HIGHLY EFFICIENT OPTICAL FREQUENCY MIXERS

Krishnan Ramaswamy Parameswaran
G. L. No. 5765

A DISSERTATION
SUBMITTED TO THE DEPARTMENT OF ELECTRICAL ENGINEERING
AND THE COMMITTEE ON GRADUATE STUDIES
OF STANFORD UNIVERSITY
IN PARTIAL FULFILLMENT OF THE REQUIREMENTS
FOR THE DEGREE OF
DOCTOR OF PHILOSOPHY

May 2002

I certify that I have read this dissertation and that in my opinion it is fully adequate, in scope and quality, as a dissertation for the degree of Doctor of Philosophy.

Martin M. Fejer
(Principal Adviser)

I certify that I have read this dissertation and that in my opinion it is fully adequate, in scope and quality, as a dissertation for the degree of Doctor of Philosophy.

Stephen E. Harris

I certify that I have read this dissertation and that in my opinion it is fully adequate, in scope and quality, as a dissertation for the degree of Doctor of Philosophy.

David A. B. Miller

Approved for the University Committee on Graduate Studies:

Abstract

This dissertation describes the development of highly efficient optical frequency mixers that build on previous work at Stanford to produce the most efficient nonlinear devices reported to date. Frequency mixing is an integral part of any broadband communications system. The ability to transfer information between carrier frequencies allows for efficient use of the available bandwidth in a transmission medium. In the electrical domain, this mixing function is very efficiently implemented using compact semiconductor devices, whose nonlinear current-voltage relationship results in the generation of output signals with frequencies at linear combinations of those of the inputs. The development of optical frequency analogs to these devices is complicated by the combination of weak nonlinearities available at optical frequencies (which necessitate the use of distributed mixers), and material dispersion. The basic techniques suited to circumventing these difficulties have been understood for decades, however the practical implementation of reasonably efficient mixers has only been achieved in the last ten years. Proton-exchanged waveguides in periodically-poled lithium niobate have proven to be the material of choice for these devices; this technology has been used to demonstrate a variety of useful all-optical signal processing functions in the last few years.

We begin with a general description of optical frequency mixing interactions, followed by a discussion of device design and fabrication. Optimization of the annealed proton-exchange process and development of buried waveguides using reverse proton-exchange have resulted in a more than three-fold improvement in conversion efficiency. The high quality of these waveguides has permitted observation of several interesting nonlinear optical phenomena for the first time, including 99 % pump depletion in single-pass second harmonic generation and the distortion in device tuning behavior that accompanies this “extreme” nonlinear optical regime. Telecommunications applications of these mixers are also presented, where all-optical gating and wavelength conversion with record efficiency have been observed.

Acknowledgements

Although the Ph.D. is nominally an individual project, success in graduate studies depends on numerous external factors. Luck plays a remarkably important role, particularly in the choice of a thesis advisor and dissertation project. In this regard, I have been very fortunate. Professor Martin M. Fejer is a wonderful supervisor. I have never met anyone with his breadth and depth of technical knowledge. Although his students often tackle very challenging problems, Marty is always able to point them in a direction that eventually leads to success. He has tremendous enthusiasm for research, but is equally at ease discussing why the Ottawa Senators cannot seem to beat the Buffalo Sabres hockey club (especially in the playoffs).

Professors Steve Harris and David Miller kindly agreed to serve on both my oral defense and reading committees. I sincerely appreciate not only their comments on this work, but many useful informal discussions in the hallways and offices of Ginzton Laboratory during my studies. Professor Robert Byer (with whom Marty Fejer shares some facilities and projects) always has encouraging words for students. His enthusiasm and global perspective is greatly appreciated, particularly on those days when nothing seems to work as it should.

When I first joined the Byer/Fejer group, several students helped me find my way in a very new environment. Mark Arbore, Loren Eyres, Leslie Gordon, Greg Miller, Bill Tulloch, Gary Woods, and Dong Zheng were very supportive in this regard. I have also worked with many other students in the group over the years, including Peter Beyersdorf, Ueyn Block, David Hum, Gennady Imeshev, Paulina Kuo, Matthew Lawrence, Justin Mansell, Tomas Plettner, Todd Rutherford, Shally Saraf, Andy Schober, Supriyo Sinha, and Arun Sridharan.

The majority of my work involved the fabrication and testing of waveguide devices. This required a very large set of diverse skills, few of which I had upon arrival at Stanford. Ming-Hsien Chou showed me many of the things I needed to know when I started. We spent many long days and nights together in Ginzton, solving myriad problems ranging from the remarkably mundane to the seemingly impossible. Perhaps his most admirable trait is his persistence when confronted with a challenging (but tractable) problem. Over the last three years, I was fortunate to work closely with Jonathan Kurz and Rosti Roussev. While I helped them become familiar with work in our group, they were very helpful in performing many of the experiments described in this dissertation, and have already produced significant results on their own. Waveguide research in the Fejer group is clearly in good hands.

Most of my experiments required the use of a homemade optical fiber amplifier. Dario Falquier and Ben Vakoc in Professor Shaw's lab showed me how to cleave and splice fibers, and helped design and build a very useful amplifier. Roger Route is the Byer/Fejer group expert on crystal growth, materials science, furnace engineering, thermocouple welding, and a host of other areas. He was instrumental in setting up the reverse proton exchange apparatus that led to the creation of the most efficient devices described in this work. Eric Gustafson was a staff scientist for most of my time in the group, and I enjoyed several interesting discussions with him about a variety of topics, both technical and otherwise.

One of the great things about Stanford is that people from all over the world come here to do research. I have had occasion to work with many visiting scholars, including David Eger (Israel), Alexei Alexandrovski (Russia), Gisele Foulon, Patrick Tourreau, and Frederic Bourgeois (France), Katia Gallo (Italy), and Sunao Kurimura (Japan). Masatoshi Fujimura made two very productive visits from Osaka University in Japan, directly contributing to significant results described in this thesis. My experience was enhanced by learning from the different perspectives of all of these individuals.

A tremendous strength of Ginzton Lab is the diversity of research being undertaken here, and the interaction between students in different groups. I spent many evenings with Scott Sharpe and Andrew Merriam of the Steve Harris group talking about nonlinear optics, Frank Sinatra, and baseball, among other things.

Kellie Koucky was the Byer/Fejer group administrator for most of my time here. She was a wonderful, warm person, and one always felt better after talking with her for a few minutes. Her untimely passing was met with great sadness, and she is dearly missed.

Although students have to do a lot by themselves, Ginzton has a staff of talented people that help perform many tasks. Larry Randall runs both the machine shop and the computer network. He has helped me machine several important components, and set up many computers in my lab over the years. I had many useful discussions about wafer dicing and endface polishing with Chris Remen and Tim Brand in the Crystal Shop. Tom Carver runs the clean room, and performed numerous depositions on my wafers. He and I were also able to solve countless problems with aging and uncooperative equipment in the clean room, without which none of my work would have been possible.

Naturally there is more to graduate student life than research (no, I don't just mean courses). The Ginzton team in the Stanford science and engineering summer softball league has evolved from perennial losers into a feared opponent over the last few years. I had the privilege to serve as captain of the team during our magical run to the finals in 2000. Street hockey is an integral part of life for most Canadian kids, and I was fortunate to find a group at Stanford (mostly expatriate Canadians) with whom I played once or twice a week. I have also made many friends in the local Karnatic (South Indian) music community, participating in several music festivals and house concerts over the years. All of these activities were welcome distractions from the daily rigors of research and courses.

The most important people in my life are my parents and my sister. They have been very supportive of my endeavors throughout my life, particularly during graduate school. I have spent countless hours on the phone with them, often describing my frustrations in the lab. Having gone through graduate studies in science and engineering themselves, they can directly relate to these problems, and always provide me with strength and encouragement. I dedicate this dissertation to them, without whom I would not be the person I am today.

Contents

Abstract **v**

Acknowledgements **vii**

1 Introduction **1**

1.1 Nonlinear Optics 2

1.2 Second Harmonic Generation 3

1.3 Bulk vs Guided-Wave Interactions 5

1.4 Other Mixing Interactions 7

1.5 Overview of this Dissertation 8

2 Theory of Three-Wave-Mixing in Quasi-Phasematched Guided-Wave Interactions **11**

2.1 Maxwell's Equations and the Nonlinear Polarizability 11

2.2 Coupled-Mode Equations 15

2.3 Dispersion and Phasematching 16

2.3.1 Quasi-Phasematching 17

2.4 Second Harmonic Generation 19

2.4.1 Undepleted Pump Limit 20

2.5 Conclusion 23

3 Device Structure and Fabrication **25**

3.1 Choosing the Right Material 25

3.2 Electric-Field Poling 26

3.3 Annealed Proton-Exchanged Waveguides 32
  3.3.1 Optimization of APE Waveguides 34
3.4 Reverse Proton-Exchange 38
  3.4.1 Comparison of Waveguide Fabrication Techniques 38
  3.4.2 Reverse Proton-Exchange Chemicals and Apparatus 39
  3.4.3 Diffusion Characterization using Planar Waveguides 40
  3.4.4 Optimization of RPE Channel Waveguides 42
  3.4.5 Measured Results 45
  3.4.6 Extrapolated Efficiency 48
3.5 Conclusion 48

4 Observation of 99 % Pump Depletion in Single Pass Second Harmonic Generation 49
4.1 SHG Theory Including Pump Depletion 50
4.2 Pump Depletion vs Conversion Efficiency 52
4.3 Experimental Challenges 53
  4.3.1 Bulk vs Waveguide Interactions 53
  4.3.2 Power Considerations 55
  4.3.3 Parasitic Processes 56
  4.3.4 Narrow Tuning Bandwidths - Tight Fabrication Tolerances . . 57
4.4 Experimental Setup - Quasi-CW Source 58
  4.4.1 Mitigation of Stimulated Brillouin Scattering 60
  4.4.2 Power Amplifier Section 61
  4.4.3 Narrowband Filtering 61
4.5 Pump Depletion Results 62
4.6 Wavelength Tuning Curves in the Strongly Depleted Limit 64
  4.6.1 Experiment and Results 64
4.7 Conclusion 67

5 Telecommunications Experiments 71
5.1 Optical Gating using Sum Frequency Mixing 71
  5.1.1 Sum Frequency Generation 72

5.1.2 SFG Experiment 74
5.1.3 Loop Mirror Configuration 78
5.2 Wavelength Conversion using Cascaded SHG and DFG 81
5.2.1 Theory of Cascaded SHG/DFG 83
5.2.2 $\chi^{(2)} : \chi^{(2)}$ Wavelength Conversion Experiment Using a Buried Waveguide 84
5.3 Conclusion 87

6 Summary and Future Directions 89
6.1 Summary of Contributions 89
6.2 Future Directions 90
6.2.1 System Applications 90
6.2.2 Novel Materials 91
6.3 Conclusion 94

A List of Journal Publications and Conference Presentations 95
A.1 Journal Publications 95
A.2 Conference Presentations 97

Bibliography 103

List of Tables

4.1 Comparison of FWHM of Tuning Curves at Low and High Pump Depletion 58

List of Figures

1.1 Comparison between radio and optical frequency mixers. 1

1.2 Second harmonic generation involves the creation of one photon at frequency 2ω from two photons at frequency ω. 3

1.3 Wave vectors for second harmonic generation - a)interactions are generally not phasematched, b)perfect phasematching can be achieved for some interactions at some temperatures using material birefringence, c)quasi-phasematching involves engineering the material with an extra grating vector K_g to have $\Delta k = 0$. 4

1.4 Comparison of a)bulk and b)guided-wave mixing interactions. 5

1.5 The conversion efficiency of SHG asymptotically approaches unity with increasing nonlinear drive ΓL. 7

1.6 Frequencies involved in a)sum frequency and b)difference frequency generation, which is accompanied by optical parametric amplification (OPA). 7

2.1 Plot of second harmonic power as a function of propagation distance in a second-order nonlinear medium. 17

2.2 Plot of second harmonic generation tuning curve for ideal and distorted phasematching distribution 21

3.1 Photograph of a typical poling fixture, consisting of Plexiglas blocks between which the 3-inch-diameter wafer (shown patterned with photoresist) is clamped. Chambers on either side are filled with liquid electrolyte that provides a conduction path between the gold-plated electrodes and the wafer surface. 28

3.2 Oscilloscope trace showing typical current and voltage waveforms resulting from electric-field poling of a lithium niobate wafer of three inch diameter. 29

3.3 Micrograph of PPLN surface after etching in hydrofluoric acid. Domains of reversed polarity are etched, while original domains are not, such that domain boundaries are revealed as lines. Wide stripes result in wavy domain boundaries and occasional run-togethers. 31

3.4 Segmentation of grating segments results in much higher poling quality. The domain walls are very straight, and run-togethers are mostly eliminated. 31

3.5 Schematic diagram of non-critical waveguide design (not to scale). . . 36

3.6 Low-power, CW SHG tuning curve for optimized APE waveguide. . . 37

3.7 Comparison between proton-exchanged (PE), annealed proton-exchanged (APE), and reverse proton-exchanged (RPE) index and mode profiles in the depth dimension. 38

3.8 Absorption of planar waveguide sample after various reverse exchange times. Reasonable agreement with the calculation is observed. 42

3.9 Comparison of optimized APE and RPE (buried) index profiles. The peak index step is slightly less than 25 % of the as-exchanged value in both cases. 44

3.10 Normalized electric field profiles for a)APE and b)RPE waveguides. The dead layer is outlined in the APE figure. 44

3.11 Plot of calculated phasematching wavelength vs waveguide width for RPE waveguides, illustrating non-critical point near 8.25 μm. The line is shown only to guide the eye. 45

3.12 Measured phasematching wavelength vs waveguide width, showing noncritical point between 7 and 8 μm. The line is shown only to guide the eye. 46

3.13 Low-power CW SHG tuning curve for optimized RPE device. 47

3.14 Spatial mode profile and depth cross-section for RPE waveguide. . . . 47

4.1 Variation of conversion efficiency and tuning curve FWHM with nonlinear drive. Tuning curve shapes are shown as insets. 51

4.2 Gain induced diffraction in high efficiency bulk SHG. At low conversion efficiencies, the beam is loosely focused and the phase fronts are symmetric on either side of the focus (thin lines). At high efficiency, the central part of the beam sees much stronger conversion than the wings, such that it is focused to a tighter spot (thick lines), resulting in faster diffraction after the focus. The beam then becomes distorted, as illustrated by the curved phase fronts. Figure is adapted from [1]. . 54

4.3 Shape of tuning curve in the undepleted pump limit. 57

4.4 Experimental setup for pump depletion experiment. An external cavity diode laser (ECDL) amplified by a chain of erbium doped fiber amplifiers (EDFAs) produces quasi-CW pulses that are launched into the waveguide. Photodiodes are used to measure the power at the interacting wavelengths. 59

4.5 Low-power, CW SHG tuning curve for optimized APE waveguide used in pump depletion experiment. 62

4.6 Pump depletion and second harmonic generation power as functions of input pump power. The data fit well with the calculation, with pump depletion reaching 99 % with 900 mW input. 63

4.7 Calculations of tuning curve shapes at varying levels of maximum pump depletion. The bandwidth narrows and sidelobes rise as the maximum depletion approaches 100 %. 65

4.8 Low-power CW SHG tuning curve for waveguide used in observation of Jacobi elliptic tuning curves. 66

4.9 Experimental setup for measuring wavelength tuning curves in the highly depleted limit. This setup is similar to that used for the pump depletion measurement (Figure 4.4), where some elements have been removed to facilitate wavelength tuning. 67
4.10 Normalized SHG tuning curves for various levels of pump depletion. Good agreement is observed between measurement and calculation. The peak input power is shown to the left of each curve. 68
4.11 Tuning curve taken in the regime where back-conversion (in the form of parametric amplification of ASE) is taking place. Very strong distortion is observed, where simple theory can no longer predict the shape. 69

5.1 Energy level diagram describing sum frequency generation interaction. 72
5.2 Calculation of signal and sum frequency transmission as functions of control power in an SFG interaction. 74
5.3 Low power CW SHG tuning curve for device used in SFG experiment. 75
5.4 Experimental setup for optical gating using SFG. 76
5.5 Measured pulse traces, showing depletion of the signal in the presence of the control beam. 77
5.6 Measured and calculated variation of signal transmission with control power. 78
5.7 Nonlinear optical loop mirror structure using $\chi^{(2)}$ interaction. 79
5.8 Photon picture of difference frequency generation and optical parametric amplification. 82
5.9 Wavelength conversion through cascaded SHG/DFG processes. 82
5.10 Experimental apparatus for wavelength conversion through cascaded SHG/DFG processes. 84
5.11 Low power CW SHG tuning curve for device used in cascaded wavelength conversion experiment. 85
5.12 Optical spectrum analyzer traces showing signal and output transmission with and without pump power. Internal (external) parametric gain of 5 dB (1.8 dB) is observed at a pump power of 180 mW. . . . 86

5.13 Plot of measured and calculated DFG efficiency as a function of pump power with $\eta_{nor}L^2 = 3000$ %/W. 86

6.1 Various novel integrated optics structures implemented lithographically in silicon dioxide mask sputtered on PPLN substrate. These structures provide useful functions in nonlinear waveguides. Accurate modeling of APE and RPE processes will allow for better design of these structures. Figure courtesy of Jonathan Kurz. 92

Chapter 1

Introduction

Recent years have seen the rapid development of optical component and system technology. Much of this effort has been driven by the communications industry, where businesses and individual consumers continue to demand increased bandwidth and enhanced services at ever-decreasing cost. Transmission speeds in the coaxial cables traditionally used for electrical communication are fundamentally limited by loss and dispersion. Optical fiber allows simultaneous propagation of many independent signals at extremely high speeds without significant crosstalk. The fortuitous overlap of wavelength bands exhibiting low propagation loss in silica fiber with the gain bandwidth of erbium-doped silica has led to the development of efficient all-optical amplifiers [2]. This key technology has allowed for compensation of passive loss in fiber spans, permitting long-haul transmission of optical signals without conversion between the optical and electrical domains. Despite the impressive data rates, trans-

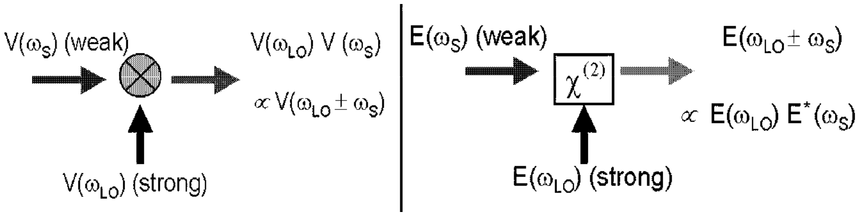

Figure 1.1: Comparison between radio and optical frequency mixers.

mission spans, and multi-wavelength transmission results to date [3], signal processing functions other than amplification are usually implemented electronically in currently installed optical communications systems. The remarkable development of semiconductor technology over the past several decades has led to a virtually limitless array of complex functions implemented in small, efficient packages. Many of these functions require nonlinear mixing of signals in order to shift information between different frequencies. The basic building blocks of these circuits are the electrical diode and transistor. The highly nonlinear current-voltage relationship in these devices allows for efficient mixing of signals with very low switching powers. A truly all-optical network requires novel devices capable of this type of efficient manipulation of signals within the optical domain.

Figure 1.1 compares radio and optical frequency mixers in general terms. Radio-frequency devices are often analyzed in terms of the interacting voltages, since at low frequencies, the circuits can be considered lumped elements. At optical frequencies, devices of any reasonable size are many wavelengths long, such that it is more instructive to consider the interaction in terms of electric fields propagating through the device at different speeds.

1.1 Nonlinear Optics

The source of the nonlinearity in three-wave optical frequency mixers is the second-order nonlinear susceptibility $\chi^{(2)}$. When an optical frequency electric field is applied to a solid dielectric medium, a polarization results from the movement of the electron cloud in response to this field:

$$P = \epsilon_0(\chi^{(1)}E + \chi^{(2)}E^2 + \chi^{(3)}E^3 + ...) \tag{1.1}$$

The first term (linear in the electric field) produces no new frequency components, and is responsible for linear optical phenomena such as refraction, diffraction, and dispersion. The higher order (nonlinear) terms result in the creation of fields at new frequencies. Three-wave mixing takes place through the second-order term $\chi^{(2)}$. If

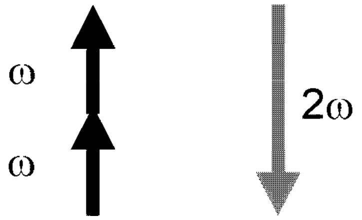

Figure 1.2: Second harmonic generation involves the creation of one photon at frequency 2ω from two photons at frequency ω.

the electric field is described by $E = E_0\cos(\omega t)$, then the second-order polarization term becomes:

$$P = \epsilon_0\chi^{(2)}E_0^2\cos^2(\omega t) = \frac{1}{2}\epsilon_0\chi^{(2)}E_0^2 + \frac{1}{2}\epsilon_0\chi^{(2)}E_0^2\cos(2\omega t) \tag{1.2}$$

The first term in the rightmost expression is a DC frequency component, representing optical rectification. The second term results in second harmonic generation (SHG), where the generated polarization serves as a driving term in Maxwell's equations that leads to the creation of a free wave at the second harmonic frequency 2ω. SHG is the simplest three-wave mixing interaction, where two photons at the fundamental frequency are destroyed to create one at the second harmonic (Figure 1.2). Hence SHG serves as a useful starting point from which more complex functions can be understood.

1.2 Second Harmonic Generation

Since the first observation of SHG by Franken et al in 1961 [4], this process has been exploited to extend the range of lasers to frequencies that are difficult to obtain by other means. Successful commercial applications of SHG include green light generation through frequency doubling of diode-pumped solid state lasers (a combination that can replace bulky argon lasers for pumping $\mathrm{Ti:Al_2O_3}$ oscillators) [5], and blue light generation by SHG of red diode lasers (where the shorter blue wavelength allows for higher storage densities in digital video disk recorders) [6].

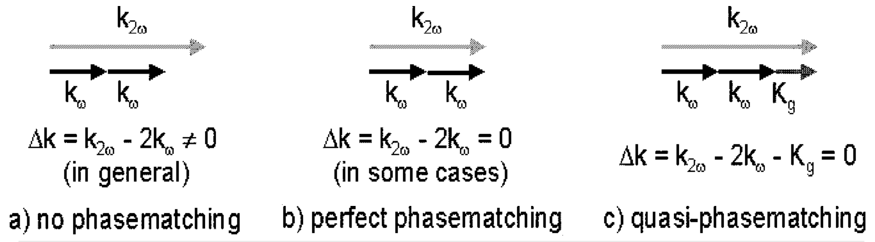

Figure 1.3: Wave vectors for second harmonic generation - a)interactions are generally not phasematched, b)perfect phasematching can be achieved for some interactions at some temperatures using material birefringence, c)quasi-phasematching involves engineering the material with an extra grating vector K_g to have $\Delta k = 0$.

While the photon picture in Figure 1.2 describes the conservation of energy condition satisfied by the interacting waves, efficient energy transfer only occurs when there is a fixed phase relationship between them. The propagation constants or wave vectors associated with each wave are depicted in Figure 1.3. The magnitude of this parameter is defined as $k_i = 2\pi n_i/\lambda_i$, where n is the refractive index determined by the linear susceptibility ($n = \sqrt{1 + \chi^{(1)}}$), and $\lambda = 2\pi c/\omega$ is the free space wavelength corresponding to frequency ω, with c being the speed of light in vacuum. Material dispersion leads to refractive index variation with frequency, such that in general, $\Delta k = k_{2\omega} - 2k_\omega \neq 0$ (Figure 1.3a). In other words, the two waves propagate through the crystal at different speeds, such that their phase relationship varies as a function of position. As a result, power is transferred back and forth between the fundamental and second harmonic as the two waves move in and out of phase. Perfect phasematching can be achieved in some situations, as shown in Figure 1.3b. This technique usually involves exploitation of material birefringence [7, 8], where at some temperatures in particular materials, the index at the fundamental frequency in one polarization is exactly equal to that at the second harmonic in a different polarization. Birefringent phasematching is clearly a restrictive technique, as a given material can only be used for a finite number of mixing interactions dictated by nature. Quasi-phasematching (Figure 1.3c) is a technique whereby an extra grating vector K_g is

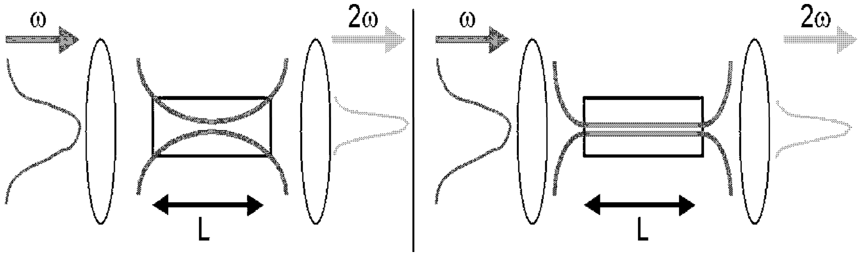

Figure 1.4: Comparison of a)bulk and b)guided-wave mixing interactions.

artificially introduced into the material, allowing for compensation of arbitrary values of phase mismatch, such that a given material can be engineered to perform a variety of mixing functions. The most common means of implementing this extra vector is to introduce a periodic modulation of the sign of the nonlinear coefficient [9].

The expression for SHG conversion efficiency in a plane wave interaction is [10]:

$$\bar{\eta} = \frac{P_{2\omega}}{P_\omega} = (\frac{8\pi^2 d^2}{n_\omega^2 n_{2\omega} c\epsilon_0 \lambda_\omega^2})(\frac{P_\omega L^2}{A}) = \kappa^2(\frac{P_\omega L^2}{A}) \tag{1.3}$$

where $d = \chi^{(2)}/2$ is the nonlinear coefficient, $n_\omega, n_{2\omega}$ are the refractive indices at the two frequencies, c is the speed of light, ϵ_0 is the permittivity of free space, λ_ω is the wavelength at the fundamental frequency, and L is the device length. It should be noted that the efficiency scales linearly with the optical intensity, where the latter is defined as the ratio of the optical power (P_ω) to the cross-sectional overlap area (A) of the interacting waves.

1.3 Bulk vs Guided-Wave Interactions

The original observations of nonlinear optical phenomena occurred in bulk materials, where free space optical beams (typically having Gaussian transverse profiles) are focused into the medium using bulk optics (Figure 1.4a). Although the spot size and overlap area A are small near the center of the crystal (leading to high localized intensity and efficiency), diffraction results in a much larger spot and lower intensity at the ends of the device. The situation where the smallest spot is at the center of the crystal and the beam size at the crystal edges is $\sqrt{2}$ times this value is known as confocal focusing, which is close to the optimum condition [11], where diffraction leads to a length-dependent overlap area $A = L\lambda_\omega/2n_\omega$. Substituting this result into equation (1.3) reveals that $\bar{\eta}_{BULK} \propto L$ for optimized bulk mixing. Achieving complete transfer of power from the fundamental to the second harmonic wave is also challenging in this case, as the wings of the mode always have much lower intensity than the peak. Hence in order to convert the wings, the peak must be driven to extremely high intensities, where gain-induced diffraction and back-conversion can occur.

In a waveguide (WG) interaction (Figure 1.4b), mixing takes place between discrete spatial eigenmodes. Here, small spot sizes can be maintained over the entire interaction length, such that A_{WG} is independent of L, and $\bar{\eta}_{WG} \propto L^2$. Hence waveguide mixers use the device length much more efficiently than bulk devices. Furthermore, the waveguide modes mix as complete entities. Hence transverse spatial variations do not limit the overall conversion efficiency. Optimization of the waveguide design involves engineering the index profile to maximize the spatial overlap of the modes, which then minimizes A_{WG}. The normalized conversion efficiency is then defined as $\eta_{nor} = \kappa^2/A_{WG}$, with κ from equation (1.3).

When either phasematching or quasi-phasematching is accomplished, as the second harmonic builds at the beginning of the interaction, its phase with respect to the fundamental is locked, such that power flows unidirectionally from the fundamental to the second harmonic. As the power in the fundamental wave is increased, the conversion efficiency asymptotically approaches unity, as shown in Figure 1.5. This calculation is for a waveguide interaction, where there is no variation in the transverse profiles of the interacting waves. Even in this situation, achieving conversion efficiency near unity is very challenging, as small deviations from the phasematched condition result in back-conversion from the second harmonic to the fundamental wave.

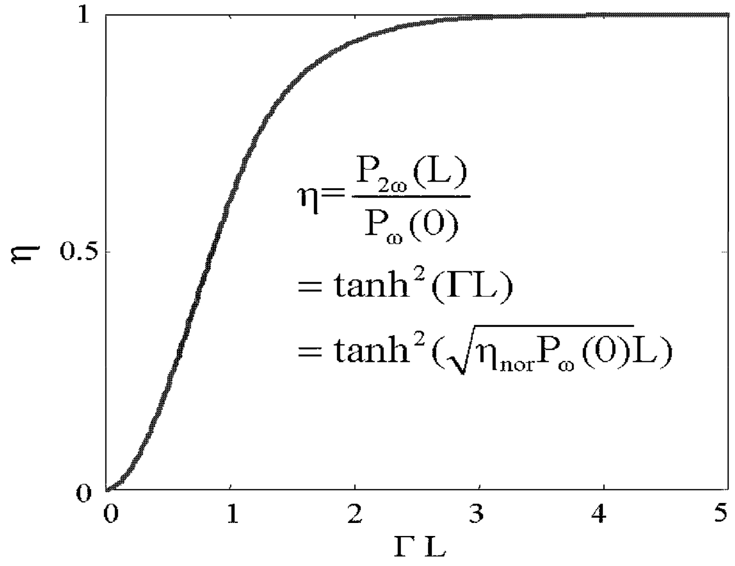

Figure 1.5: The conversion efficiency of SHG asymptotically approaches unity with increasing nonlinear drive ΓL.

1.4 Other Mixing Interactions

While SHG is a very useful function by itself, in the communications band (at wavelengths around 1550 nm) it is more commonly used as a diagnostic for measuring the quality of devices for use in other mixing functions. These more complicated interactions include sum frequency generation (SFG) and difference frequency generation (DFG). Figure 1.6 compares these processes in terms of the interacting frequencies.

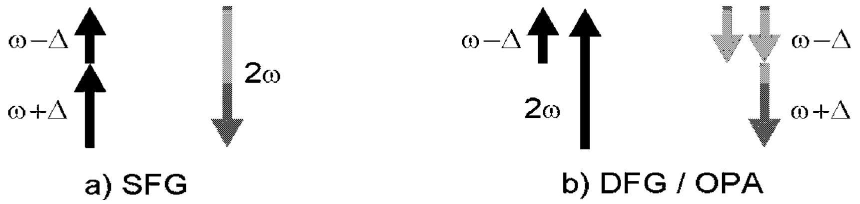

Figure 1.6: Frequencies involved in a)sum frequency and b)difference frequency generation, which is accompanied by optical parametric amplification (OPA).

Both involve the transfer of information from the signal frequency to a newly generated output frequency, a function known as wavelength conversion. In SFG, both input photons are destroyed to create the output photon at frequency 2ω. Hence this interaction allows for implementation of an optical gate or switch, where turning up the power in the stronger beam results in depletion of the weaker one. The DFG process involves destruction of a high energy photon at 2ω to create a new photon at the difference frequency $2\omega - (\omega - \Delta) = \omega + \Delta$, along with an additional photon at the original signal frequency $\omega - \Delta$. Hence this process also results in optical parametric amplification (OPA) of the signal. Several properties inherent to these parametric processes make optical frequency mixers attractive for many applications. These properties include transparency to transmission format, large signal dynamic range, and large modulation bandwidth. Wavelength conversion within a single wavelength band [12, 13], between two bands [14, 15], chromatic dispersion compensation [16], and gated mixing for optical time division multiplexing (OTDM) [17] are just a few examples of functions that have been successfully demonstrated with these mixers in the last few years.

1.5 Overview of this Dissertation

The research described in this dissertation involves the development of highly efficient optical frequency mixers, which are used to demonstrate many all-optical signal processing functions. The two primary goals of this work were the improvement of device performance (in terms of mixing efficiency) and the investigation of the behavior of these mixers in a regime where one of the waves is strongly depleted. The former was achieved by implementing buried waveguides using annealed and reverse proton-exchange in periodically-poled lithium niobate. These buried structures exhibit a normalized conversion efficiency three times that of devices previously demonstrated, leading to an order-of-magnitude increase in the efficiency of devices operated in the commonly-used cascaded $\chi^{(2)}$ configuration (Section 5.2). The strongly depleted regime was explored by constructing an amplified laser source capable of producing quasi-CW pulses with high peak power, low average power, and relatively long pulsewidth. Second harmonic generation of these pulses in optimized waveguide mixers was performed, where a record 99 % pump depletion was observed without back-conversion, validating the quality of the fabrication process. As discussed above, these mixers have many applications in communications. To demonstrate these applications, devices were designed for operation in the telecommunications band ($\lambda \approx 1550$ nm), and two significant functions (all-optical gating using SFG and wavelength conversion/parametric amplification using DFG/OPA) were demonstrated with record efficiency.

A description of the basic physics of the three-wave mixing process, including presentation of a mathematical framework with which the devices can be described, is presented in Chapter 2. This description is followed by details of the device design and fabrication in Chapter 3, including materials studies and optimized processing recipes for producing high quality mixers. Chapter 4 explores the regime of extremely large pump depletion in second harmonic generation. The high quality waveguides allow for experimental observation of several phenomena for the first time. Chapter 5 describes telecommunications applications of these mixers. A summary of this research is presented in Chapter 6 along with a discussion of future directions.

Chapter 2

Theory of Three-Wave-Mixing in Quasi-Phasematched Guided-Wave Interactions

The purpose of this chapter is to present a mathematical framework for the description of three-wave mixing interactions in guided-wave structures. The notation used here is followed in subsequent chapters discussing device performance and experimental results. Maxwell's equations are used to develop a set of coupled differential equations describing the interaction of waveguide modes. Solutions for the particular case of second harmonic generation are presented, including the effects of loss and phase mismatch. Further development of solutions for other interactions is presented in subsequent chapters in order to facilitate comparison with experimental results.

2.1 Maxwell's Equations and the Nonlinear Polarizability

Maxwell's equations are the fundamental relationships with which all electromagnetic phenomena can be described:

$$\nabla \times \tilde{\mathbf{E}} = -\frac{\partial \tilde{\mathbf{B}}}{\partial t} \tag{2.1}$$

$$\nabla \times \tilde{\mathbf{H}} = \tilde{\mathbf{J}} + \frac{\partial \tilde{\mathbf{D}}}{\partial t} \tag{2.2}$$

$$\nabla \cdot \tilde{\mathbf{D}} = \rho \tag{2.3}$$

$$\nabla \cdot \tilde{\mathbf{B}} = 0 \tag{2.4}$$

In this notation, $\tilde{\mathbf{E}}$ is the electric field, $\tilde{\mathbf{B}}$ is the magnetic flux density, $\tilde{\mathbf{H}}$ is the magnetic field, $\tilde{\mathbf{J}}$ is the free current density, $\tilde{\mathbf{D}}$ is the electric displacement, and ρ is the free charge density. Symbols with tildes represent time-dependent quantities, and vectors are denoted by **boldface** type. The dielectric waveguides described in this dissertation have no free charge carriers, hence $\rho = 0$. We define an effective conductivity σ such that $\tilde{\mathbf{J}} = \sigma \tilde{\mathbf{E}}$ represents the effect of waveguide loss.

The constitutive relations that contain information about the material parameters are:

$$\tilde{\mathbf{B}} = \mu \tilde{\mathbf{H}} = \mu_0 \mu_r \tilde{\mathbf{H}} = \mu_0 \tilde{\mathbf{H}} \tag{2.5}$$

$$\tilde{\mathbf{D}} = \epsilon \tilde{\mathbf{E}} = \epsilon_0 \epsilon_r \tilde{\mathbf{E}} + \tilde{\mathbf{P}}_{\mathbf{NL}} \tag{2.6}$$

where we set $\mu_r = 1$ since we are dealing with non-magnetic media in this work. When an optical frequency electric field is applied to a solid dielectric medium, a polarization results from the movement of the electron cloud in response to this field. The first term on the right hand side of equation (2.6) represents the linear part of this polarization, which is responsible for phenomena such as refraction, diffraction, and dispersion, where $n = \sqrt{\epsilon_r}$ is the refractive index. The higher order susceptibility terms responsible for nonlinear processes (some of which generate new frequencies) take the form:

$$P_{NL_i} = \epsilon_0 (\chi^{(2)}_{ijk} E_j E_k + \chi^{(3)}_{ijkl} E_j E_k E_l + ...) \tag{2.7}$$

where P_{NL_i} is the component of the polarization in a particular direction i, and E_j, E_k can be at different frequencies in general. As in any power series expansion, the higher order terms in the series get successively weaker. In three-wave mixing we are interested only in the first term, whose tensor nature is shown by writing it in the form:

$$P_{NL_i} = \epsilon_0 \sum_{ijk} \chi^{(2)}_{ijk} E_j E_k \tag{2.8}$$

This expression explicitly shows the relationship between differently polarized fields and the generated polarization.

If we assume a harmonic time dependence of the field quantities of the form:

$$\tilde{\mathbf{E}}(x, y, z, t) = \mathrm{Re}[\mathbf{E}(x, y, z)\mathrm{exp}(j\omega t)] \tag{2.9}$$

then substitution of the constitutive relations into Maxwell's equations yields:

$$\nabla \times \mathbf{E} = -j\omega\mu_0\mathbf{H} \tag{2.10}$$

$$\nabla \times \mathbf{H} = (\sigma + j\omega\epsilon_0\epsilon_r)\mathbf{E} + j\omega\mathbf{P_{NL}} \tag{2.11}$$

In the absence of a nonlinear polarization, the solutions to these equations in a waveguide form a set of discrete modes $\mathbf{E}_\nu$, each having an effective index n_ν that describes its propagation. These modes can be expressed as the product of a length-independent transverse profile and an envelope function that evolves with position:

$$\mathbf{E}_\nu(x, y, z) = \mathbf{E}_\nu(x, y)A_\nu(z)\mathrm{exp}(-jk_\nu z) \tag{2.12}$$

$$\mathbf{H}_\nu(x, y, z) = \mathbf{H}_\nu(x, y)B_\nu(z)\mathrm{exp}(-jk_\nu z) \tag{2.13}$$

where $\mathbf{E}_\nu, \mathbf{H}_\nu$ are normalized transverse field amplitudes, A_ν, B_ν are slowly varying envelope functions, and $k_\nu = 2\pi n_\nu/\lambda$. These modes form an orthogonal set such that

$$\frac{1}{2}\int_{-\infty}^{\infty}\int_{-\infty}^{\infty} \mathrm{Re}[\mathbf{E}_\nu(x, y)A_\nu(z) \times \mathbf{H}^*_\mu(x, y)B^*_\mu(z)] \cdot \hat{\mathbf{z}}dxdy = \delta_{\nu\mu}P_\nu(z) \tag{2.14}$$

where P_ν is the power carried by the νth mode.

For waveguides where the index step is a relatively small fraction of the substrate index (as is the case for the devices used in this work), the "weak guidance" approximation [18] allows us to take the fields as being transverse, where we neglect the field components along the propagation direction. This approximation allows us to use the following relationship between the electric and magnetic fields (as is used in the analysis of TEM waves):

$$\mathbf{H}(x,y)B_\nu(z) \approx \sqrt{\frac{\epsilon_0}{\mu_0}} n_\nu \hat{\mathbf{z}} \times \mathbf{E}(x,y)A_\nu(z) \tag{2.15}$$

such that the orthogonality relationship becomes:

$$\frac{1}{2}\int_{-\infty}^{\infty}\int_{-\infty}^{\infty} \mathrm{Re}[\mathbf{E}_\nu(x,y)A_\nu(z) \cdot \sqrt{\frac{\epsilon_0}{\mu_0}} n_\nu \mathbf{E}^*_\mu(x,y)A^*_\mu(z)]dxdy = \delta_{\nu\mu}P_\nu(z) \tag{2.16}$$

so

$$\int_{-\infty}^{\infty}\int_{-\infty}^{\infty} |\mathbf{E}_\nu(x,y)|^2 dxdy = 1 \tag{2.17}$$

where

$$P_\nu(z) = \frac{n_\nu \epsilon_0 c}{2}|A_\nu(z)|^2 \tag{2.18}$$

We now absorb the constants into the definition of the envelope function, such that:

$$P_\nu(z) \equiv |A_\nu(z)|^2 \tag{2.19}$$

This normalization (where $A_\nu(z)$ has units of $\sqrt{\mathrm{W}}$) simplifies the subsequent analysis.

The conservation of energy condition for a general three-wave mixing interaction is:

$$\omega_3 = \omega_1 + \omega_2 \tag{2.20}$$

The waveguides developed in this work guide only one polarization, so were are only interested in interactions where all three waves are co-polarized. The scalar magnitudes of the nonlinear polarization in this case become:

$$P_{NL}(\omega_3) = 2\epsilon_0 d_0 \bar{d}(x,y)d(z)E(\omega_1)E(\omega_2) \tag{2.21}$$

$$P_{NL}(\omega_2) = 2\epsilon_0 d_0 \bar{d}(x,y)d(z)E(\omega_3)E^*(\omega_1) \tag{2.22}$$

$$P_{NL}(\omega_1) = 2\epsilon_0 d_0 \bar{d}(x,y)d(z)E(\omega_3)E^*(\omega_2) \tag{2.23}$$

where $d = \chi^{(2)}/2$ is the component of the nonlinear susceptibility tensor coupling the three co-polarized fields. The function $\bar{d}(x, y)$ accounts for variation of the nonlinear coefficient in the plane normal to the propagation direction. In the proton-exchanged lithium niobate material system considered in this dissertation, the nonlinear coefficient has been found to vanish in the as-exchanged material [19]. Subsequent annealing leads to partial recovery of the nonlinearity, leading to the spatial variation described by $\bar{d}(x, y)$. This subject will be addressed in greater detail in Section 3.3.

2.2 Coupled-Mode Equations

In order to describe the three-wave mixing process, the polarization terms can be substituted into Maxwell's equations to produce a set of coupled differential equations. The derivation of these coupled-mode equations has been presented in great detail elsewhere [20] and is not repeated here. Given the normalizations of the previous section, these equations take the following form:

$$\frac{dA_3}{dz} = -j\kappa_3 \nu A_1 A_2 \exp(j\Delta k' z) - \frac{\alpha_3}{2} A_3 \tag{2.24}$$

$$\frac{dA_2}{dz} = -j\kappa_2 \nu^* A_1^* A_3 \exp(-j\Delta k' z) - \frac{\alpha_2}{2} A_2 \tag{2.25}$$

$$\frac{dA_1}{dz} = -j\kappa_1 \nu^* A_2^* A_3 \exp(-j\Delta k' z) - \frac{\alpha_1}{2} A_1 \tag{2.26}$$

The coupling coefficients are defined as:

$$\kappa_i = \sqrt{\frac{8\pi^2 d_0^2}{n_1 n_2 n_3 c \epsilon_0 \lambda_i^2}} \tag{2.27}$$

The phase velocity mismatch is:

$$\Delta k' = k_3 - k_2 - k_1 = 2\pi(\frac{n_3}{\lambda_3} - \frac{n_2}{\lambda_2} - \frac{n_1}{\lambda_1}) \tag{2.28}$$

The spatial overlap factor is:

$$\nu = \int_{-\infty}^{\infty} \int_{-\infty}^{\infty} \bar{d}(x,y) E_1(x,y) E_2(x,y) E_3^*(x,y) dx dy \tag{2.29}$$

This factor (with units of 1/length) accounts for the transverse spatial overlap of the interacting modes, and is related to the overlap area A discussed in Chapter 1 as $A = 1/\nu^2$. Hence maximizing the efficiency requires minimizing A, which means maximizing ν. The power loss coefficients are given by:

$$\alpha_i = \frac{\mu_0 \sigma_i c_0}{2} \tag{2.30}$$

where the σ_i are the effective conductivities described in section 2.1.

2.3 Dispersion and Phasematching

Dispersion is the variation of refractive index with wavelength. In waveguides, several effects cause dispersion. The contribution from the physical properties of the material in question is known as material dispersion. Waveguide dispersion refers to the effect of the geometrical structure of the index distribution. In waveguides supporting multiple transverse modes, intermodal dispersion describes the variation of index between different spatial modes [20]. All of these effects contribute to the determination of the effective indices of the interacting waveguide modes (n_i in equations (2.27) and (2.28) above). For a given waveguide and set of frequencies, $\Delta k' \neq 0$ in general due to dispersion. In this case, the phase relationship between the three interacting waves is constantly changing as a function of position, such that the direction of power flow does the same. In most interactions of interest, the goal is to transfer power from one wave to one or both of the others. This function is most easily accomplished when the phase velocity mismatch is eliminated. Birefringent phasematching [7, 8] is a commonly used approach, where (at a particular temperature) the effective indices of the interacting waves having different polarizations result in $\Delta k' = 0$. This approach is restrictive, in that the range of interactions that can be phasematched in this way

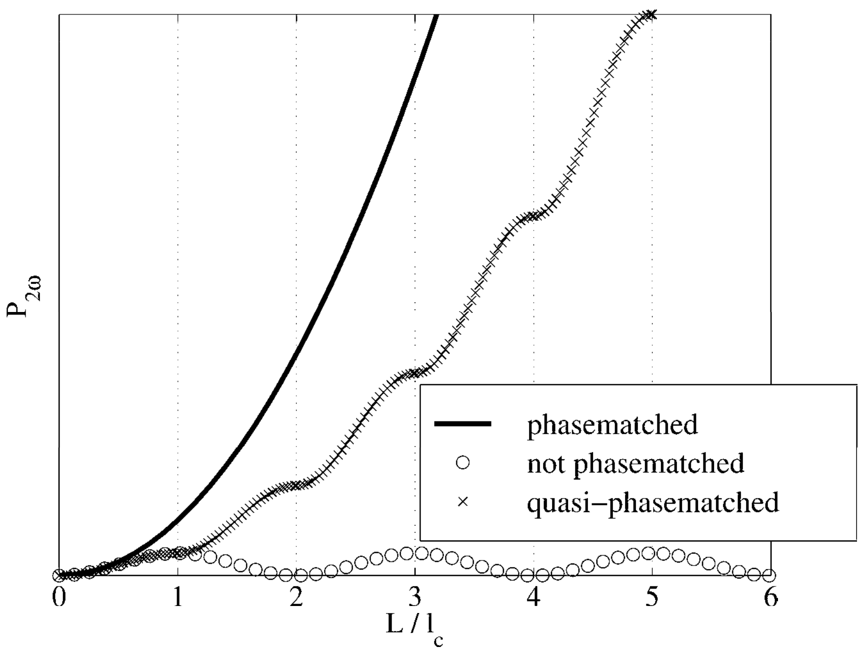

Figure 2.1: Plot of second harmonic power as a function of propagation distance in a second-order nonlinear medium.

is limited by nature. It is also not applicable in waveguides that only support a single polarization.

2.3.1 Quasi-Phasematching

Quasi-phasematching (QPM) is a technique whereby materials can be engineered to produce unidirectional power flow for any mixing interaction for which the material is transparent [21, 22]. This method involves reversal of the sign of the nonlinear coefficient every time the accumulated phase difference reaches π. Hence the period of the QPM grating is:

$$\Lambda = 2l_c = \frac{2\pi}{\Delta k'} \tag{2.31}$$

where l_c is known as the coherence length. Figure 2.1 shows a plot of power generated as a function of position for the simple case of second harmonic generation. Without phasematching, the generated second harmonic grows and decays as the fundamental and second harmonic waves go in and out of phase over each coherence length. In the perfectly phasematched case (as is obtained using birefringence), the generated power grows quadratically with position. The QPM sign reversal at each multiple of l_c also results in a net quadratic increase with distance, where the discrete nature of the reversals results in a lower second derivative than that obtained with perfect phasematching.

The periodic variation of the nonlinear coefficient produced by the QPM grating can be represented by the following Fourier series [9]:

$$g(z) = \sum_{m=-\infty}^{\infty} G_m \exp(jK_m z) \tag{2.32}$$

where the wave vector of the mth harmonic is given by:

$$K_m = \frac{2\pi m}{\Lambda} \tag{2.33}$$

It can be easily shown that the Fourier amplitude for a square wave of duty cycle D is:

$$G_m = \frac{2}{m\pi} \sin(m\pi D) \tag{2.34}$$

The nonlinear coefficient is then given by:

$$d(x,y,z) = d_{eff}\bar{d}(x,y)g(z) \tag{2.35}$$

where d_{eff} is an effective nonlinear coefficient to be defined below. Efficient mixing can be obtained by choosing $K_m = \Delta k'$, such that the phase mismatch term becomes:

$$\Delta k \equiv \Delta k' - K_m = k_3 - k_2 - k_1 - K_m \tag{2.36}$$

The coupled mode equations for the QPM interaction then become:

$$\frac{dA_3}{dz} = -j\kappa_3 \nu A_1 A_2 \exp(j\Delta k z) - \frac{\alpha_3}{2} A_3 \tag{2.37}$$

$$\frac{dA_2}{dz} = -j\kappa_2\nu^* A_1^* A_3 \exp(-j\Delta kz) - \frac{\alpha_2}{2}A_2 \tag{2.38}$$

$$\frac{dA_1}{dz} = -j\kappa_1\nu^* A_2^* A_3 \exp(-j\Delta kz) - \frac{\alpha_1}{2}A_1 \tag{2.39}$$

$$\kappa_i = \sqrt{\frac{8\pi^2 d_{eff}^2}{n_1 n_2 n_3 c\epsilon_0 \lambda_i^2}} \tag{2.40}$$

These are identical to equations (2.24)-(2.27), where Δk replaces $\Delta k'$ and the nonlinear coefficient $d_0 d(z)$ is replaced by an effective nonlinearity scaled by the grating amplitude G_m:

$$d_{eff} = d_0 G_m = \frac{2d_0}{m\pi}\sin(m\pi D) \tag{2.41}$$

For first order QPM (where $m = 1$), the optimum duty cycle is $D = 50\%$, such that:

$$d_{eff} = \frac{2d_0}{\pi} \tag{2.42}$$

Hence the net effect of the first order grating is the reduction of the effective nonlinear coefficient by a factor of $2/\pi$.

2.4 Second Harmonic Generation

Analytical solutions to the coupled mode equations can be found for many combinations of interacting wavelengths and boundary conditions. Of these interactions, second harmonic generation (SHG) is of particular interest, as it is the simplest three-wave mixing process, where two of the three waves are at the same frequency:

$$\omega_2 = 2\omega_1 \tag{2.43}$$

For this special case, the polarization term becomes:

$$P_{NL}(\omega_2) = \epsilon_0 d_{eff}\bar{d}(x,y)[E(\omega_1)]^2 \tag{2.44}$$

such that the coupled mode equations have the form

$$\frac{dA_2}{dz} = -j\sqrt{\eta_{nor}}A_1^2\exp(-j\Delta kz) - \frac{\alpha_2}{2}A_2 \tag{2.45}$$

$$\frac{dA_1}{dz} = -j\sqrt{\eta_{nor}}A_1^*A_2\exp(j\Delta kz) - \frac{\alpha_1}{2}A_1 \tag{2.46}$$

where the small signal normalized conversion efficiency (in units of 1/W-m^2) is given by:

$$\eta_{nor} = \kappa^2\nu^2 \tag{2.47}$$

It is instructive to examine the solutions to the coupled mode equations and efficiency expressions in several limits.

2.4.1 Undepleted Pump Limit

The simplest way to characterize second-order nonlinear devices is a low-power, continuous-wave (CW), SHG tuning curve, which is a measurement of the SHG efficiency as a function of phase mismatch, where the latter is varied by tuning either the sample temperature or the wavelength at the fundamental (also known as the pump) frequency. This tuning curve reveals information about the mixing efficiency, uniformity of phasematching (and thus the quality of the fabrication process), and the number of modes interacting in the structure. In the low conversion efficiency limit, the pump wave can be considered undepleted (i.e. the fractional change in its level is less than 20 %). If we also neglect the waveguide propagation loss, the coupled mode equations become:

$$\frac{dA_2}{dz} = -j\sqrt{\eta_{nor}}A_1^2\exp(-j\Delta kz) \tag{2.48}$$

$$\frac{dA_1}{dz} = 0 \tag{2.49}$$

Straightforward integration yields the following solution for the nonlinear conversion efficiency η:

$$\eta_{\mathrm{LOSSLESS}} = \frac{P_2(L)}{[P_1(0)]^2} = \eta_{nor}L^2\mathrm{sinc}^2(\Delta kL/2) \tag{2.50}$$

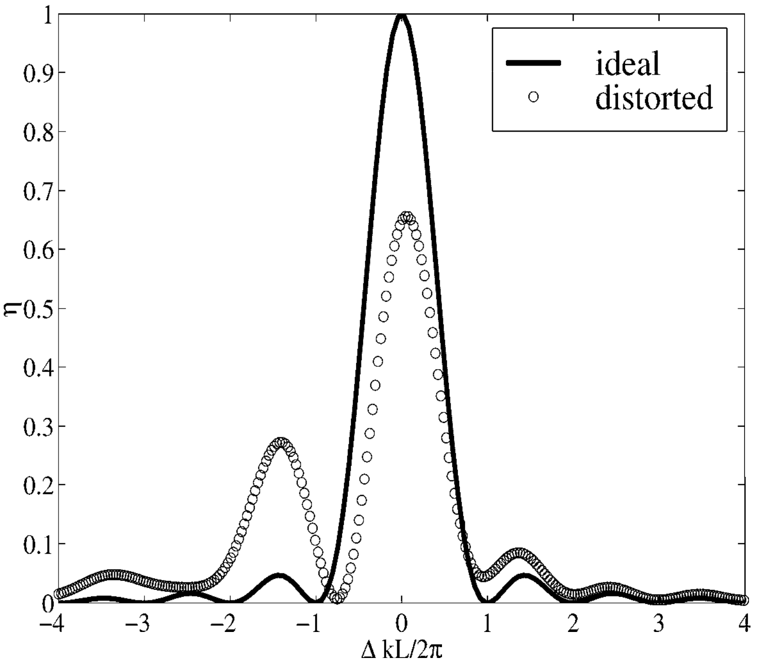

Figure 2.2: Plot of second harmonic generation tuning curve for ideal and distorted phasematching distribution

The solution in equation (2.50) assumes that the phase mismatch Δk is constant throughout the length of the waveguide. The effect of position-dependent mismatch is broadening of the width of the curve and reduction of its peak amplitude. The area under the curve is determined by the square of the length of the quasi-phasematched region and the strength of the spatial overlap of the interacting modes. In the ideal case, this area is:

$$\text{area} = \int_{-\infty}^{\infty} \eta_{nor} L^2 \text{sinc}^2(\Delta k L/2) d(\Delta k L/2) = \eta_{nor} \pi L^2 \tag{2.51}$$

The effect of spatially varying phase mismatch is the redistribution of area as a function of $\Delta k L/2$, since different frequency components will satisfy the phasematching condition at different points along the waveguide. Helmfrid et al derive this result in [23]. For example, a tuning curve from an ideal device is plotted in Figure 2.2 along with one from a second waveguide (of the same length) with non-uniform phasematching along its length. In this particular case, the extra phase mismatch is zero at the beginning of the device, and increases quadratically to 7.5π at the end. The areas under the curves are identical, indicating that the modal overlap and device length are the same in both waveguides. The distortion arises from non-uniformities in the linear properties of the second waveguide (refractive index, temperature, etc.) along its length. This type of measurement is very useful when trying to determine the source of anomalous device behavior. The area under the curve and the shape of the curve allow independent measures of spatial overlap and waveguide uniformity.

It should be noted that there is no second harmonic field at the beginning of the waveguide. As such, the phase of the second harmonic with respect to the fundamental is free to take on any value. Only one phase difference ($\pi/2$), results in unidirectional power transfer from the fundamental to the second harmonic, hence the generated second harmonic field takes on this value. Any distortion causing phase mismatch along the device length disturbs this fixed relationship. In the undepleted pump limit, the fractional change in the pump power is small, so the effect of this disturbed phase difference is distortion in the tuning curve, as described previously. In the strongly depleted limit, however, deviation of the relative phase from $\pi/2$ causes power to flow from the second harmonic back to the fundamental, limiting the observable level of pump depletion. This situation is further examined both theoretically and experimentally in Chapter 4.

Real devices usually have non-negligible losses. When loss is included, the efficiency expression becomes more complicated:

$$\eta = \eta_{nor} \frac{\exp(-4\alpha_1 L) + \exp(-2\alpha_2 L) - 2\cos(\Delta k L)\exp(-[\alpha_2 + 2\alpha_1]L)}{(\alpha_2 - 2\alpha_1)^2 + \Delta k^2} \tag{2.52}$$

Usually we are interested in determining the normalized conversion efficiency η_{nor}. Since it is often easy to measure power at the two wavelengths at the device output, it is instructive to define a measured conversion efficiency as:

$$\eta_{meas} = \frac{P_{2\omega}(L)}{[P_\omega(L)]^2} = \eta_{nor}\frac{\exp(-4\alpha_1 L) + \exp(-2\alpha_2 L) - 2\cos(\Delta k L)\exp(-[\alpha_2 + 2\alpha_1]L)}{\exp(-4\alpha_1 L)[(\alpha_2 - 2\alpha_1)^2 + \Delta k^2]} \tag{2.53}$$

In the special case where $\alpha_2 = 2\alpha_1$ and $\Delta k = 0$, the expression simplifies very nicely to:

$$\eta_{meas} = \eta_{LOSSLESS} = \eta_{nor} L^2 \mathrm{sinc}^2(\Delta k L/2) \tag{2.54}$$

This specific situation is encountered in many real devices, hence the above expression is very useful in practice.

2.5 Conclusion

The basic physics underlying the operation of optical frequency mixers has been presented in this chapter. The coupled mode equation formalism provides a useful framework with which many mixing interactions can be analyzed. The next chapter describes the design and fabrication of the mixing devices, where the low-power CW SHG tuning curve described in Section 2.4.1 serves as a useful measure of device efficiency and quality.

Chapter 3

Device Structure and Fabrication

The basic physics underlying the operation of optical frequency mixers has been well understood for a long time, as evidenced by the early proposal of quasi-phasematching [21, 22]. The successful implementation of these ideas as practical devices has required many years of materials science and device engineering. This chapter describes the development of the fabrication processes used in this research work, along with the important engineering improvements that enabled the experimental results presented in later chapters, including demonstration of the most efficient nonlinear frequency mixers reported to date.

3.1 Choosing the Right Material

Many factors must be considered when choosing a material system for development of practical devices. Maximizing the mixing efficiency described by equation (2.47) requires a large nonlinear coefficient and strong optical confinement. The former is an intrinsic material property, and the latter can be provided by creation of a waveguide in the nonlinear substrate. A wide transparency range allows a given material to be used in a variety of mixing interactions. Perhaps the most important property that allows for the systematic study and development of a material into a commercially viable product is the availability of low-cost, high-quality substrates.

Lithium niobate is a ferroelectric, uniaxial oxide that has many attractive properties. Its large piezoelectric coefficient has led to its extensive use in radio frequency surface acoustic wave filters [24]. In their simplest form, these devices consist of a pair of interdigital electrodes deposited on the substrate surface. Only signals whose electrical frequency matches the resonant frequency of the circuit formed by the electrodes can travel from the input to the output, hence the device behaves as an electrical filter. This filter structure is widely used in a variety of electronic devices, such as cellular phones. Lithium niobate also has a large electro-optic coefficient, and is used to make guided wave interferometric devices that allow for imposing electronic data onto optical signals [25]. These and other applications have led to large-scale production of quality lithium niobate substrates.

The basic material properties of lithium niobate also make it well suited to nonlinear optical applications. Its maximum nonlinear coefficient of $d_{33} = 27$ pm/V compares favorably to that of other materials, it is transparent from the ultraviolet to the mid-infrared (325-4500 nm), and a variety of waveguide fabrication techniques have been developed for it. Implementation of quasi-phasematching in guided wave structures in lithium niobate has been developed in the Byer/Fejer group at Stanford [13, 26, 27, 28] and several other groups around the world [29, 30, 31], over the past fifteen years, hence a large body of processing knowledge exists in the literature. The next few sections involve description of the processing techniques used in this research, building from the work of previous Stanford students and including the improvements particular to this dissertation.

3.2 Electric-Field Poling

As discussed in Section 2.3.1, quasi-phasematching involves a periodic inversion of the sign of the second-order nonlinear coefficient. While the term is a misnomer (typically the materials contain no iron), ferroelectrics are materials exhibiting a spontaneous electric dipole moment, analogous to magnetic dipoles in ferromagnetic materials [32]. There are several ways in which to achieve the required periodic inversion of the sign of the nonlinearity, including modulation of heat input during laser-heated pedestal growth [33], direct writing with an electron beam [34], titanium indiffusion [35, 36], and post-growth electric-field poling using lithographically patterned electrodes. When an electric field higher than a characteristic coercive field is applied to a ferroelectric, the orientation of the spontaneous polarization is reversed, which causes the reversal of the sign of odd-rank tensor properties (such as electro-optic, piezoelectric, and nonlinear optic coefficients). The electric-field poling process, conceived independently by groups in Japan [37] and at Stanford [38], has proven to be very versatile and compatible with standard microfabrication technology, due largely to the advent of a crystal growth technique that produces uniform, single-domain wafers [39, 40]. The electric-field poling technique developed at Stanford in the early 1990s has continually evolved since that time [41]. The wafer is clamped in a Plexiglas fixture, with chambers on either side filled with a liquid electrolyte (typically a saturated solution of lithium chloride in deionized water). High voltage is applied to the electrolyte (and the wafer) through metal contacts on the outside of the fixture (Figure 3.1). The periodic pattern is achieved by defining a set of electrodes on the wafer surface prior to the application of high voltage, with the unpatterned area shielded by a dielectric. It has been found that metal electrodes directly deposited on wafer surface are the most effective at producing high quality domain patterns, particularly for short periods [42]. However, subsequent formation of waveguides on the surface requires removal of the electrodes to allow for further patterning. Since it is difficult to completely remove metals deposited on the lithium niobate surface without leaving behind a contaminated surface layer, an alternative approach was developed for waveguide devices. Rather than depositing a periodic array of conductors on the surface to serve as electrodes, an array of dielectric strips can be used to insulate parts of the wafer, leaving a series of strips of exposed lithium niobate to serve as electrodes. Electrical contact to the +z surface is made only in the areas without the photoresist insulator (Figure 3.1). The backside of the wafer is not patterned. A systematic study of the nucleation and growth of domains in lithium niobate has led to a numerical model for the highly nonlinear relationship between the velocity of the domain walls and the applied electric field [43, 44]. It has been observed that domains nucleate on the +z surface at the edges of the electrodes (where the local electric field

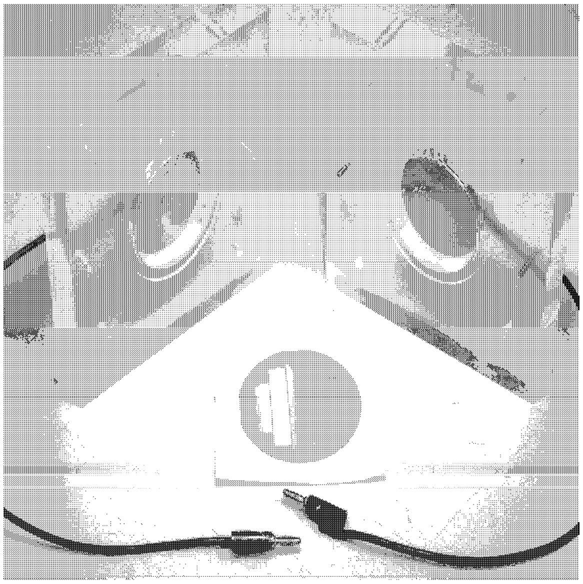

Figure 3.1: Photograph of a typical poling fixture, consisting of Plexiglas blocks between which the 3-inch-diameter wafer (shown patterned with photoresist) is clamped. Chambers on either side are filled with liquid electrolyte that provides a conduction path between the gold-plated electrodes and the wafer surface.

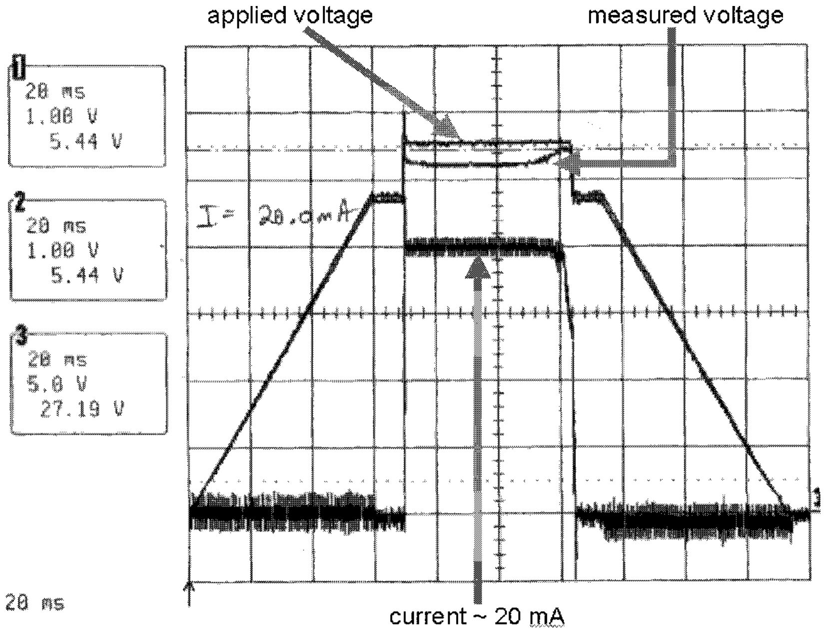

Figure 3.2: Oscilloscope trace showing typical current and voltage waveforms resulting from electric-field poling of a lithium niobate wafer of three inch diameter.

is highest) then propagate straight down to the opposite face before growing inward, merging, then finally growing outward from the electrode edges. The model allows for the design of optimized electrode widths and voltage waveforms to produce a desired domain pattern. A typical waveform is shown in Figure 3.2. The wafers used in this work have a thickness of 0.5 mm, such that application of a coercive field of 21 kV/mm requires 10.5 kV. This voltage is obtained by amplifying a low voltage (provided by an arbitrary-waveform generator) with a high voltage amplifier (with a gain of 2000). The applied electric field is initially ramped up slowly from zero to a value slightly below the coercive field. This ramp is followed by a short spike of field above the coercive value, which is designed to aid in the nucleation or initial formation of inverted domains. The pedestal at an intermediate field before this spike serves only to minimize the change in field during the spike, where dielectric breakdown is most likely. The domain growth takes place in the central flat section, where the applied field is slightly above the coercive value, such that current begins to flow. The length of this segment is determined by the area to be poled. A calculation of this time for a typical wafer is given below:

$$\text{time} = \frac{P_s A_p}{I_p} = \frac{(78\ \frac{\mu\text{C}}{\text{cm}^2})(13\ \text{cm}^2)}{21\ \text{mA}} \approx 50\ \text{ms} \tag{3.1}$$

where P_s is the spontaneous polarization charge density associated with the individual dipole moments, A_p is the area to be poled, and $I_p \approx 20$ mA is the poling current. Poling is done in a "current controlled" regime, where the current is clamped at the current limit of the operational amplifier. This clamping is evidenced by the voltage measured across the wafer, which drops below the nominal value when the current exceeds the limit of the high voltage amplifier. Towards the end of the central segment, when sufficient charge is delivered to invert the domains in the exposed area of the wafer, the current "self-terminates", and the measured voltage rises to equal the applied value. A detailed model for this process is presented elsewhere [44]. After poling the material is known as periodically-poled lithium niobate, or PPLN, a very useful bulk nonlinear optical material.

Various kinds of poling defects can reduce the effective interaction length, and thus the conversion efficiency. The most common defect is the merging of adjacent domains, known as a "run-together", which is equivalent to having a missing domain in the quasi-phasematching structure. As derived in [9], if the fraction of domains having the wrong sign is denoted as f, the efficiency drops to:

$$\eta_{\text{missing domains}} = (1-2f)^2 \eta_{nor} \tag{3.2}$$

Hence if only 10 % of the domains have the wrong sign, the efficiency drops to 64 % of the ideal value. The first step in fabrication is photolithography, where photoresist is spun onto the wafer surface and exposed to ultraviolet light through a chromium mask. Many poling defects are caused by particles in the photoresist that serves as a dielectric during high voltage application. Care and cleanliness during lithography can largely mitigate this problem. Run-togethers also arise when domain lengths vary as they grow in the direction parallel to the grating vector (Figure 3.3). If two adjacent domains have some variability in their length, there is some probability

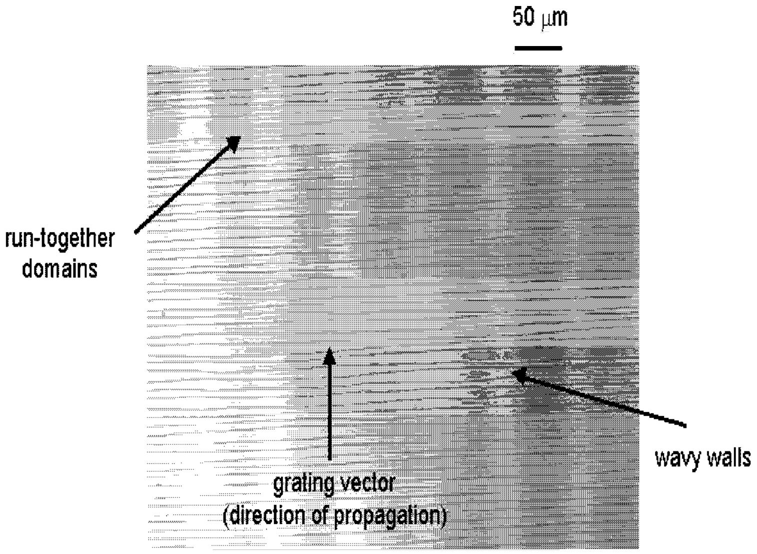

Figure 3.3: Micrograph of PPLN surface after etching in hydrofluoric acid. Domains of reversed polarity are etched, while original domains are not, such that domain boundaries are revealed as lines. Wide stripes result in wavy domain boundaries and occasional run-togethers.

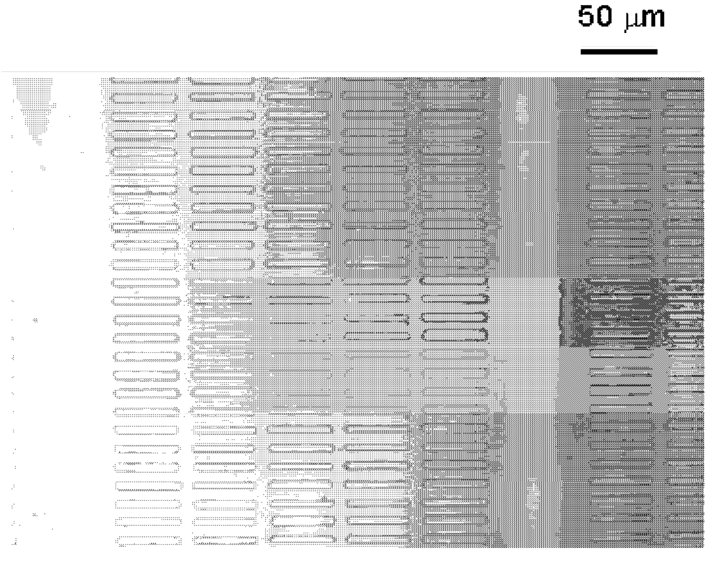

Figure 3.4: Segmentation of grating segments results in much higher poling quality. The domain walls are very straight, and run-togethers are mostly eliminated.

that they both vary in the same direction, leading to merging of the walls. Using segmented gratings helps avoid this phenomenon (Figure 3.4) [45]. This technique involves using very narrow grating segments, such that the domain lengths are not allowed to vary significantly over the length of a device. This technique has been used to significantly improve the poling quality over the previous generation of devices, and is also very useful in the implementation of complex interferometric structures such as the optical frequency balanced mixer [46] and novel nonlinear optical lens structures [47].

3.3 Annealed Proton-Exchanged Waveguides

The periodic poling process results in a grating that compensates for the phase velocity mismatch caused by the dispersion inherent to the material. As discussed in Section 2.3.1, it is this quasi-phasematching that enables efficient use of the entire length of the crystal. Waveguides dramatically enhance the conversion efficiency of three-wave mixers by supporting transverse spatial modes of small spot size over long distances. Various approaches to waveguide formation in lithium niobate have been investigated over the past twenty years, including indiffusion of titanium [31, 48], protons [49], and zinc [50]. Among these methods, annealed proton-exchange (APE) presents an attractive combination of strength of confinement (measured by the refractive index step), low propagation loss, and ease of fabrication.

Photorefraction is a phenomenon where light propagating in a material results in a redistribution of charge around the beam, producing a space-charge field that induces a nonuniform refractive index profile through the electro-optic effect [51] that causes instability in the phasematching condition. Waveguides fabricated using APE are less photorefractive than those produced by titanium indiffusion, but more so than those made by indiffusion of zinc. On the other hand, APE provides a larger index step than either titanium or zinc. Given that the primary goal of this work was the demonstration of high mixing efficiency (which is obtained through strong optical confinement), and the fact that photorefraction can be largely mitigated by operating the devices at moderate temperatures ($\approx 100°\mathrm{C}$), APE was the best choice.

The initial exchange process involves immersion of the lithium niobate substrate in an acid melt, where H^+ ions (protons) diffuse into the material and Li^+ ions diffuse out, resulting in a "step function" of protons on the surface. The protonated material exhibits a slightly larger extraordinary refractive index than the substrate ($\Delta n_e \approx 0.09$ @ $\lambda = 1550$ nm), and is known as a proton-exchanged (PE) waveguide. A variety of acids have been used to form PE waveguides in lithium niobate, including benzoic [49], sulfuric [52], and pyrophosphoric [53], among others. Benzoic acid is the most commonly used melt. It is a relatively weak acid, is non-toxic, exists as a powder at room temperature, and has a melting point of 122°C. All of the PE done in this work used benzoic acid at an exchange temperature of 160°C. This temperature is high enough to ensure that the acid is fully molten and that the exchange proceeds at a reasonable rate.

Although proton-exchanged waveguides provide strong optical confinement, they tend to be very lossy (≈ 1 dB/cm) [54], and exhibit very weak nonlinearity [19]. As such, these devices are almost completely useless for mixing applications, since the launched waves get scattered, and no mixing takes place. The origin of this "dead layer" lies in the complicated phase diagram of PE:$LiNbO_3$ [55]. During the initial exchange, a variety of phases can be produced, depending on the choice of processing conditions. For the parameters used in this work, the phase of the initially exchanged layer is one exhibiting no nonlinearity.

Annealing makes proton-exchanged waveguides much better suited to nonlinear mixing. This process involves heating the crystal after exchange, such that protons diffuse from the surface into the substrate, turning the proton profile from a step function into one with a peak at the surface that decreases monotonically into the substrate. Using this process, the lossy (β phase) waveguide can be transformed into a low-loss (α phase) structure. This low-loss phase exists in regions where the index step and proton concentration are reduced below 25 % of the as-exchanged value [54]. This transformation is accompanied by partial recovery of the nonlinear coefficient in the initially exchanged layer, while the deeper region into which the tail of the profile diffuses retains the substrate nonlinearity. Varying the initial exchange depth and annealing conditions allows for engineering of waveguides to support a desired number of spatial modes for a given mixing interaction.

This engineering of waveguide properties requires a good understanding of the evolution of the proton concentration in the substrate during fabrication. An extensive study of the diffusion of protons in lithium niobate has revealed that this material system exhibits concentration-dependent diffusion, where the shapes of the diffused profiles cannot be described by simple analytical expressions. Detailed measurements have led to an empirical model for the dependence of the diffusion coefficient on the proton concentration, where it was also determined that the index profile is essentially linearly proportional to the proton concentration. A second tool needed in order to engineer waveguides for nonlinear optical applications is knowledge of the dependence of the refractive index step on wavelength, allowing for accurate calculation of the spatial profiles and effective indices of the transverse modes supported by the waveguide. This phenomenon has also been well studied, where a reliable Sellmeier relationship has been obtained from data on the effective indices of modes of waveguides fabricated under a variety of conditions, measured by the prism coupling method. Both the diffusion and Sellmeier models are described in detail elsewhere [56]. These models for annealed proton-exchanged (APE) waveguides in lithium niobate have been used to accurately predict the behavior of a variety of nonlinear optical devices [27, 28, 57]. The next section describes the use of these models in the optimization of the frequency mixers developed in this dissertation.

3.3.1 Optimization of APE Waveguides

As discussed in Chapter 2, the efficiency of three-wave mixing interactions in a waveguide is largely determined by the spatial overlap of the interacting modes. The expression for the overlap integral is repeated here for convenience:

$$\nu = \int_{-\infty}^{\infty}\int_{-\infty}^{\infty} \bar{d}(x,y)E_1(x,y)E_2(x,y)E_3^*(x,y)dxdy \tag{3.3}$$

The peak value and distribution of the refractive index profile define the shapes of the electric field spatial modes, whose overlap is represented by ν. In an ideal situation, the index step is very high, such that the interacting modes are well confined and the electric field intensity is maximized. This requirement must be balanced with the fact that the material must be annealed into a low-loss phase in order to have a finite nonlinearity and non-zero mixing efficiency. Hence the materials optimization requires maintaining the maximum possible peak index (for strong confinement) while still being in the α phase. A further consideration is that of fabrication tolerances. The waveguide fabrication process involves lithographic patterning of channels in a thin ($\approx$ 500 Å) SiO_2 film sputtered on the PPLN surface. Traditional lithography for microelectronics involves patterning of two-dimensional structures whose features are comparable in size in both dimensions. Channel waveguide lithography for nonlinear mixers requires creation of long (several centimeter) lines with much smaller ($\approx$ 10 μm) widths. Although high fidelity features of these widths can be relatively easily obtained using conventional lithography, maintaining the accuracy of these dimensions over several centimeters is very challenging. In this regime, it is advantageous to design the waveguides to be "dimensionally non-critical" [58, 59], meaning that the phasematching wavelength is insensitive to variations in waveguide dimensions, particularly the width. The large range of times and temperatures available for the proton-exchange and annealing processes presents a broad parameter space for optimization.

Previous work at Stanford has led to an optimized design for APE waveguides operating in the 1550 nm wavelength region [13, 16]. This design requires an initial proton-exchange depth of $\approx$ 0.8 μm produced by 15 hours of exchange in benzoic acid at 160°C, followed by annealing for 26 hours at 328°C. Modeling of the diffusion process reveals that this combination of proton-exchange and annealing leads to a waveguide whose entire profile is in the low-loss α phase discussed above. A waveguide mask width of 11.5 μm was found to be non-critical under these conditions, producing a mixer with a normalized conversion efficiency of $\eta_{nor}L^2$ =1200 %/W for a 56-mm-long QPM grating, such that η_{nor}=38 %/W-cm^2.

An important point to note is that this optimization results in a waveguide that supports roughly four modes at the fundamental wavelength. The grating formed during periodic poling allows for quasi-phasematching of a single spatial mode at the fundamental wavelength with another at the second harmonic. In order to have

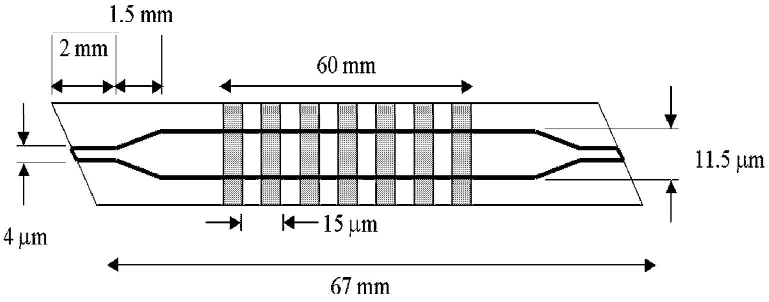

Figure 3.5: Schematic diagram of non-critical waveguide design (not to scale).

efficient mixing, some means of exciting only one mode at the fundamental wavelength is needed. One effective solution is to implement a mode filter and adiabatic taper at the waveguide input [57]. The filter is a waveguide that is single-moded, such that any light coupled into it is in the lowest order spatial mode. The linear taper in width slowly transforms the mode into the lowest order shape in the multimoded mixing region. A schematic top view of the resulting device is shown in Figure 3.5. The waveguide width is tapered from the single-moded 4 μm to the optimized 11.5 μm in the mixing region.

Like the electric-field poling process, waveguide fabrication begins with photolithography. The non-critical design described above greatly loosens tolerances on process quality, however these tolerances scale inversely with device length. Increasing the waveguide length to the maximum possible 67 mm in a 3-inch-diameter wafer demands some improvement in process uniformity, including optimization of the temperature uniformity of the proton-exchange bath and annealing oven. The proton-exchange bath consists of a Pyrex$^{\mathrm{TM}}$ beaker containing the benzoic acid placed in a large bath of silicone oil. The cast iron pot containing the oil is attached to a standard laboratory hotplate, where both the oil and acid are stirred at roughly 200 rpm using magnetic stirring bars. The outside of the iron pot is insulated using multiple layers of fiberglass blanket, with a Fiberfrax$^{\mathrm{TM}}$ lid on the top. Samples are placed into the acid using a Teflon$^{\mathrm{TM}}$ holder suspended from a Teflon$^{\mathrm{TM}}$ lid. This configuration produces very good temperature uniformity for samples with lengths up to 67 mm. The annealing process requires a much different environment. Samples are annealed at 328°C in

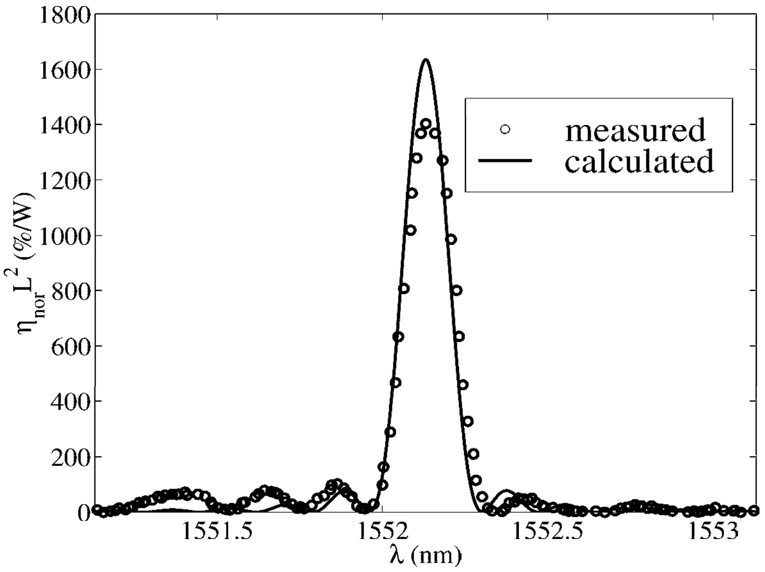

Figure 3.6: Low-power, CW SHG tuning curve for optimized APE waveguide.

air, so stirred liquid baths are not suitable in this case. A three-zone tube furnace is a much better choice, where the multiple temperature controllers flatten out the parabolic temperature profile that is characteristic of a single central zone controller. One issue with this arrangement is that although the overall profile is much flatter, the superposition of the temperature profiles generated by the individual heaters results in a small-amplitude ripple in temperature, which can again lead to nonuniformity along the device length. Placing the device on a highly thermally conductive sample holder (namely a copper block electroplated with gold) largely eliminates this problem.

As a result of these processing improvements, longer and more efficient APE PPLN waveguides have been fabricated. Figure 3.6 shows a low-power CW second harmonic generation tuning curve for such a device. The QPM grating length is 59.5 mm, and the overall device length is 66.5 mm. The peak efficiency of 1400 %/W corresponds to a normalized efficiency of $\eta_{nor} = 38$ %/W-cm^2, identical to that of the previously demonstrated shorter devices. The symmetric sinc^2 shape of the data indicates that all of the fabrication processes were very uniform, and the FWHM of 0.18 nm is very close to the theoretical value, as evidenced by the good agreement with the

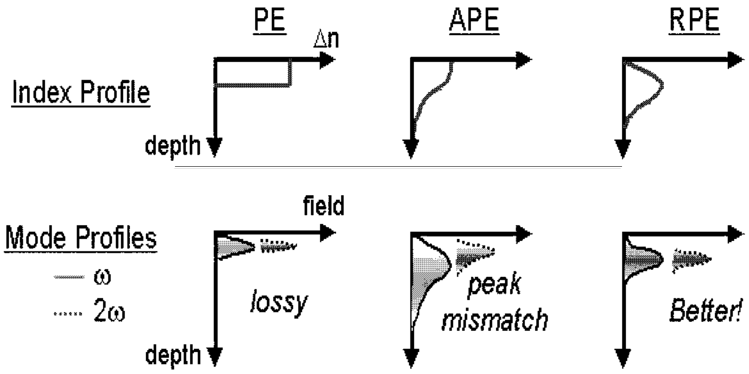

Figure 3.7: Comparison between proton-exchanged (PE), annealed proton-exchanged (APE), and reverse proton-exchanged (RPE) index and mode profiles in the depth dimension.

calculation. This particular device was used to observe 99 % pump depletion in a quasi-CW SHG experiment, as will be described in Chapter 4.

3.4 Reverse Proton-Exchange

The APE waveguides described thus far are reasonably efficient and have been used in a variety of device and system demonstrations [60]. This section describes the implementation of buried waveguides using a reverse proton-exchange technique. This approach leads to a significant increase in normalized conversion efficiency over APE, opening the door to high gain parametric amplifiers with relatively modest pump power levels.

3.4.1 Comparison of Waveguide Fabrication Techniques

Near-degenerate three-wave mixing involves the interaction of waves differing in wavelength by a factor of two. Figure 3.7 shows a comparison of the index and mode profiles produced using different fabrication methods. Proton-exchanged waveguides produce strong confinement and symmetric modes, however they are lossy and exhibit very low nonlinearity. Annealing lowers the peak index (which reduces the loss) and pushes the modes away from the dead layer, resulting in the reasonably high efficiency discussed in Section 3.3.1. Nevertheless, the interacting electric field profiles are asymmetric, so that the peaks of the modal fields lie at different depths, and still sample the initially exchanged layer, such that the overlap integral ν in equation (3.3) is not maximized. The symmetric index profile in the rightmost part of Figure 3.7 greatly improves the situation. The maxima are forced to coincide, increasing the spatial overlap and thus the conversion efficiency, while the entire profile is in the low-loss phase. One approach to making the index profile in APE waveguides more symmetric is to remove some protons from the waveguide surface. This "reverse proton-exchange" (or RPE) can be accomplished by immersing the sample in a lithium-rich melt such that protons diffuse out of the PPLN and are replaced by lithium ions. Several groups have explored this process and observed its attractive properties, including recovery of the nonlinear coefficient [55, 61] and symmetry of spatial modes [62]. The former increases the mixing efficiency, while the latter allows for engineering of a waveguide mode that matches that of standard optical fiber, reducing the insertion loss in a fiber pigtailed device.

3.4.2 Reverse Proton-Exchange Chemicals and Apparatus

In order to draw protons out of and recover the substrate properties in the surface region, the APE structure must be immersed in a lithium-rich melt. Various melts have been investigated for this purpose. Lithium benzoate is a natural candidate, as it has been shown that very small amounts of this material added to a benzoic acid melt can slow the rate of forward proton-exchange [63]. A lithium benzoate concentration of 5 mol.% completely stops the exchange, while mixtures with concentrations larger than this result in reverse exchange, with the excess lithium diffusing into the substrate and forcing the outdiffusion of protons. This approach has been successfully implemented [62], however the differential evaporation of the benzoic acid and lithium benzoate results in a time-dependent melt composition, demanding the use of a sealed container in order to obtain consistent results, which makes the approach somewhat inconvenient.

Other lithium salts would also appear to be good choices for reverse exchange media. Lithium nitrate ($LiNO_3$) has been tried, however when used alone as a counter diffusion melt, it has been found to damage the sample surface [62]. Damage is avoided by using mixed nitrate melts with smaller amounts of lithium. Potassium nitrate (KNO_3) and sodium nitrate ($NaNO_3$) can be combined with $LiNO_3$ to form a eutectic melt with a melting point of 130°C. Sodium and potassium have been found to have no effect on the proton distribution, so the other nitrates simply serve as carriers to dilute the lithium concentration. Korkishko et al [64] have demonstrated promising results using a melt in a mol.% ratio of $LiNO_3$ (37.5) - KNO_3 (44.5) - $NaNO_3$ (18.0). Secondary ion mass spectrometry (SIMS) of devices that had undergone reverse exchange after APE showed a surface region with lithium concentrations similar to those in the bulk, indicating recovery of the substrate properties. Hence this melt composition was chosen for the studies in this work.

As discussed in section 3.3.1, temperature uniformity during processing is critical to maintenance of the phasematching condition over the length of a device. Preliminary modeling of the RPE process indicated that in order for the reverse exchange to proceed at any reasonable rate, the process temperature needs to be above 300°C. This temperature is too high for the silicone oil bath approach used in the PE process, as most organic liquids cannot survive these temperatures. A better apparatus is a vertical tube furnace, where the melt components are placed in a quartz beaker, which is then placed at the center of the tube and heated in air. Stirring is done by mechanically rotating a quartz rod placed in the melt from the top.

3.4.3 Diffusion Characterization using Planar Waveguides

The optimization of APE structures discussed in Section 3.3.1 was enabled by a good understanding of the diffusion process. Performing a similar design optimization for reverse exchanged structures requires a good understanding of the counter diffusion process. The forward diffusion model is a natural starting point for a reverse diffusion model, with the notable difference that in the former case, the slope of the concentration profile is set to zero at the surface, while in the latter case the concentration itself is set to zero at the surface. In order to test the ability of the forward model to predict reverse diffusion behavior, some measurable diagnostic is required.

The diffusion model presented in [56] was developed using the prism coupling technique [65] on planar waveguide samples. This method involves pressing the planar waveguide surface against one face of a triangular prism, where a laser beam is launched through one of the other faces, and the transmitted light is detected through the third. As the angle of incidence is varied, dips are detected in the transmitted signal, as evanescent coupling takes place through the small air gap in between the prism and sample. This coupling occurs at particular angles corresponding to the finite set of modes supported by the waveguide at the incident wavelength. Given this set of modes, the index profile can be reconstructed using the well-known Inverse Wentzel Kramers Brillouin (IWKB) method [66]. In reverse exchanged waveguides, the surface refractive index step is very close to zero by design. Hence prism coupling is not an effective diagnostic in this case, as the incident laser field must tunnel through a barrier in order to excite the waveguide modes.

Since we are removing protons from the substrate during reverse exchange, a measure of the total number of protons in the material is a useful metric. One way to measure this number is to observe the optical absorption in the material in the wavelength range between 2750 nm and 2950 nm [67]. This absorption band results from excitation of the of the O-H bonds formed in the $LiNbO_3$ crystal during proton-exchange. The area under such an absorption spectrum is a measure of the number of protons in the material. The difference in this number for a sample before and after proton-exchange is a measure of the number of protons introduced during the exchange (the as-grown substrate contains some small number of protons that are introduced during crystal growth). A plot of the total number of protons as a function of reverse exchange time and temperature provides a useful metric for comparison with results predicted by the modified forward diffusion model. In order to perform this comparison, a series of planar annealed proton-exchanged waveguides with different initial PE depths was prepared. These samples were reverse exchanged several times, where the absorption was measured after each step to determine the number of protons remaining in the substrate. The plot in Figure 3.8 shows a typical

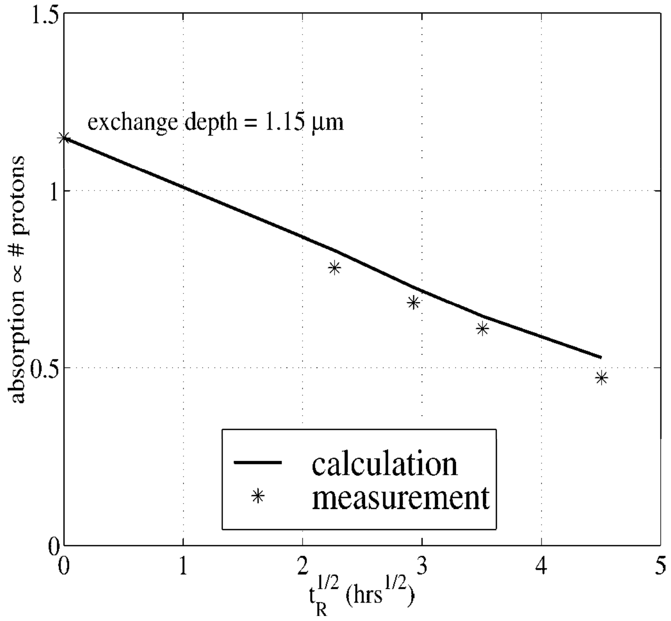

Figure 3.8: Absorption of planar waveguide sample after various reverse exchange times. Reasonable agreement with the calculation is observed.

set of data, along with a calculation performed using the modified forward diffusion model. The abscissa is presented in units of $\sqrt{t_R}$, where t_R is the reverse exchange time. The agreement of the data with the model justifies its use in designing channel waveguides.

3.4.4 Optimization of RPE Channel Waveguides

Having established some confidence in a model for describing the RPE process in planar structures, channel waveguides optimized for mixing efficiency can be designed. Given the fairly large number of design parameters (proton-exchange depth, waveguide width, annealing time and temperature, reverse exchange time and temperature), a set of design rules is needed in order to simplify the process. The primary design constraint is that the peak refractive index step be slightly less than 25 % that of the as-exchanged material, in order to ensure that the entire waveguide is in the low-loss α phase while maintaining maximum optical confinement. Since the reverse exchange process results in the removal of protons from the substrate surface, the initial exchange can be deeper than that used in the optimized APE structures presented in Section 3.3.1. Conversely, the annealing time can be reduced, as the RPE process contributes to the reduction in peak index step that is accomplished by annealing alone in the APE case. A secondary consideration is that of non-critical design. As in the APE devices, it is advantageous to choose a set of waveguide parameters (mask width in particular) such that the phasematching condition is insensitive to first order variations in their values. Finally, the effect of the "dead layer" must be addressed. In APE guides, the parts of the electric fields that sit in the initially exchanged region do not contribute to the mixing process. The RPE process has been observed to revive the nonlinearity of this region [61], such that the calculation of modal overlap can take the entire field profiles into account.

With these guidelines, various designs were simulated in order to find an optimum set of parameters. Figure 3.9 compares the index profiles of optimized APE and RPE waveguides. The peak index is slightly below 25 % of the as-exchanged value in order to minimize loss and maximize confinement in both cases. The RPE profile provides slightly higher optical confinement, as the slopes of the profile on either side of the peak are much steeper than the long tail of the APE profile. Figure 3.10 shows plots of electric field profiles at the fundamental and second harmonic frequencies (for a fundamental wavelength of 1550 nm) in the depth dimension for optimized APE and RPE waveguides. The peaks are clearly closer together in the RPE case, where the second harmonic mode is pushed down into the substrate. Neglecting the effect of the dead layer, the overlap integral ν (equation (3.3)) in the RPE case is roughly twice that of the APE modes. Assuming that there is no recovery of the dead layer in the APE guide and full recovery in the RPE guide, the ratio is close to three. Hence it is the combination of both factors that makes the RPE process very attractive. The RPE waveguide calculation is for a proton-exchange depth of 1.15 μm, annealing time of 8 hours at 328°C, and reverse exchange time of 10.25 hours at the same temperature. The waveguide width of 8.25 μm is such that the phasematching wavelength is calculated to be non-critical to variations in this width (Figure 3.11).

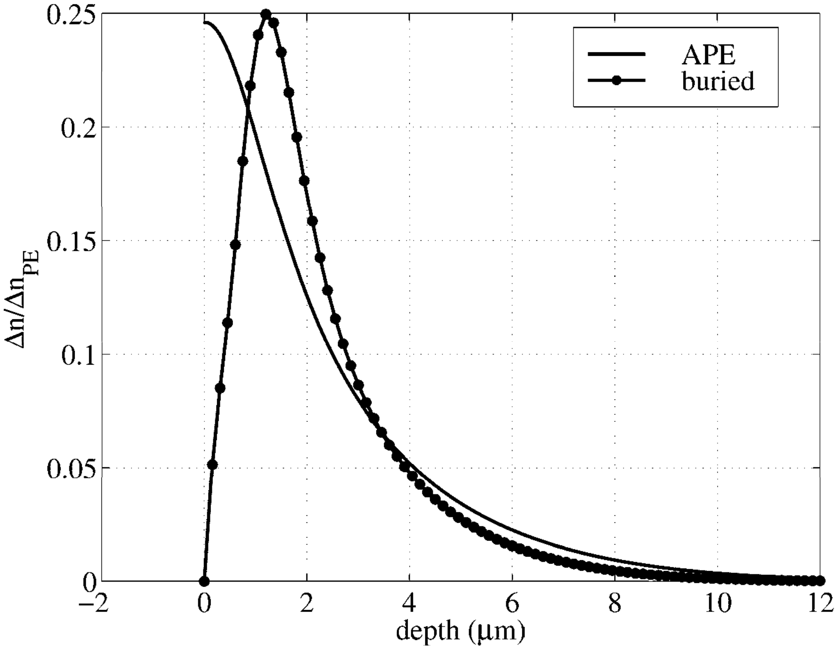

Figure 3.9: Comparison of optimized APE and RPE (buried) index profiles. The peak index step is slightly less than 25 % of the as-exchanged value in both cases.

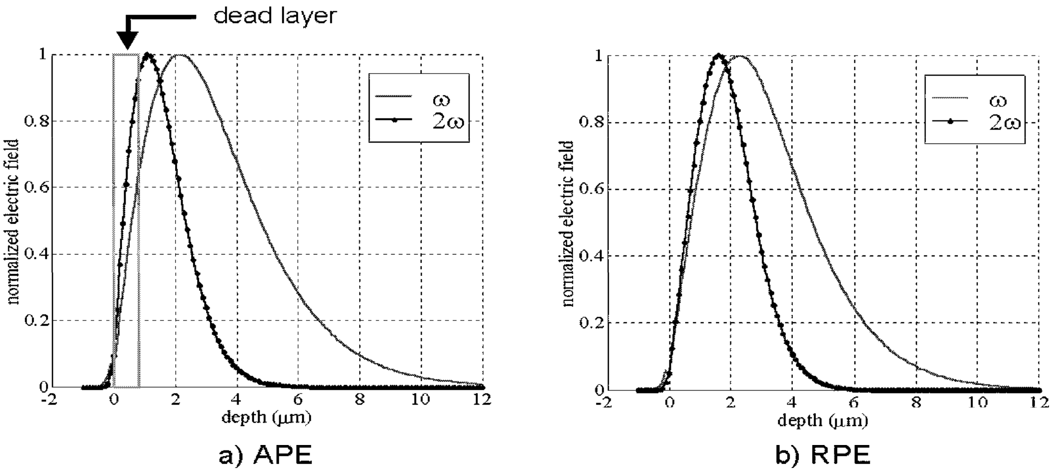

a) APE

b) RPE

Figure 3.10: Normalized electric field profiles for a)APE and b)RPE waveguides. The dead layer is outlined in the APE figure.

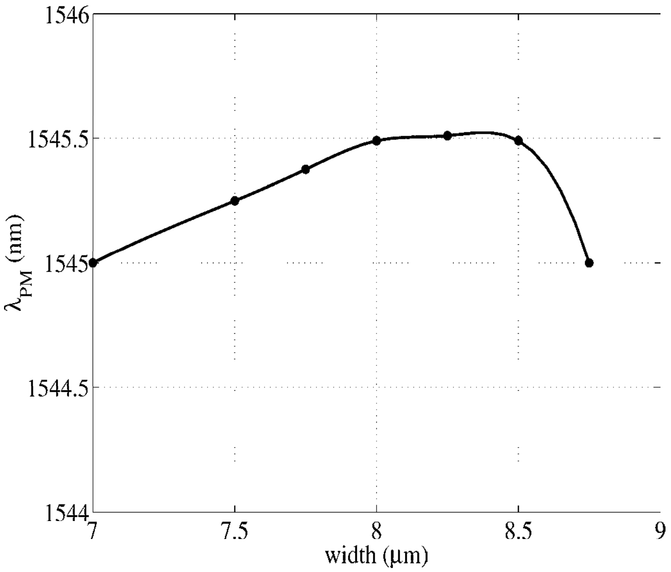

Figure 3.11: Plot of calculated phasematching wavelength vs waveguide width for RPE waveguides, illustrating non-critical point near 8.25 μm. The line is shown only to guide the eye.

3.4.5 Measured Results

Based on the promise of the above calculations, a waveguide sample was fabricated. Although the modeling results indicate a fairly small parameter space that should produce high efficiency, some uncertainty in the model demands that a range of parameters be explored experimentally. The diffusion model in [56] was developed based on APE structures, where devices with very low proton concentrations (as are present near the surface of the RPE guides) were not studied. Furthermore, the Sellmeier expression for the protonated material did not include any measurements in the communications band (at 1550 nm). Hence there is some error in the calculation of the effective indices used to determine the quasi-phasematching periods needed for efficient mixing. More accurate models for both the diffusion and dispersion are currently being developed [68], which should facilitate the design process.

The length of the first fabricated sample was 3.3 cm, which is short enough to allow uniform reverse exchange without any stirring. A variety of quasi-phasematching

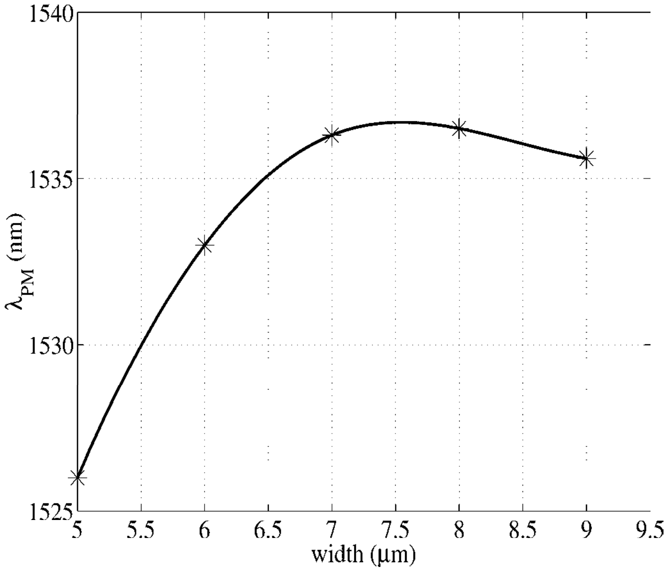

Figure 3.12: Measured phasematching wavelength vs waveguide width, showing non-critical point between 7 and 8 μm. The line is shown only to guide the eye.

periods and waveguide widths were implemented, to maximize the chance of observing phasematching in the 1550 nm band. Figure 3.12 shows a plot of measured phasematching wavelength as a function of waveguide width. A non-critical point is observed at a width in between 7 and 8 μm, close to the predicted value of 8.25 μm. The phasematching wavelengths are quite different from the calculation in Figure 3.11. The discrepancy is largely due to inaccuracies in the dispersion model. A low-power CW SHG tuning curve for a 7-μm-wide waveguide is shown in Figure 3.13, where the peak value of η_{nor}=150 %/W-cm^2 is more than three times that of the best APE result (38 %/W-cm^2, presented in Section 3.3.1). The measured SHG efficiency in the RPE waveguide is also consistent with a calculation based on the model discussed in Section 3.4.3 when complete recovery of the initially exchanged layer is assumed, supporting the observations in [61]. The shape of the measured data fits well to the calculated sinc^2 function, indicating both good process uniformity and non-critical phasematching.

Figure 3.14 shows an image of the spatial mode at 1536.5 nm of a 7-μm-wide

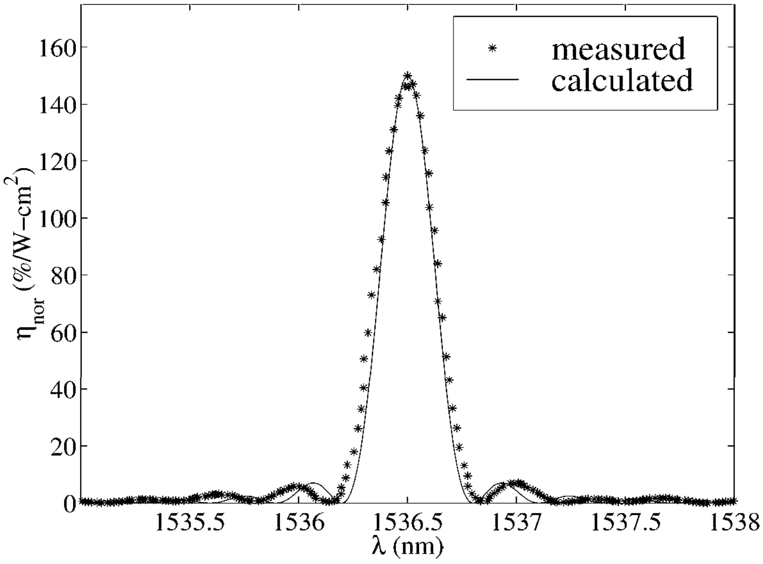

Figure 3.13: Low-power CW SHG tuning curve for optimized RPE device.

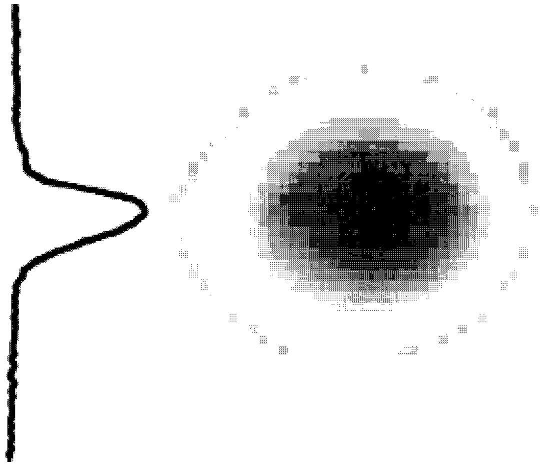

Figure 3.14: Spatial mode profile and depth cross-section for RPE waveguide.

buried waveguide. A slice in the vertical (depth) direction is also shown, where the ratio of the $1/e^2$ half widths is nearly 1:1, which is much better than that of typical APE waveguides (2.8:1) in which the asymmetric diffusion results in a long tail in depth.

3.4.6 Extrapolated Efficiency

A 6-cm-long waveguide with this value of η_{nor} would have an efficiency of $\eta = \eta_{nor} L^2 =$ 5400 %/W. It is instructive to examine the wavelength conversion efficiency and parametric gain that can be obtained through near-degenerate difference frequency generation (DFG) in such a device. With a pump input in the 775 nm band (a configuration presented in [57]), wavelength conversion within the 1550 nm band with 0 dB conversion loss can be obtained with only 30 mW local oscillator power. This calculation assumes typical propagation losses of 0.3 dB/cm at 1550 nm and 0.6 dB/cm at 775 nm. Signal parametric gain of 10 dB would be obtained with a pump power of 115 mW. In a cascaded configuration, SHG of an input local oscillator at 1550 nm generates the pump at 775 nm. This pump simultaneously mixes with an input signal through DFG to create the wavelength converted output [13]. In this configuration, 0 dB conversion loss and 10 dB parametric gain require 75 mW and 192 mW input local oscillator power at 1550 nm, respectively. An experiment of this kind with an efficient RPE waveguide device is presented in Chapter 5.

3.5 Conclusion

The process optimizations described in this chapter have resulted in the development of the most highly efficient optical frequency mixers reported to date. These devices can be used for a variety of applications. The following chapters describe experiments where this efficiency and uniformity of phasematching are exploited to observe several interesting mixing phenomena.

Chapter 4

Observation of 99 % Pump Depletion in Single Pass Second Harmonic Generation

The simplest three-wave mixing interaction is second harmonic generation. Nevertheless, it is one of the most useful and commonly exploited nonlinear optical processes, allowing extension of many readily accessible laser sources to shorter wavelengths (that are generally more difficult to produce directly). Successful commercial applications of SHG include frequency-doubled diode-pumped solid state lasers for pumping $Ti : Al_2O_3$ lasers [5] and blue light generation for use in digital video disk players [6].

As described in Section 2.4, when the second harmonic wave builds from zero in a quasi-phasematched interaction, it is free to take on any phase with respect to the fundamental. A value of $\pi/2$ results in strong, unidirectional power flow from the fundamental to the second harmonic, with the conversion efficiency asymptotically approaching unity with increasing interaction length. Deviation from this quasi-phasematched condition results in conversion of power back to the fundamental frequency. As the level of pump depletion rises, the amount of phase shift required to produce a change in direction of power flow drops rapidly. Hence achieving strong pump depletion becomes increasingly difficult as the maximum depletion approaches unity. This chapter describes the experimental observation of pump depletion up to 99 % in a quasi-CW single-pass SHG configuration. Devices operating with this level of depletion can be used for many applications, including high gain parametric amplification and generation of light with sub-Poissonian noise statistics (amplitude squeezed light) [69]. A description of SHG theory including pump depletion is first presented, followed by a discussion of the challenges involved in achieving strong pump depletion, followed by a description of the experiment and its results.

4.1 SHG Theory Including Pump Depletion

As developed in Chapter 2, the electric field profiles in a waveguide can be described by the product of an envelope function that evolves with position and a position-independent transverse profile. This profile is an eigenmode whose shape is determined by the refractive index distribution of the waveguide. The evolution of the envelopes during second harmonic generation in guided-wave structures can be described by the coupled mode equations (2.45) and (2.46), which are repeated here for convenience:

$$\frac{dA_2}{dz} = -j\sqrt{\eta_{nor}}A_1^2\exp(-j\Delta kz) - \frac{\alpha_2}{2}A_2 \tag{4.1}$$

$$\frac{dA_1}{dz} = -j\sqrt{\eta_{nor}}A_1^*A_2\exp(j\Delta kz) - \frac{\alpha_1}{2}A_1 \tag{4.2}$$

Consider the situation where the input second harmonic field is absent, and the input fundamental is given by $A_1(0) = \sqrt{P_1(0)}$. In the strong conversion limit, the right hand side of equation (4.2) cannot be set to zero. We first analyze the lossless situation ($\alpha_1 = \alpha_2 = 0$) for simplicity. If we define the nonlinear drive as:

$$\Gamma = \sqrt{\eta_{nor}P_1(0)} \tag{4.3}$$

then the solution for the dimensionless conversion efficiency $\bar{\eta}_{SHG}$ is [21, 70]:

$$\bar{\eta}_{SHG} = \frac{P_2(L)}{P_1(0)} = \upsilon_b^2\mathrm{sn}^2(\frac{\Gamma L}{\upsilon_b}, \upsilon_b^4) \tag{4.4}$$

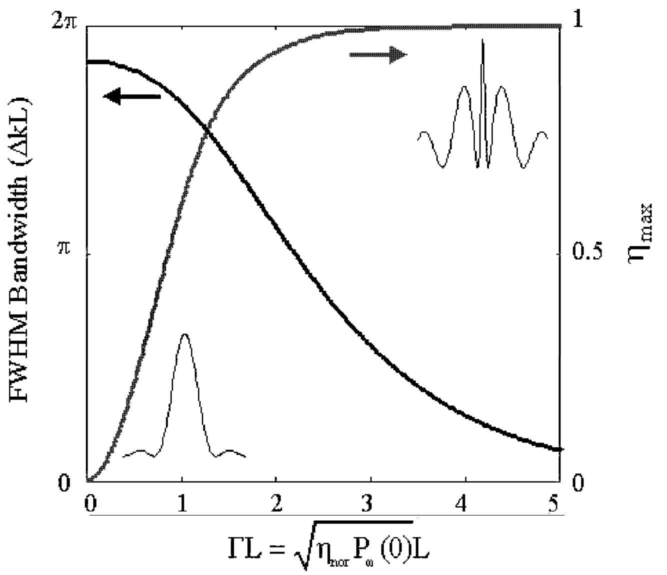

Figure 4.1: Variation of conversion efficiency and tuning curve FWHM with nonlinear drive. Tuning curve shapes are shown as insets.

where

$$v_b = \frac{1}{\Delta k/4\Gamma + \sqrt{1 + (\Delta k/4\Gamma)^2}} \tag{4.5}$$

and sn is a Jacobi elliptic function, which is implicitly defined by:

$$u(m) = \int_0^{\phi} \frac{d\theta}{\sqrt{1 - m\sin^2(\theta)}} \tag{4.6}$$

and

$$\mathrm{sn}(u, m) = \sin(\phi) \tag{4.7}$$

Examination of this expression in several limits is instructive.

In the phasematched case ($\Delta k = 0$), the solution simplifies to:

$$\bar{\eta}_{SHG}(\Gamma L) = \tanh^2(\sqrt{\Gamma L}) \tag{4.8}$$

which asymptotically approaches unity with increasing ΓL (Figure 4.1). It is the slow approach of $\bar{\eta}_{SHG}$ to unity with increasing ΓL that leads to the difficulties associated with the very strong drive required to bring the energy conversion efficiency (or pump depletion) close to unity.

At low values of ΓL (the undepleted pump case), the tuning curve expression simplifies to that described by equation (2.50):

$$\bar{\eta}_{SHG}(\Delta kL/2) = P_1(0)\eta_{LOSSLESS}(\Delta kL/2) = P_1(0)\eta_{nor}L^2\mathrm{sinc}^2(\Delta kL/2) \qquad (4.9)$$

As the drive increases, the shape of the curve changes dramatically, as described by the Jacobi elliptic function in equation (4.4). Figure 4.1 shows that the width of the main lobe narrows rapidly with increasing nonlinear drive; when $\bar{\eta}_{SHG}$ reaches 99% (at $\Gamma L = 3$), the FWHM of the main lobe drops to about 30 % of its low power value. The tuning curves shown as insets reveal the transformation from a sinc^2 function to a Jacobi elliptic function as the drive is increased, which makes achieving a conversion efficiency close to 100 % very challenging.

4.2 Pump Depletion vs Conversion Efficiency

The presence of propagation losses in waveguides precludes analytical solution of equations (4.1) and (4.2), but leaves the essential conclusions of the above discussion unchanged. To clarify contributions of linear and nonlinear effects in analyzing experimental data, it is useful to compare the transmission at the fundamental wavelength at low and high pump powers. For a device of length L, we define the transmission at the fundamental wavelength as:

$$T_\omega = \frac{P_\omega(L)}{P_\omega(0)} \qquad (4.10)$$

such that the pump depletion becomes:

$$D[P_\omega(0)] = 1 - \frac{T_\omega}{T_\omega|_{P_\omega \approx 0}} \qquad (4.11)$$

which is readily computed by straightforward numerical integration of equations (4.1) and (4.2). For a phasematched interaction, the pump depletion asymptotically approaches unity with increasing nonlinear drive, just like the conversion efficiency in the lossless case. Hence achieving strong pump depletion in lossy systems as defined above involves the same challenges as those involved with achieving strong conversion efficiency in lossless systems. These challenges are further outlined in the next section.

4.3 Experimental Challenges

4.3.1 Bulk vs Waveguide Interactions

Achieving pump depletion or energy conversion greater than 90% in single-pass bulk nonlinear optical interactions is difficult [71, 72]. The typically Gaussian transverse dependence of beam intensity results in non-uniform nonlinear drive, which (together with the attendant narrowing of the acceptance bandwidths) limits the overall conversion efficiency. Gain-induced diffraction is a particular manifestation of this phenomenon (Figure 4.2), where the center of the beam is more strongly converted than the wings, resulting in beam distortion. As discussed in [70], for an input pulse with a Gaussian profile in space and time, when the maximum local power conversion efficiency at the peak of the pump beam in space and time is 99 %, the overall energy conversion efficiency (i.e. the local instantaneous efficiency averaged over time and radial coordinate) is only 75 %. In order to increase this value to 99 % in a device of a fixed length, the peak power would have to be increased more than 40 times beyond this point. At these drive levels back-conversion and (in many cases) surface damage, would occur. Quadrature frequency conversion [73] is a technique that has been used to get more than 95 % energy conversion by using two crystals of different lengths to separately address the high and low intensity portions of the pump beam, generating harmonic waves that are orthogonally polarized in the two regions. This approach is somewhat complicated, and generates an output with transverse variations in the polarization state. Guided-wave interactions circumvent these problems.

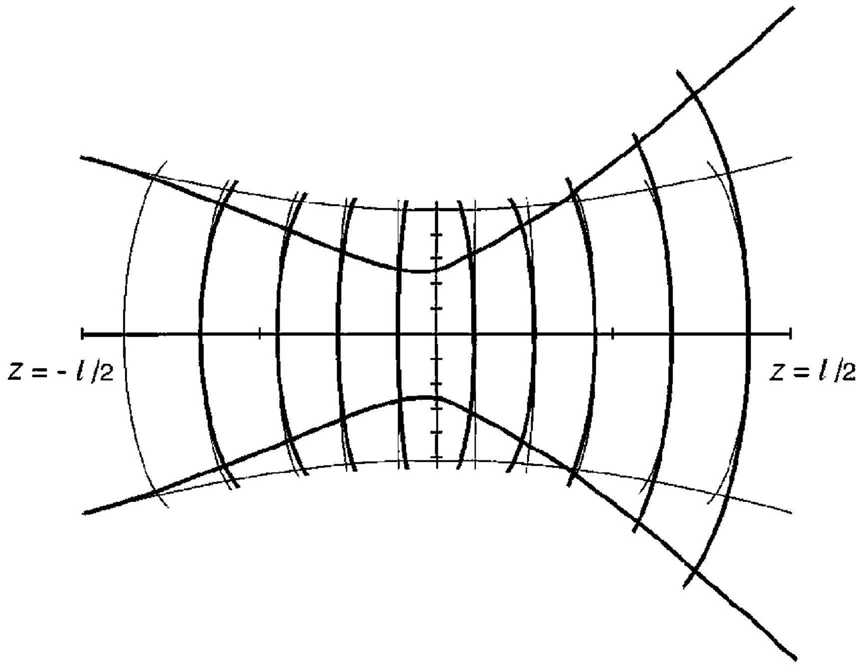

Figure 4.2: Gain induced diffraction in high efficiency bulk SHG. At low conversion efficiencies, the beam is loosely focused and the phase fronts are symmetric on either side of the focus (thin lines). At high efficiency, the central part of the beam sees much stronger conversion than the wings, such that it is focused to a tighter spot (thick lines), resulting in faster diffraction after the focus. The beam then becomes distorted, as illustrated by the curved phase fronts. Figure is adapted from [1].

Transverse variations in the mixing efficiency and diffraction effects are eliminated since the waveguide modes interact as entities. Normalized conversion efficiencies are also much higher than in the bulk case. The two-dimensional spatial confinement provided by the waveguide eliminates the tradeoff between confinement and efficiency. This additional degree of freedom reduces the power required to reach strong pump depletion, thereby opening up the choice of pump lasers to include quasi-CW and even CW sources.

4.3.2 Power Considerations

Examination of Figure 4.1 reveals that $\bar{\eta}_{SHG} = 0.99$ when $\Gamma L = 3$. For typical device parameters available at the time this work was done ($\eta_{nor} L^2 \approx 1400$ %/W), the input power required to reach this point is $P_1(0) \approx 1$ W. Pulsed sources with this level of peak power in the 1550 nm wavelength band (such as mode locked fiber lasers) have been available for many years. However, very short pulse lasers are not well suited to this type of experiment, as temporal non-uniformities complicate the depletion process in the same manner that transverse spatial variations in bulk interactions result in strong conversion at the pulse center and weak conversion in the wings. A further difficulty with short pulses is the group velocity mismatch between the launched fundamental and generated second harmonic pulses. This mismatch limits the device length, and consequently the conversion efficiency, since the pulses don't overlap in time for lengths greater than a walkoff distance [74]. The group velocity mismatch parameter for typical APE waveguides in periodically-poled lithium niobate at 1550 nm is 0.37 ps/mm. Hence the maximum quasi-phasematching grating length suitable for 1 ps pulses is less than 3 mm, as compared to the 60 mm possible using standard 3 inch diameter wafers.

Although continuous wave (CW) lasers avoid the temporal issues, they pose other problems for proton-exchanged waveguide devices. As mentioned in Section 3.3, photorefraction is a phenomenon where the presence of laser light in a material causes a change in the refractive index of that material [51]. In a nonlinear optical waveguide, these index changes can cause instability of the mixing process, as variation of optical power along the device length leads to a position-dependent variation of the phasematching condition. In the proton-exchanged waveguides used in this work, the problem is particularly serious for average powers greater than a milliwatt at short ($\lambda < 1000$ nm) wavelengths when the device is operated at room temperature. Since we are operating with a pump wavelength around 1550 nm, the second harmonic wavelength is around 775 nm, where the generated power is on the order of tens of milliwatts when strong pump depletion occurs. Hence CW sources are also not well-suited for this experiment at room temperature.

4.3.3 Parasitic Processes

Parasitic processes pose another limit to the observable pump depletion in the large conversion regime. The coupled mode equations describing near-degenerate phase-matched parametric amplification of signal and idler fields close to the fundamental frequency (pumped by the second harmonic of the fundamental input) in a lossless waveguide are:

$$\frac{dA_s}{dz} = j\sqrt{\eta_{nor}}A_{2\omega}A_i^* \tag{4.12}$$

$$\frac{dA_i}{dz} = j\sqrt{\eta_{nor}}A_{2\omega}A_s^* \tag{4.13}$$

where $\omega_s + \omega_i = 2\omega$, $A_{2\omega}$ is the second harmonic field, and we take $\Delta k = k_{2\omega} - k_s - k_i = 0$. Using equation (4.8) for evolution of the second harmonic, the solution for the parametric gain in the limit where $A_{2\omega}$ is undepleted is:

$$\mathrm{G} = |\frac{A_i(L)}{A_s(0)}|^2 = \frac{\bar{\eta}_{SHG}^2}{4(1-\bar{\eta}_{SHG})} \tag{4.14}$$

When $\bar{\eta}_{SHG} = 0.99$, G=14 dB, so small amounts of amplified spontaneous emission (ASE) at the device input (as might be present, for example, from an amplified CW pump laser) can be parametrically amplified, converting power back to the pump wavelength band, limiting the observable level of pump depletion. At this level of parametric gain, feedback from facet reflections must also be suppressed to avoid parametric oscillation, as the 14 % Fresnel reflection characteristic of a 90° facet in a

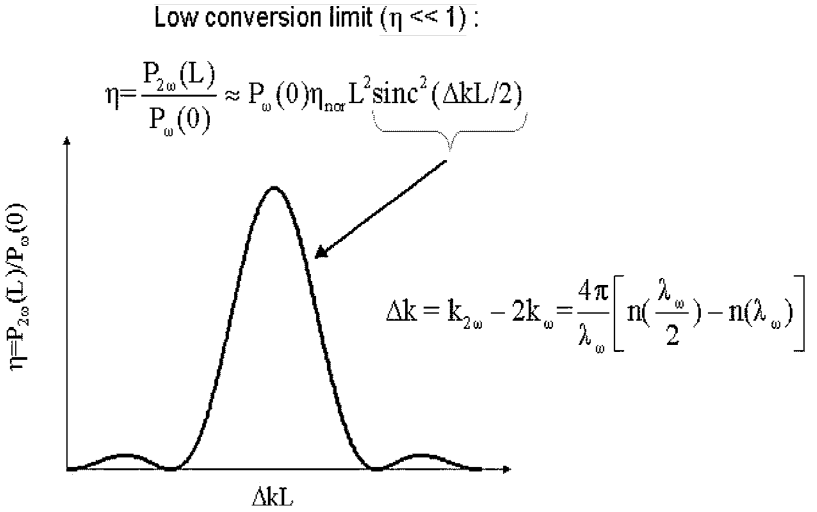

Figure 4.3: Shape of tuning curve in the undepleted pump limit.

PPLN waveguide is sufficient to reach oscillation threshold [73]. These problems can be largely mitigated by narrowband filtering of the pump source and angle polishing of the end faces, respectively.

4.3.4 Narrow Tuning Bandwidths - Tight Fabrication Tolerances

One difficulty in the large depletion regime that is not easily avoided is the narrowing of the phasematching bandwidth. As discussed in Section 2.4.1, the wavelength tuning curve is a very convenient measure of device quality. The sinc^2 shape of the tuning curve at low conversion efficiency is shown in Figure 4.3, where it is clear that there is a finite range of values of the phase mismatch ΔkL that allow for efficient mixing. This parameter is a function of any variable that affects the effective indices of the interacting waveguide modes. A useful figure of merit is the full width at half maximum (FWHM) of this function.

As the conversion efficiency increases, the shape of the tuning curve changes from a sinc^2 into the Jacobi elliptic function described by equation (4.4), where the FWHM decreases dramatically. This narrowing is illustrated in Figure 4.1, where the abscissa

Table 4.1: Comparison of FWHM of Tuning Curves at Low and High Pump Depletion

Parameter	FWHM @ η_{max}=10 % (K)	FWHM @ η_{max}=99 % (K)
annealing temperature (601 K)	± 0.0018	± 0.0005
exchange temperature (433 K)	± 0.0100	± 0.0030

is the dimensionless nonlinear drive ΓL. It is instructive to calculate the tolerances on various physical parameters that correspond to the FWHM in phase mismatch. For a 60 mm long APE waveguide in PPLN operating near 1550 nm, the change in acceptance bandwidth between 10 % and 99 % pump depletion corresponds to a drop from 0.17 nm to 0.052 nm in wavelength bandwidth. Table 4.1 shows the corresponding requirements on axial homogeneity in the proton-exchange and annealing processes, assuming linear gradients in temperature.

4.4 Experimental Setup - Quasi-CW Source

In order to fully explore the regime of large pump depletion in typical optical frequency mixers formed using APE in PPLN, CW or quasi-CW power of more than 1 Watt in the 1550 nm wavelength band is needed. Sources of this kind were not available at the time this experiment was planned, so one was designed and built specifically for this purpose. A block diagram of this amplified, externally modulated, external cavity diode laser system is shown in Figure 4.4. This pulsed system uses a cascade of erbium doped fiber amplifiers (EDFAs) to produce relatively long (5-100 ns) pulses with peak powers on the order of 5 W. The first EDFA (Lucent 1713HHA, donated by Bell Laboratories) in the chain serves as a pre-amplifier to compensate for the insertion losses of the electro-optic modulators. Pulses are produced by launching the amplified laser signal into an electro-optic amplitude modulator (EO-AM), which is driven by a low-voltage pulser. The EO-AM is a Uniphase DZ150 series device, donated by Uniphase Corporation (now JDS Uniphase).

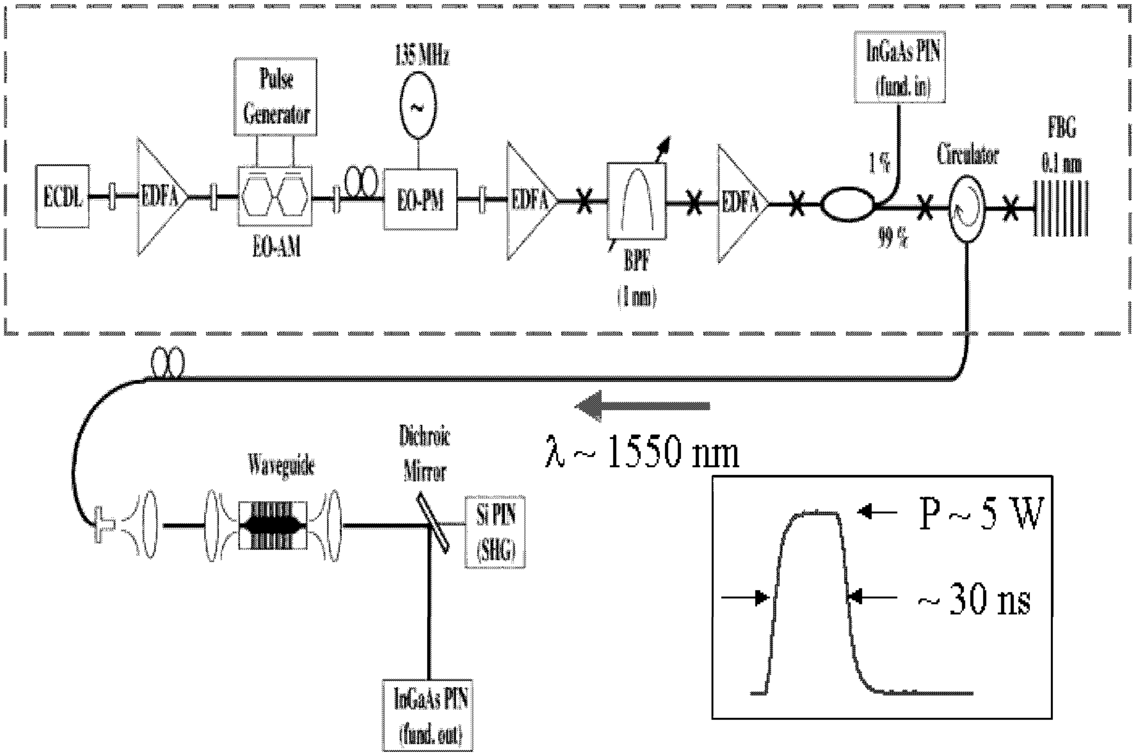

Figure 4.4: Experimental setup for pump depletion experiment. An external cavity diode laser (ECDL) amplified by a chain of erbium doped fiber amplifiers (EDFAs) produces quasi-CW pulses that are launched into the waveguide. Photodiodes are used to measure the power at the interacting wavelengths.

4.4.1 Mitigation of Stimulated Brillouin Scattering

Since we are generating peak powers on the order of Watts in a tightly confining erbium fiber, nonlinear effects in the fiber need to be considered and mitigated. Chief among these is stimulated Brillouin scattering (SBS) [75], which is a nonlinear phenomenon where photons in an intense beam propagating in a medium interact with acoustic phonons to produce a secondary optical beam propagating in the direction opposite to the incident wave. This conversion limits the power in the forward going beam once threshold is reached, as a strong diffraction grating is established, such that increasing the forward going power only increases the strength of the diffraction grating, further raising the amount of reflected light. In standard single mode optical fiber (made of silica), the SBS threshold power is on the order of 1 W. In an erbium-doped silica fiber, the threshold is greatly reduced, both by the smaller fiber core diameter and by the optical gain provided by the erbium dopant. Since it is a coherent wave mixing interaction, SBS also has a characteristic linewidth. At a wavelength of 1550 nm in silica, this number is on the order of $\Delta\nu_B \approx$10 MHz for a CW pump. For short pulses, whose bandwidth exceeds that of the Brillouin gain, the threshold for SBS is increased, so that higher peak powers can be generated than with CW radiation. A second way to increase the threshold power is to directly broaden the spectrum of the propagating signal so that it is wider than the SBS linewidth. This broadening can be accomplished by direct phase modulation, which spreads power from the main signal into sidebands separated from the carrier frequency by multiples of the modulation frequency. This technique is useful so long as the device under test has an acceptance bandwidth larger than that of the broadened signal. As discussed above, the device under consideration here has a linewidth of 0.052 nm ($\equiv$ 6500 MHz @ 1550 nm) at 99 % pump depletion, so a broadening of 135 MHz is sufficient to increase the SBS threshold to well above the powers needed for this experiment while keeping the signal within the device linewidth. This broadening is performed by an electro-optic phase modulator (JDS Uniphase PM150 series) driven by a function generator.

4.4.2 Power Amplifier Section

The last two EDFAs in the system serve to amplify the pulses to powers needed for observation of strong depletion. Both of these amplifiers were built in-house, and use laser diodes at 1480 nm to pump spools of erbium-doped silica fiber, each roughly 30 m long. Wavelength division multiplexing (WDM) couplers combine the pump light with the input signal before launching into the gain medium. Input and output isolators prevent back reflections and oscillation. The amplifier output power can be controlled by adjusting the current driving the pump diode. Both amplifiers have maximum small signal gains of roughly 25 dB with maximum saturated output powers on the order of 30 mW. When the signal pulse is absent, the pump radiation in the amplifiers produces an inverted population in the erbium-doped fiber, which results in a steady state level of amplified spontaneous emission (ASE) traveling in both directions. The arrival of the short pulse stimulates emission of much of the stored energy, resulting in a peak output power much higher than that possible with a CW signal. The idea is to force the fiber to deliver as much of its stored energy as possible during the short pulse. The tunable filter (with a FWHM transmission bandwidth of 1 nm) in between the amplifiers is designed to prevent the ASE from the first EDFA from saturating the second when the signal is absent. When the EO-AM allows the signal to pass, it travels through the filter, seeding the second EDFA so that it operates in the highly saturated regime. The peak power of the final pulses is varied by changing the current driving the pump diode of the second amplifier.

4.4.3 Narrowband Filtering

As discussed in Section 4.3.3, strong pump depletion is accompanied by significant parametric gain provided by the generated second harmonic. This parametric gain can amplify small noise inputs to levels comparable to the undepleted pump, limiting the observable level of depletion. The EDFAs in the quasi-CW source produce significant amounts of ASE that can seed this process. While the tunable filter with 1 nm FWHM bandwidth is sufficient to prevent gain saturation of the second amplifier by ASE from the first, further filtering is needed after the second stage to limit the

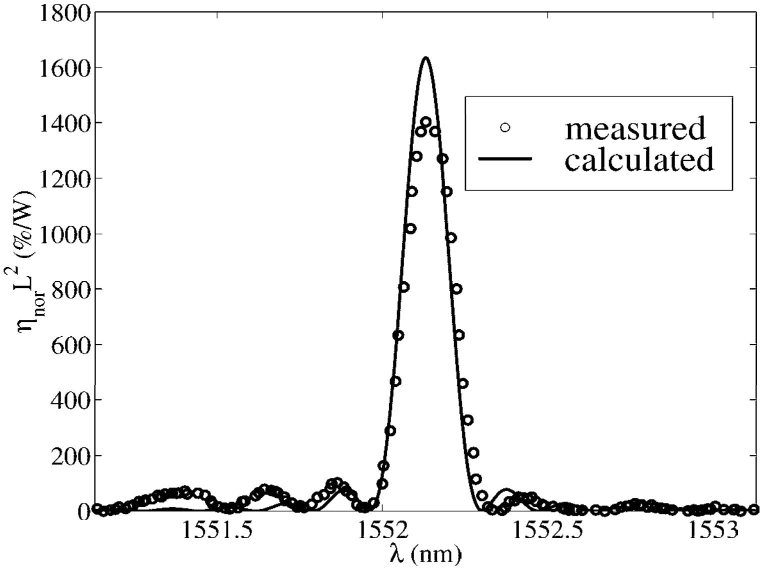

Figure 4.5: Low-power, CW SHG tuning curve for optimized APE waveguide used in pump depletion experiment.

amount of ASE entering the waveguide. The circulator and narrowband fiber Bragg grating (FBG) serve this purpose. The reflection spectrum of the FBG (donated by Sabeus Photonics) has a FWHM of 0.1 nm, where its center wavelength is tunable by mechanically stretching the fiber in between two translation stages. The optical circulator serves to collect only the filtered signal reflected from the FBG and pass it to the waveguide coupling stages. The rejected power transmitted by the FBG is discarded by placing the other end of the fiber in a container of index-matching gel. The filtered pulses are reasonably square in time, with 30 ns pulsewidth at 1 kHz repetition rate. The maximum generated power is roughly 5 W.

4.5 Pump Depletion Results

The optimization of the APE waveguide discussed in 3.3.1 was used to design and fabricate a waveguide with a peak efficiency of $\eta_{nor}L^2$=1400 %/W. The low-power CW SHG tuning curve for that device is shown again in Figure 4.5 for reference.

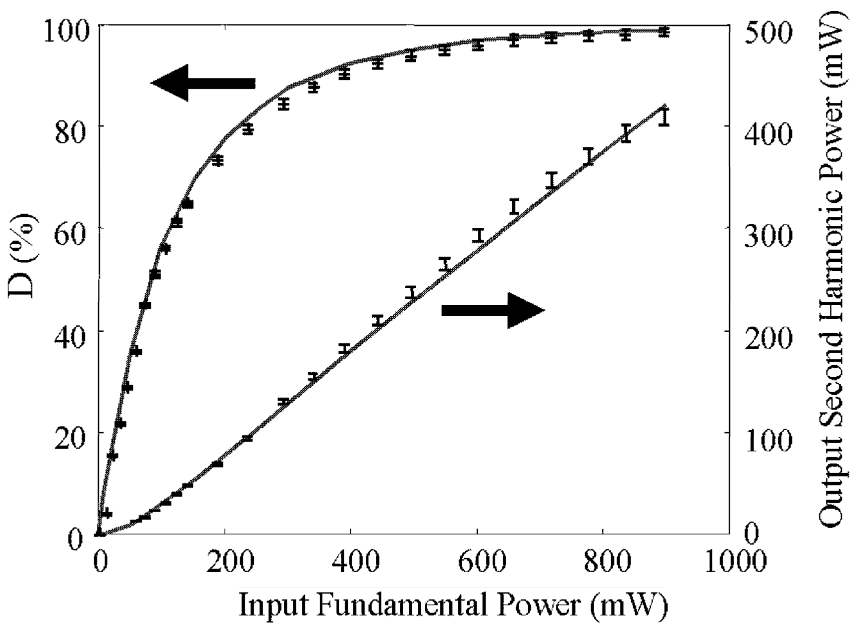

Figure 4.6: Pump depletion and second harmonic generation power as functions of input pump power. The data fit well with the calculation, with pump depletion reaching 99 % with 900 mW input.

The superimposed calculation used typical values of power propagation losses 2α at the fundamental and SH wavelengths (0.43 and 0.59 dB/cm respectively). The peak efficiency of the calculated curve is chosen such that the areas under the measured and calculated curves are equal, which results in a value of η_{nor}=38 %/W-cm^2. The deviation of the measurement from the calculation is caused by residual phase mismatch along the length of the device, which arises from slight imperfections in the fabrication process. Figure 4.6 shows a plot of pump depletion as a function of pump power launched into the waveguide, along with a calculation using the same values of propagation losses and normalized efficiency used in the low power fit. The three signals (fundamental in, fundamental out, and second harmonic out) were measured by time-resolving the pulses detected by calibrated photodiodes on a digital oscilloscope, such that all powers are peak values. Good agreement with theory is observed, with pump depletion reaching 99 % at an input power around 900 mW. A plot of the generated power at the second harmonic wavelength is also shown, where again agreement is very good. When the input power is increased beyond this point, the curves turn around. In other words, pump depletion and the amount of generated second harmonic power start to decrease. The small residual phase mismatch apparent from the CW tuning curve may cause this phenomenon, where deviation from the phasematching condition results in back-conversion. Parametric amplification of residual ASE from the amplifiers by the strong second harmonic signal is another possibility.

4.6 Wavelength Tuning Curves in the Strongly Depleted Limit

The pump depletion results in the previous section required fixing the pump wavelength at the phasematching point while increasing the pump power. As discussed in Section 4.3.4, the shape of the SHG tuning curve as a function of pump wavelength changes dramatically from a sinc^2 at low power to a Jacobi elliptic function at large levels of pump depletion. Figure 4.7 shows the calculated evolution of the tuning curve shape as a function of maximum pump depletion. Although this behavior was predicted by Armstrong et al [21] in the seminal paper on nonlinear optics, clear experimental observation of this tuning behavior has until now been impeded by the various effects discussed in Sections 4.4.1-4.4.3.

4.6.1 Experiment and Results

This experiment was done with a buried waveguide formed using the RPE process described in Section 3.4. The low-power CW SHG tuning curve for this device is shown in Figure 4.8. The peak efficiency for this device with a grating length of 33 mm is $\eta_{nor}L^2$=1630 %/W, so that the normalized efficiency is η_{nor}=150 %/W-cm^2.

The challenges that make this experiment difficult naturally mirror those of the pump depletion measurement described above, since we are operating in the large depletion regime in both cases. The measurement is further complicated by the need to tune the wavelength while maintaining a constant input power level. The

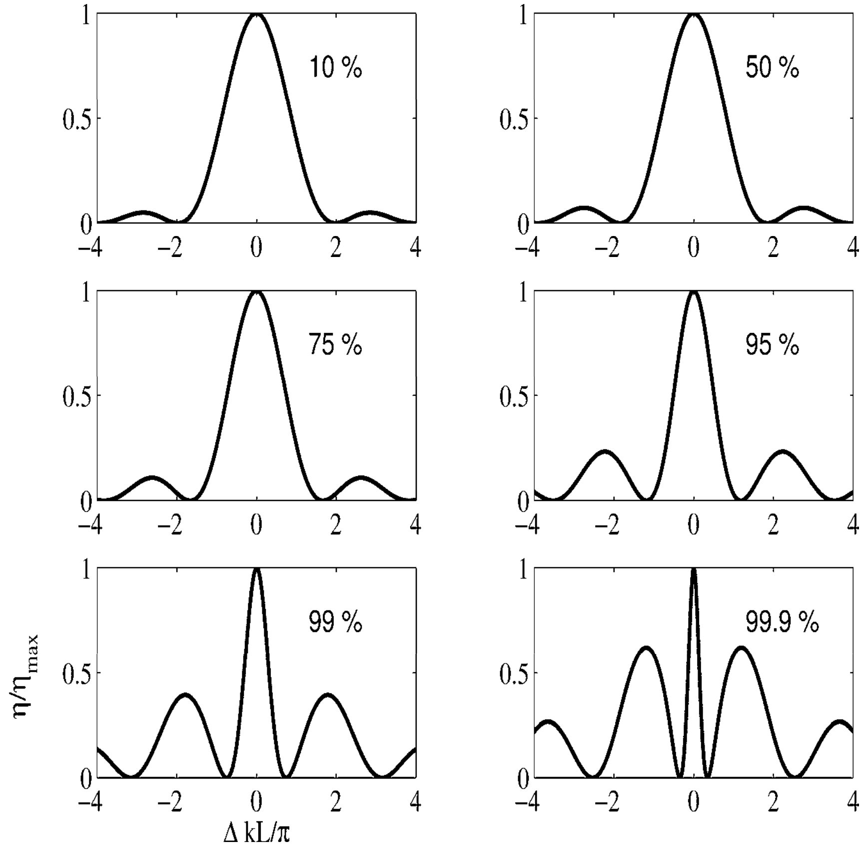

Figure 4.7: Calculations of tuning curve shapes at varying levels of maximum pump depletion. The bandwidth narrows and sidelobes rise as the maximum depletion approaches 100 %.

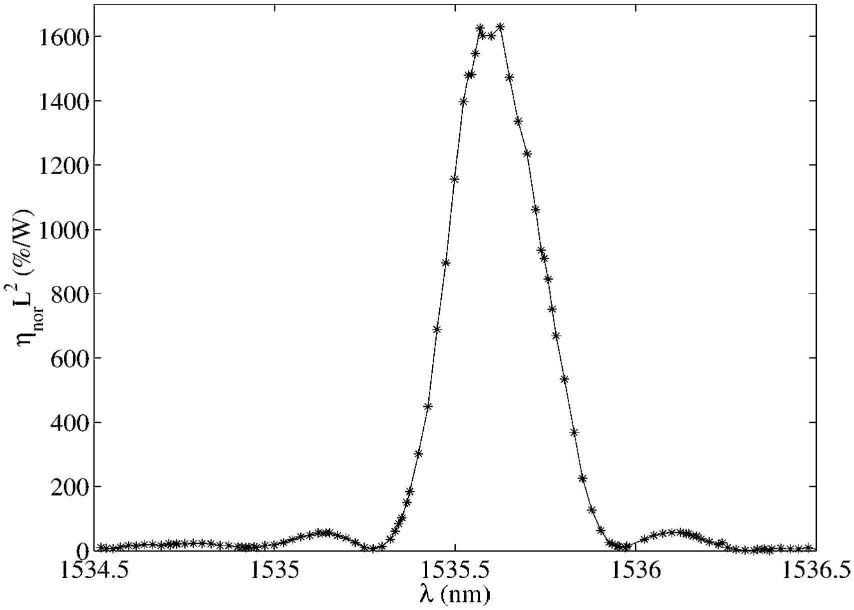

Figure 4.8: Low-power CW SHG tuning curve for waveguide used in observation of Jacobi elliptic tuning curves.

experimental setup is shown in Figure 4.9, where the original quasi-CW source was modified in order to facilitate wavelength tuning. The FBG and circulator were removed, since the tuning curves span roughly 2 nm, and the grating was not mounted in a fashion conducive to accurate, fast tuning. The pulsewidth was reduced to roughly 20 ns, which allowed for removal of the phase modulator, as the broadening provided by the shorter pulse was sufficient to prevent SBS at the powers needed to observe strong depletion in this more efficient device. In order to facilitate acquisition of tuning curve data, boxcar integrators were used to measure the power levels in the three pulses. These devices were triggered by the pulser driving the EO-AM, and produce DC voltages proportional to the peak values of the measured pulses. An interferometric wavelength meter produced a fourth voltage proportional to the laser wavelength. All four voltages were sampled using a data acquisition board in a desktop computer, then combined to produce the desired tuning curves.

The measured tuning curves for various levels of input power (and pump depletion) are shown in Figure 4.10 (normalized to unity). The maximum observable pump

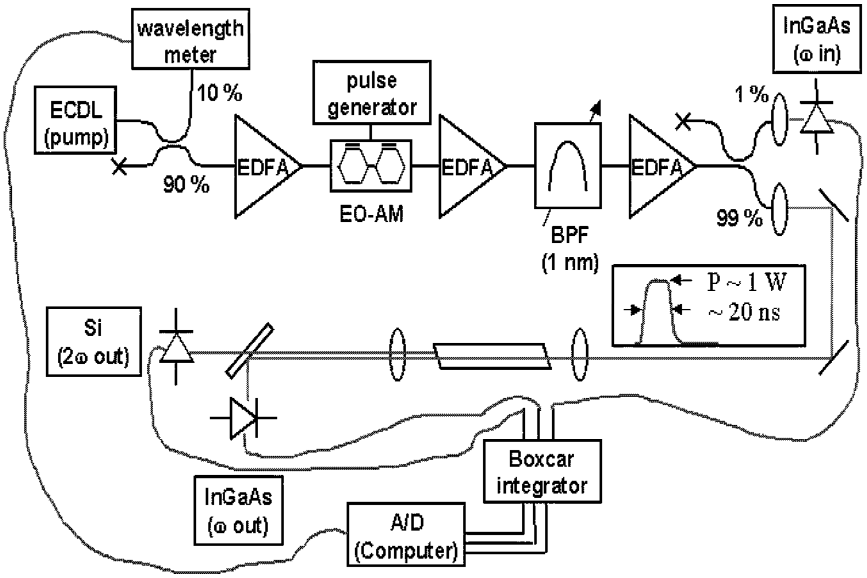

Figure 4.9: Experimental setup for measuring wavelength tuning curves in the highly depleted limit. This setup is similar to that used for the pump depletion measurement (Figure 4.4), where some elements have been removed to facilitate wavelength tuning.

depletion without back conversion was 95 % at a peak input power of 732 mW. The first curve (top left) is identical to that in Figure 4.8. As the peak depletion increases, the evolution of the shape from a sinc^2 function to a highly distorted Jacobi elliptic function is evident, and good agreement with the calculated profiles is observed. Figure 4.11 shows a tuning curve taken at a much higher power in another (similar) waveguide, where strong distortion is observed and the shape cannot be fit using simple theory. This distortion is a result of driving the peak conversion beyond the limit allowed by the waveguide imperfections, where small amounts of back-converted radiation can alter the phase of the total fundamental field.

4.7 Conclusion

Obtaining complete pump depletion in second harmonic generation presents many experimental challenges. The experiments described in this chapter involve the first observation of nearly complete pump depletion, along with the associated modification

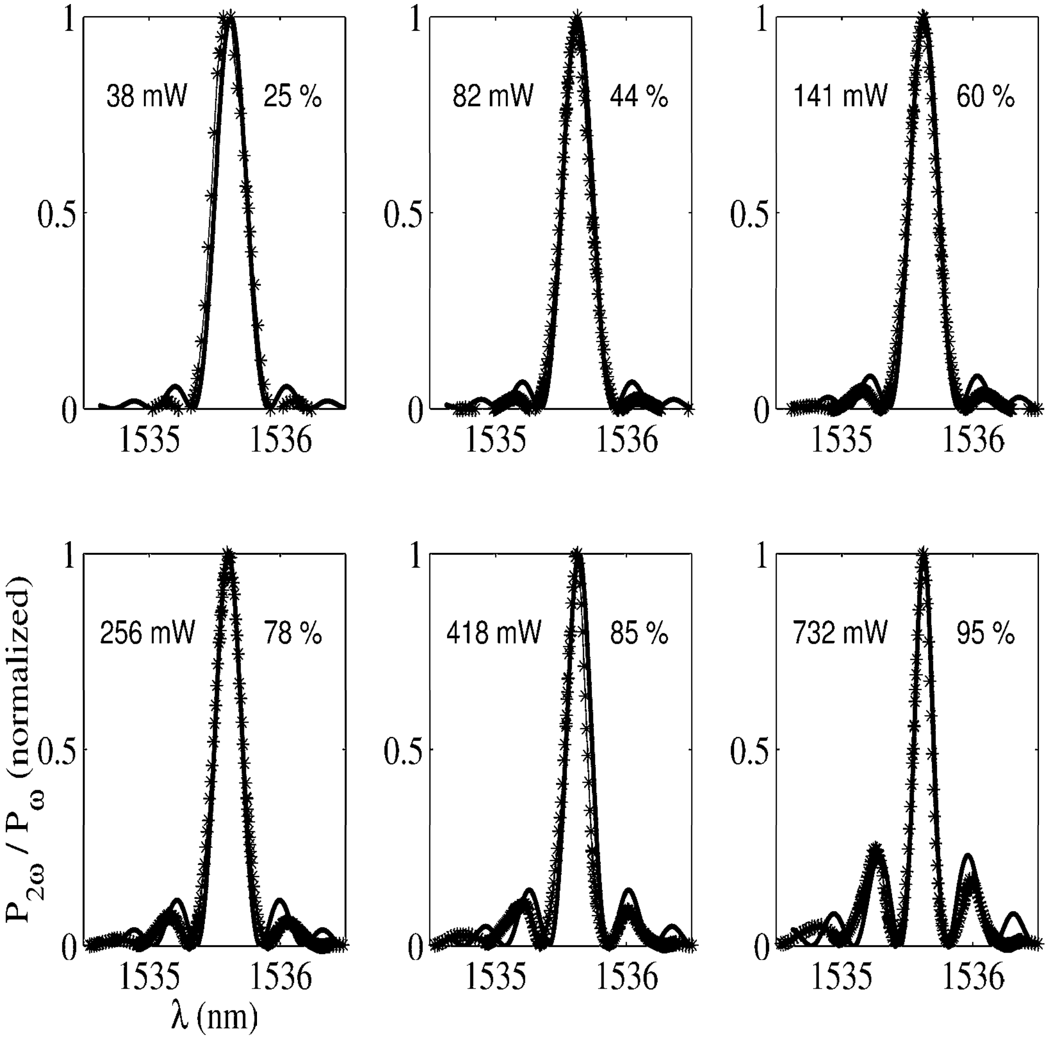

Figure 4.10: Normalized SHG tuning curves for various levels of pump depletion. Good agreement is observed between measurement and calculation. The peak input power is shown to the left of each curve.

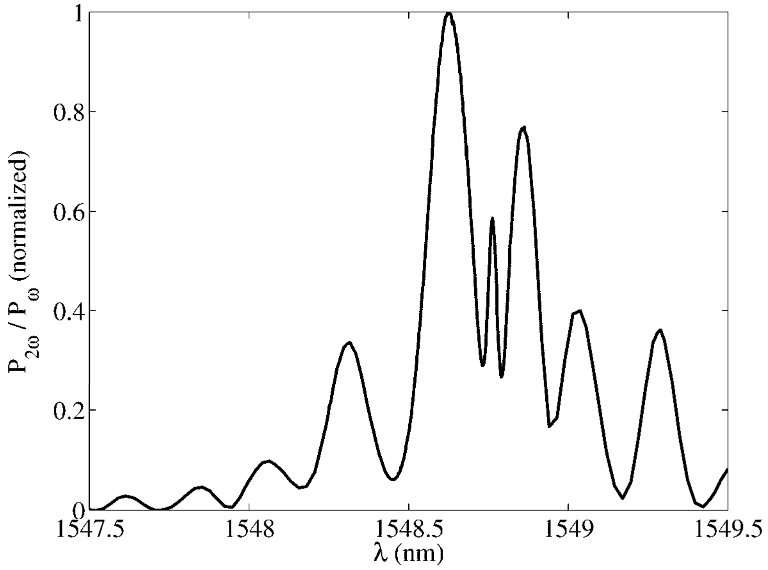

Figure 4.11: Tuning curve taken in the regime where back-conversion (in the form of parametric amplification of ASE) is taking place. Very strong distortion is observed, where simple theory can no longer predict the shape.

of tuning behavior, in a single-pass waveguide SHG experiment. The high efficiency and uniformity of phasematching in the optimized waveguides discussed in Chapter 3 allow for the observation of these unprecedented levels of depletion. Application of these mixers to telecommunications functions is presented in Chapter 5.

Chapter 5

Telecommunications Experiments

Second harmonic generation is a very useful function for generating wavelengths that are otherwise difficult to obtain. In the telecommunications band, SHG serves as a very useful diagnostic for characterizing devices designed for use in near-degenerate three-wave mixing interactions such as sum and difference frequency generation (SFG and DFG, respectively). These more complicated processes can be used to implement a variety of telecommunications functions, such as optical gating, wavelength conversion, and parametric amplification. This chapter describes the use of optical frequency mixers in demonstrating these functions.

5.1 Optical Gating using Sum Frequency Mixing

A basic element from which logic circuits are built is the simple two-input gate, where one input carries some information, and the other controls the first. The strong nonlinearities available from transistors and diodes have made it very easy to make efficient, cascadable electronic logic gates. The relatively weak nonlinearities at optical frequencies make implementation of all-optical gates quite challenging. Many implementations have been investigated in recent years. Four-wave mixing in optical fibers, for example, has been demonstrated by many groups [76], [77]. The weak third order nonlinearity $\chi^{(3)}$ used in this process requires either high switching powers or long interaction lengths in order to achieve complete switching in these

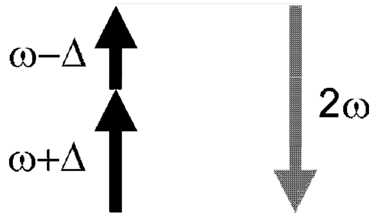

Figure 5.1: Energy level diagram describing sum frequency generation interaction.

devices. Semiconductor optical amplifiers have also been used in numerous switch configurations [78]. One difficulty with these devices is limited switching speed due to finite carrier lifetimes. Cascading of second-order nonlinearities ($\chi^{(2)} : \chi^{(2)}$) is another approach [79], [80]. The switching power needed in these configurations is quite high (on the order of several Watts), primarily because they operate far from phasematching in order to simultaneously obtain a large phase shift (required for switching) and flat spectral response.

In this section, an all-optical gate based on sum frequency generation (SFG) using a single phasematched $\chi^{(2)}$ interaction in an APE waveguide formed in PPLN is presented. This approach exploits the high conversion efficiency available from operation at the phasematching point, while the instantaneous nature of the parametric process results allows for high-speed operation. A loop mirror structure using this gate is proposed with which high contrast, low power, all-optical switching can be performed.

5.1.1 Sum Frequency Generation

Second harmonic generation is essentially a two-wave interaction, where energy is converted from a single input wave to a single output. In most signal processing functions, at least two inputs are needed, where one (control or local oscillator) determines the transmission of the other (signal). In a sum frequency generation interaction, two low energy photons combine to produce a single higher energy photon (Figure 5.1). As the power of either input wave is increased, the sum frequency wave grows and the transmission of the input waves decreases. If one of the waves is much stronger than the other and remains relatively undepleted, as its power is increased, the transmission of the weaker signal decreases. Hence at some control power, all of the signal power is transferred to the sum frequency wave.

To illustrate this behavior, the coupled mode equations (2.37)-(2.39) can be solved subject to the following boundary conditions: $A_1(0) = \sqrt{P_{SIG}}$, $A_2(0) = \sqrt{P_{CTRL}}$, $A_3(0) = 0$. The equations are repeated here for convenience:

$$\frac{dA_3}{dz} = -j\kappa_3 \nu A_1 A_2 \exp(j\Delta k z) - \frac{\alpha_3}{2} A_3 \tag{5.1}$$

$$\frac{dA_2}{dz} = -j\kappa_2 \nu^* A_1^* A_3 \exp(-j\Delta k z) - \frac{\alpha_2}{2} A_2 \tag{5.2}$$

$$\frac{dA_1}{dz} = -j\kappa_1 \nu^* A_2^* A_3 \exp(-j\Delta k z) - \frac{\alpha_1}{2} A_1 \tag{5.3}$$

where

$$\kappa_i = \sqrt{\frac{8\pi^2 d_{eff}^2}{n_1 n_2 n_3 c \epsilon_0 \lambda_i^2}} \tag{5.4}$$

The solutions in the lossless ($\alpha_i = 0$), phasematched ($\Delta k = 0$) case are:

$$P_{SFG}(L) = P_{SIG}(0) \frac{\lambda_{SIG}}{\lambda_{SFG}} \sin^2(\sqrt{\eta_{nor} P_{CTRL}} L) \tag{5.5}$$

$$P_{SIG}(L) = P_{SIG}(0) \cos^2(\sqrt{\eta_{nor} P_{CTRL}} L) \tag{5.6}$$

As illustrated in Figure 5.2, when the control power is increased from zero, the signal gets depleted and power gets transferred to the SFG wave. Near degeneracy (where the signal and SFG wavelengths are similar), the wavelength ratio in equation (5.5) is roughly 2, such that when the signal is completely depleted, the peak power of the SFG wave is twice that of the input signal. Power is still conserved, as the difference in power between the input signal and generated SFG wave comes from the control wave. As the control is increased beyond this point, the SFG wave mixes with the control through difference frequency generation (DFG) to regenerate the signal. Hence switching the control power between zero and P_{SW} results in gating of the signal, where P_{SW} is determined by the value that makes the argument of the

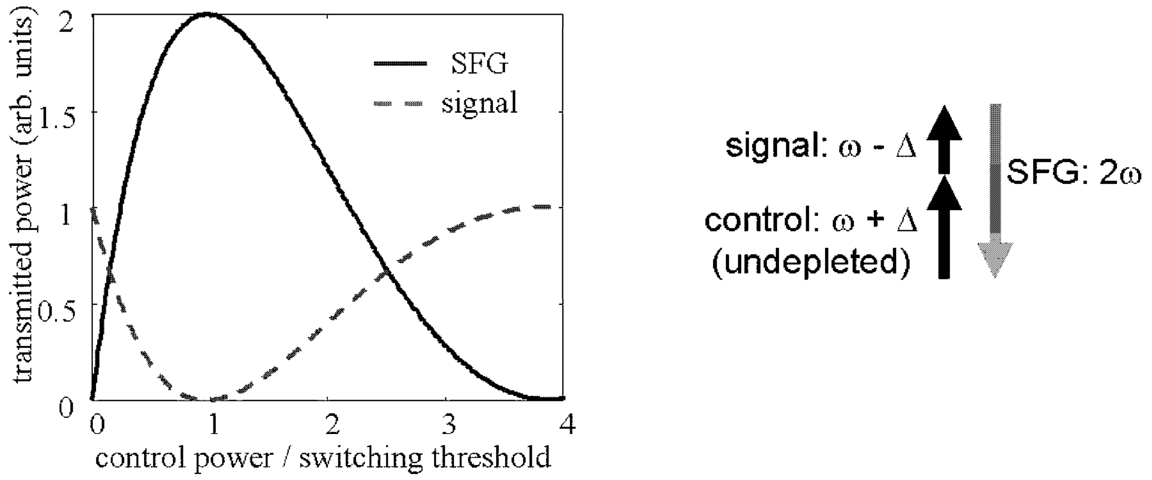

Figure 5.2: Calculation of signal and sum frequency transmission as functions of control power in an SFG interaction.

trigonometric functions in equations (5.5)-(5.6) equal to $\pi/2$:

$$P_{SW} = \frac{\pi^2}{4\eta_{nor}L^2} \tag{5.7}$$

It should be noted that complete switching is achieved without depletion of the control wave, so that the bandwidth narrowing that takes place in the large conversion regime of SHG is not present here. When switching is done near degeneracy, both the signal and control wavelengths are similar, such that both have tuning bandwidths that are similar to that of the pump in an SHG interaction. A typical value for this bandwidth is 0.17 nm for a device having a QPM grating length of 60 mm, where the bandwidth scales inversely with grating length.

5.1.2 SFG Experiment

The waveguide used in this experiment was fabricated using the annealed proton-exchange technique discussed in Chapter 3. The dimensionally non-critical design presented in section 3.3.1 for mixing in the 1550 nm wavelength band was employed in order to loosen fabrication tolerances. The particular device used in this work was

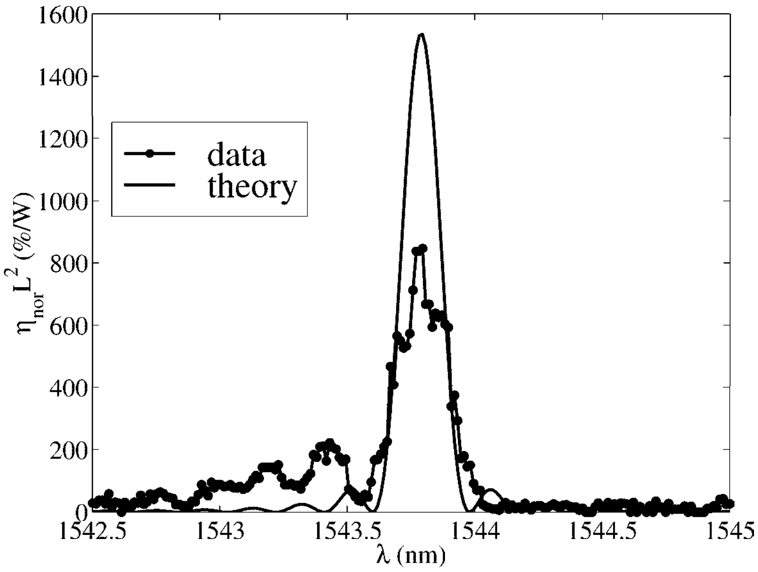

Figure 5.3: Low power CW SHG tuning curve for device used in SFG experiment.

sub-optimal, as evidenced by the tuning curve in Figure 5.3. The peak measured efficiency is 847 %/W for this sample with a QPM grating length of 5.55 cm. This efficiency is significantly lower than the value for the optimized device discussed in Section 4.5. The peak value of 1500 %/W in the calculated curve in Figure 5.3 was found by integrating the area under the measured data, as discussed in Section 2.4.1. This area is equal to the peak efficiency that would have been available from this device had the fabrication conditions been ideal. This device was fabricated before the implementation of many of the engineering optimizations described in Chapter 3, which resulted in non-uniformities during fabrication, such that the tuning curve became notably distorted. Nevertheless, the device efficiency is sufficient to prove the concept of gating using SFG.

The experimental setup is shown in Figure 5.4. Since the tuning bandwidths of both the signal and control beams in SFG are small, narrowband sources are needed in order to observe efficient mixing. Control pulses were produced by an externally modulated, fiber-amplified, external cavity diode laser. This quasi-CW source is very similar to that discussed in Section 4.4, where long ($\approx$ 50 ns) pulses having peak

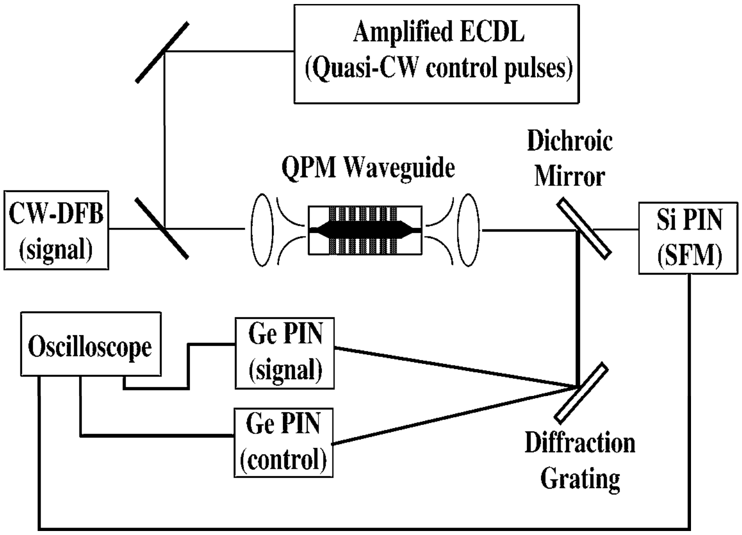

Figure 5.4: Experimental setup for optical gating using SFG.

powers on the order of 5 W are produced. A distributed feedback (DFB) laser diode operating at 1537 nm produces the CW signal. The signal and control beams are combined, then launched into the waveguide. A dichroic mirror separates the signal and control beams (both in the 1550 nm band) from the sum frequency wave (in the 775 nm band). A bulk diffraction grating allows for spatial separation of the signal and control beams. PIN photodiodes are used for measuring the temporal profiles of the pulses.

Figure 5.5 shows a set of pulse traces, illustrating depletion of the CW signal in the presence of the control pulse. When the control is off, the signal transmission is normalized unity. In the presence of the control pulse, the signal transmission drops nearly to zero. Close examination of the pulse shapes indicates that the distortion near the peak of the control pulse is somewhat suppressed in the inverted signal pulse, a result of the nonlinearity in the SFG transfer function shown in Figure 5.2. Near the switching point, the first derivatives of the signal and sum frequency transmission curves are zero, such that the transmission of these waves is (to first order) insensitive to changes in the control power about this point.

Figure 5.6 shows a plot of normalized signal transmission as a function of control

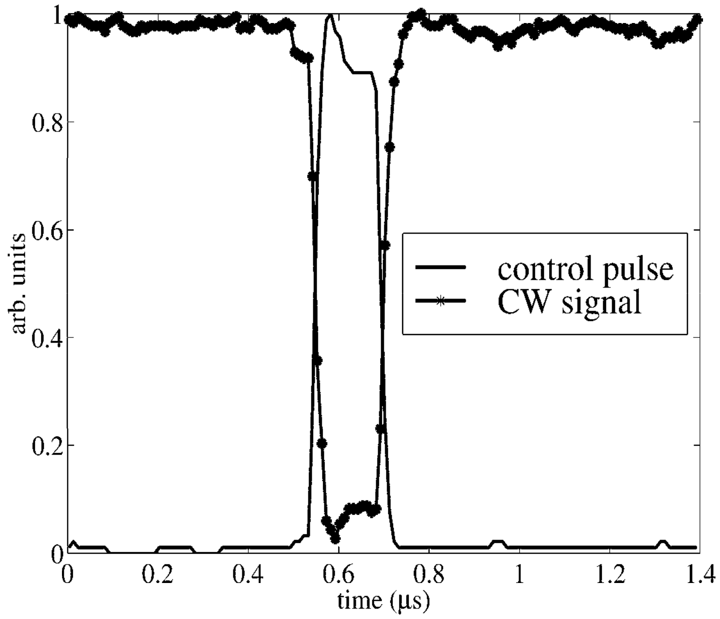

Figure 5.5: Measured pulse traces, showing depletion of the signal in the presence of the control beam.

power. The solid line shows the calculated result obtained by numerical integration of the coupled mode equations (5.1)-(5.3), including propagation losses. The calculation uses the measured normalized internal SHG conversion efficiency of $\eta_{nor}L^2 = 847$ %/W and typical values of propagation losses at the three wavelengths (0.35 dB/cm at λ_{SIG} and λ_{CTRL}, and 0.70 dB/cm at λ_{SFG}). Nearly complete (96 %) extinction of the signal is seen at an input control power of 185 mW, a value in reasonable agreement with theory. The mechanism responsible for the residual 4 % is likely the phase mismatch along the device length arising from waveguide nonuniformities due to imperfections in fabrication, as evidenced in the tuning curve of Figure 5.3. It should be noted that the threshold control power for this function scales inversely with the normalized conversion efficiency η_{nor} (equation (5.7)). Hence implementation of this function using the buried waveguides discussed in Section 3.4 will greatly reduce the required gating power. For example, an optimized buried waveguide device with $\eta_{nor} = 150$ %/W-cm^2 would have $\eta_{nor}L^2 = 5400$ %/W, which would reduce the gating power to a value below 30 mW.

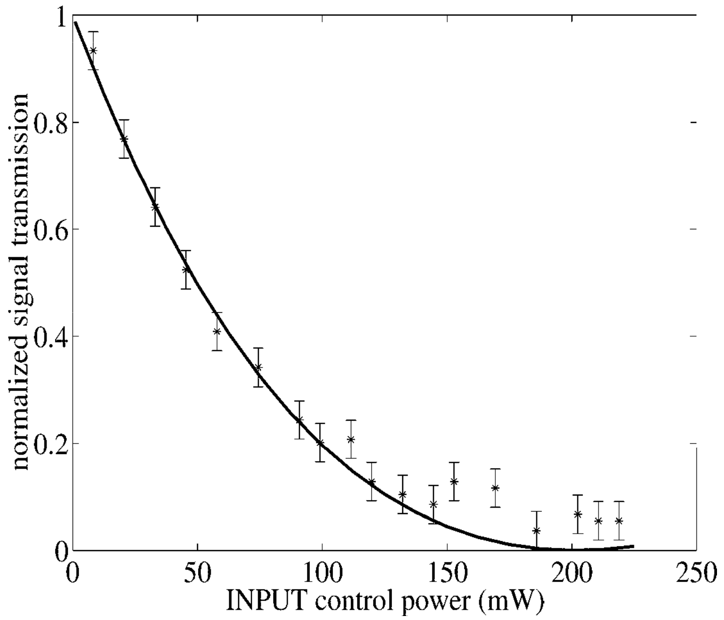

Figure 5.6: Measured and calculated variation of signal transmission with control power.

5.1.3 Loop Mirror Configuration

A very important measure of any switch is its contrast, which is the ratio between the outputs in the "on" and "off" states. Hence having a very high quality off state (where the signal is as close to zero as possible) is paramount. The experiment described in the previous section showed a residual 4 % signal transmission in the off state, due to slight imperfections in fabrication that led to deviation from phasematching along the device length. This problem can be avoided by placing the waveguide in a nonlinear optical loop mirror (NOLM, Figure 5.7). This simple structure is a Sagnac interferometer formed by connecting the outputs of a 3-dB (or 50:50) fiber splitter together with a nonlinear element in between them. Power entering port 1 is evenly divided between the two output ports of the splitter. In the absence of a control signal, the $\chi^{(2)}$ device (waveguide optical frequency mixer, for example) presents only a reciprocal passive loss, such that the two counterpropagating signals return to the splitter at the same time and interfere in phase, having traversed the same path in

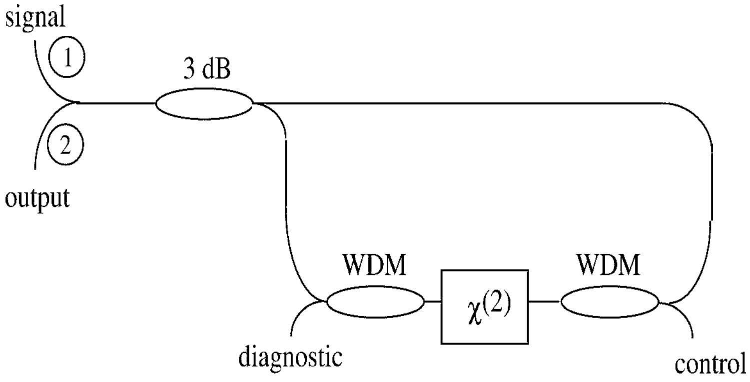

Figure 5.7: Nonlinear optical loop mirror structure using $\chi^{(2)}$ interaction.

opposite directions. This balanced state of the interferometer results in all of the input power being coupled back to port 1 (all of the power entering port 1 is reflected out the same port, hence the term "loop mirror"). If we take port 2 to be the output of the switch, this situation corresponds to the off state. The quality of this zero is determined solely by the symmetry of the 3-dB splitter. Commercially available components are symmetric to better than 0.05 dB, so this structure leads to switching with extremely good extinction.

In order to obtain a "1" state at port 2, the interferometer must be imbalanced in a controllable manner. The optical frequency mixer serves this purpose, forcing some power to be leaked out of port 2. A control wave entering the loop in a clockwise direction can mix with the signal propagating in the same direction to create the imbalance. In the case of SFG, the mixing process converts the clockwise signal to the sum frequency (as described in the previous section). This sum frequency signal can be removed from the loop using a WDM coupler and be used as a diagnostic (since it contains all of the signal information). The absence of a clockwise control wave results in the counterclockwise signal power being divided between ports 1 and 2 upon returning to the 3-dB coupler. Hence this results in a high-contrast (from the loop architecture), narrowband (due to the narrow phasematching bandwidth of the SFG process) gate with an insertion loss of roughly 9.5 dB (arising from two passes through the 3-dB coupler and a single pass through the fiber-pigtailed waveguide, whose insertion loss is typically 3.5 dB). Any residual signal resulting from imperfect phasematching in the waveguide only results in a slight increase in the insertion loss, as this residual signal interferes with the counterclockwise signal at the 3-dB coupler. The extinction of the "0" state remains unchanged.

Another three-wave mixing interaction that can be used to imbalance the loop is DFG. As will be discussed in detail in Section 5.2, this process results in amplification of the signal (rather than the depletion characteristic of SFG). A further difference is the broad signal bandwidth of DFG as opposed to the very narrow bandwidth of SFG. The loop can be imbalanced by amplifying the clockwise signal, such that interference at the 3-dB coupler can result in more power exiting port 2. For example, if the clockwise signal is amplified by an amount equal to the waveguide insertion loss, interference with the counterclockwise signal (that sees the insertion loss without amplification) results in the output power at port 2 being exactly equal to the input power at port 1. This configuration thus creates a high-contrast (inherent to the loop architecture), broadband (from the near-degenerate DFG interaction) gate with 0 dB insertion loss. Increasing the parametric gain of the clockwise interaction above that required to compensate for the insertion loss can produce a switch exhibiting net gain. In this situation, the interferometer is called a nonlinear amplifying loop mirror (NALM).

Nonlinear loop mirrors were originally proposed using optical fibers as the nonlinear element [81, 82, 83]. In this case, the imbalance is produced using $\chi^{(3)}$ effects such as cross-phase modulation or cross-gain modulation. Here, a control pulse launched unidirectionally in the fiber produces a change in the transmission properties at the signal wavelength. If timed correctly, the phase or gain modulation seen by the clockwise pulse is different from that seen by the counterclockwise pulse, resulting in incomplete interference at the 3-dB coupler. One difficulty with this approach is the inherent weakness of the $\chi^{(3)}$ nonlinearity, which requires either a very long segment of fiber or very high peak powers in order to accumulate sufficient nonlinear phase to imbalance the loop. Semiconductor optical amplifiers (SOAs) are also commonly used for the same purpose [84, 85, 86]. A complication here is that the finite carrier lifetime in SOAs can limit the size of switching windows (and thus switching speeds) in these mirror architectures. The use of optical frequency mixers as nonlinear components in loop mirrors is attractive in that the parametric mixing process is virtually instantaneous, such that the switching speed is limited only by the group velocity mismatch of the waves propagating in the crystal. Switching speed can be traded off against conversion efficiency, as shorter samples can switch shorter pulses, while the conversion efficiency increases with the square of the length. For example, in the waveguides discussed in this dissertation, the mismatch parameter is roughly 0.37 ps/mm, implying that a 60-mm-long device can switch a 25 ps pulse without distortion of the pulse shape, which is sufficient to switch individual bits in a 40 Gb/s data stream, so the efficiency-speed tradeoff is not very costly. The fact that only co-propagating signals satisfy the phasematching condition in the waveguide allows the mixer to be placed anywhere within the loop, regardless of the pulse widths, greatly simplifying the timing and implementation of the gate.

5.2 Wavelength Conversion using Cascaded SHG and DFG

A very useful function in multi-wavelength fiber communication systems is all-optical wavelength conversion. While the SFG process described in section 5.1 involves conversion of signal information from a wavelength in the 1550 nm band to one in the 775 nm band, this output wavelength is not in the communications band. Difference frequency generation (DFG) can be used to perform wavelength conversion within a single wavelength band, and is also accompanied by optical parametric amplification (OPA) of the original signal. This configuration is illustrated in Figure 5.8, where a local oscillator photon at ω_{LO} mixes with a signal photon at ω_s. The DFG process creates a photon at a new frequency of $\omega_{LO} - \omega_s$. Since the local oscillator photon is destroyed in this process, conservation of energy dictates that this new photon be accompanied by generation of a new signal photon at ω_s. Hence two functions are obtained in a single three-wave mixing interaction. A mixer device implementing this type of DFG wavelength conversion has been successfully demonstrated [57], where

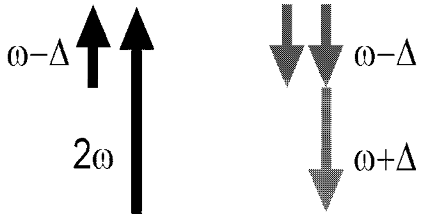

Figure 5.8: Photon picture of difference frequency generation and optical parametric amplification.

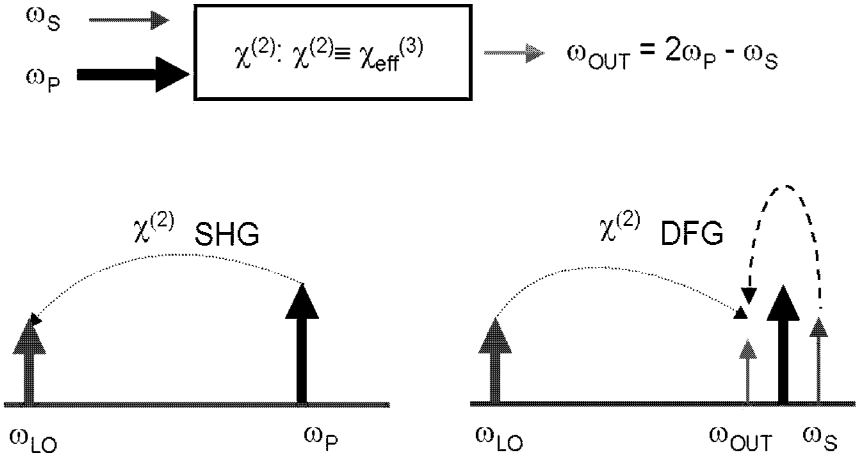

Figure 5.9: Wavelength conversion through cascaded SHG/DFG processes.

integrated coupling structures were used to combine the local oscillator and signal in the same waveguide.

One difficulty with this architecture is that the local oscillator is in the 775 nm wavelength band. Sources in this band are not commonly rated for use in telecommunications systems, so an approach where both inputs are in the 1550 nm band is highly desirable. One elegant way of doing this is to generate the local oscillator using SHG in the same device where DFG takes place. This so-called cascaded $\chi^{(2)}$ approach [87] is illustrated schematically in Figure 5.9. Here, a pump wave at frequency $\omega_P = \omega_{LO}/2$ creates the local oscillator through SHG in the mixer. The output frequency is then created through the same DFG process described above. This interaction looks very much like four-wave mixing using $\chi^{(3)}$, where the output frequency is twice one of the input frequencies minus the other. Using two second-order nonlinearities to perform the function results in a very strong effective third-order nonlinearity. The SHG bandwidth is relatively narrow (0.17 nm for a QPM grating length of 60 mm), where the pump frequency is fixed by the quasi-phasematching grating in the mixer. Near degeneracy (where both the signal and output frequencies are relatively close to the pump frequency), the signal bandwidth is very large (around 45 nm for the same 60 mm length). This cascaded mixing phenomenon has been used by several groups in different material systems to demonstrate simultaneous conversion of multiple signals with identical conversion efficiency [13], as well as optical switching [79, 88, 89].

5.2.1 Theory of Cascaded SHG/DFG

Although the $\chi^{(2)} : \chi^{(2)}$ interactions are known as cascaded processes, the SHG and DFG processes occur simultaneously. In order to fully describe the mixing interactions, a fourth equation (describing SHG of the pump to generate the local oscillator) must be added to the coupled mode equations presented in Section 2.2. Those equations, in the phasematched condition ($\Delta k = 0$), become:

$$\frac{dA_P}{dz} = -j\sqrt{\eta_{nor}}A_P^* A_{LO} - \frac{\alpha_P}{2}A_P \tag{5.8}$$

$$\frac{dA_{LO}}{dz} = -j\sqrt{\eta_{nor}}A_P^2 - 2j\sqrt{\eta_{nor}}A_S A_{OUT} - \frac{\alpha_{LO}}{2}A_{LO} \tag{5.9}$$

$$\frac{dA_{SIG}}{dz} = -j\sqrt{\eta_{nor}}A_{LO}A_{OUT}^* - \frac{\alpha_{SIG}}{2}A_{SIG} \tag{5.10}$$

$$\frac{dA_{OUT}}{dz} = -j\sqrt{\eta_{nor}}A_{LO}A_{SIG}^* - \frac{\alpha_O}{2}A_{OUT} \tag{5.11}$$

where the coupling coefficient η_{nor} is the value for second harmonic generation. Near degeneracy, the coefficient for DFG is identical to that for SHG, hence all four equations use the same coupling factor. The wavelength conversion efficiency can be defined as:

$$\eta_{DFG} = \frac{P_{OUT}(L)}{P_S(0)} \approx \frac{\eta_{nor}^2 L^4 [P_P(0)]^2}{4} \tag{5.12}$$

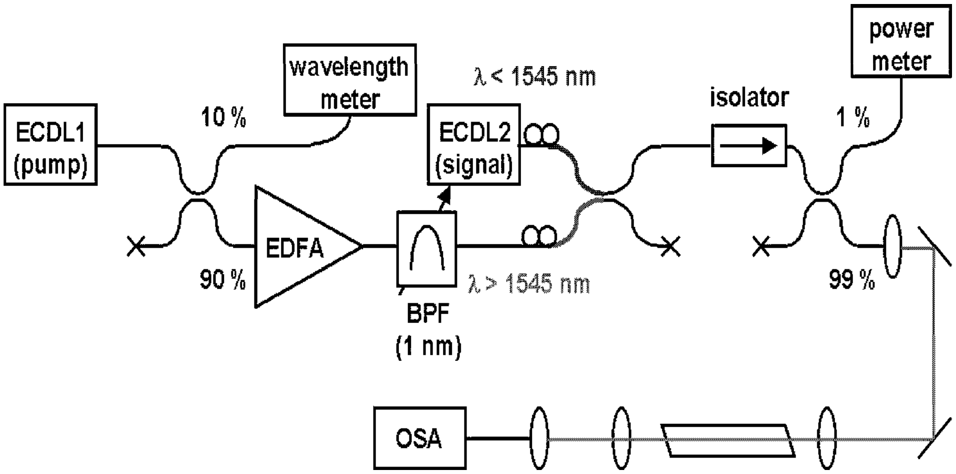

Figure 5.10: Experimental apparatus for wavelength conversion through cascaded SHG/DFG processes.

where the rightmost expression is obtained in the absence of loss, assuming that the pump remains relatively undepleted. Since there are two $\chi^{(2)}$ processes involved here, the efficiency η_{DFG} increases as η_{nor}^2 and L^4, such that improvements in device quality are even more beneficial than in the case of SHG alone.

5.2.2 $\chi^{(2)} : \chi^{(2)}$ Wavelength Conversion Experiment Using a Buried Waveguide

The apparatus used to observe wavelength conversion is shown in Figure 5.10. This experiment involves combining two signals in the 1550 nm band, which requires the use of a red/blue WDM coupler. This commercially available component combines wavelengths above and below 1545 nm with reasonably low (< 0.3 dB) insertion loss at each input wavelength. External cavity diode lasers (ECDLs) are used as sources for the signal and pump. A high-power erbium doped fiber amplifier (EDFA) is used to amplify the pump for high efficiency wavelength conversion. The tunable bandpass filter (BPF) suppresses the ASE from the EDFA, which would otherwise serve as a noise source that degrades the signal-to-noise ratio of the generated output wave. The combined waves are launched into the device using free-space optics, with

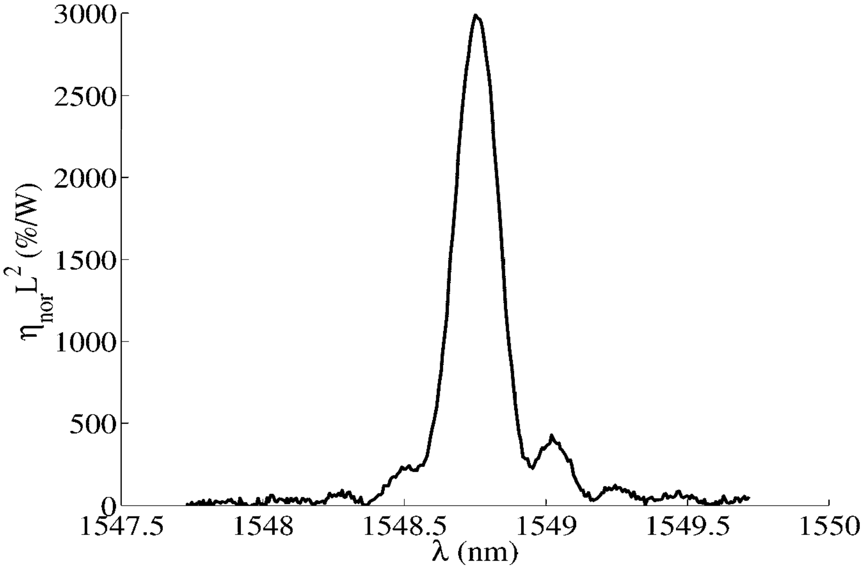

Figure 5.11: Low power CW SHG tuning curve for device used in cascaded wavelength conversion experiment.

the outputs coupled into an optical fiber for measurement on an optical spectrum analyzer (OSA). The experiment was done at 120°C to mitigate photorefraction. The device used in this experiment was fabricated using the annealed and reverse proton-exchange process described in Chapter 3. A low power CW SHG tuning curve is shown in Figure 5.11, where the peak conversion efficiency is $\eta_{nor}L^2 = 3000$ %/W.

Figure 5.12 shows an OSA trace at the output of the waveguide, with the pump wave off and on at the maximum available power. With the pump off, the signal level is -12.9 dBm. Accounting for the Fresnel reflection at the output facet and the propagation loss in the waveguide, the signal power at the input of the waveguide is roughly -10.7 dBm. When the pump is turned up to a level of 180 mW in the waveguide, the generated power at the waveguide output is -8.9 dBm, indicating an external wavelength conversion efficiency of +1.8 dB. This DFG is accompanied by an internal parametric gain of roughly 5 dB. Figure 5.13 shows the variation of η_{DFG} with pump power, where 0 dB wavelength conversion is observed with only 160 mW input. A calculation using the measured $\eta_{nor}L^2 = 3000$ %/W along with reasonable

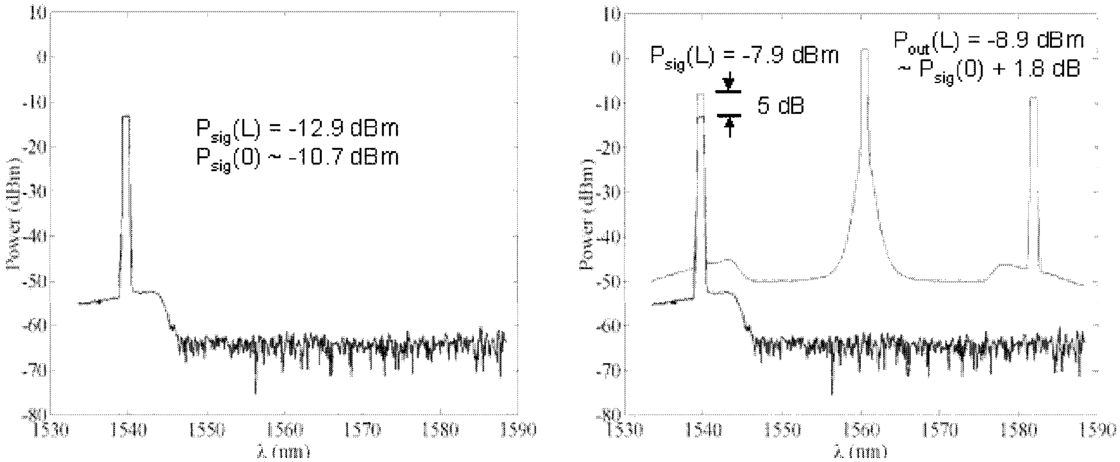

Figure 5.12: Optical spectrum analyzer traces showing signal and output transmission with and without pump power. Internal (external) parametric gain of 5 dB (1.8 dB) is observed at a pump power of 180 mW.

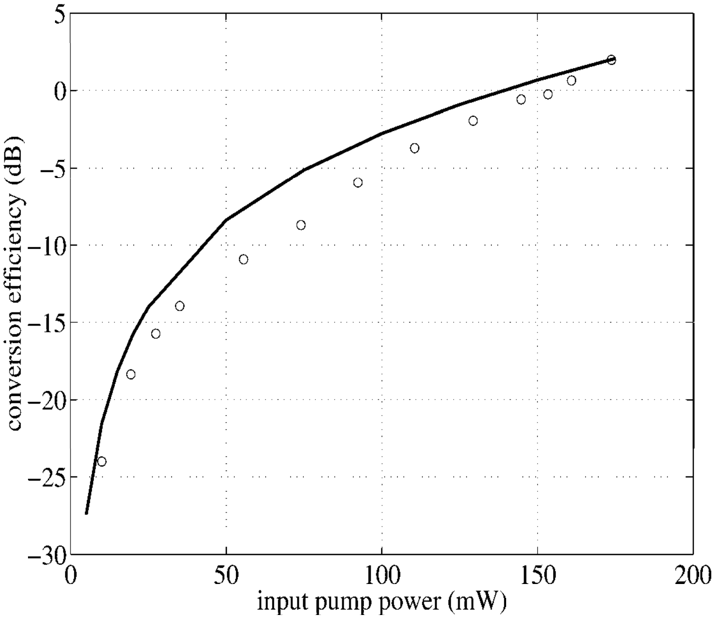

Figure 5.13: Plot of measured and calculated DFG efficiency as a function of pump power with $\eta_{nor}L^2 = 3000$ %/W.

loss values of 0.35 dB/cm and 0.70 dB/cm at 1550 nm and 775 nm respectively is also shown. Agreement is reasonable, although the measured efficiency is lower than the calculation for the intermediate power levels. Despite the high temperature operation, as the input pump power was increased, drifting of the phasematching wavelength was observed. This instability may be the cause for the discrepancy between theory and measurement, as some of the data points may have been taken with the pump wavelength slightly away from the nominal phasematching point.

5.3 Conclusion

The experiments described in this chapter involve the use of optical frequency mixers for telecommunications applications. The high quality mixers permit very efficient optical gating and wavelength conversion. Further improvement in device efficiency and material properties should allow for improved system performance with lower pump powers, as discussed in the next chapter.

Chapter 6

Summary and Future Directions

This final chapter summarizes the contributions of this dissertation, and presents possible future research directions, including advanced applications and novel material technologies.

6.1 Summary of Contributions

The primary objective of this work was the development of highly efficient optical frequency mixers. This goal was achieved, as evidenced by the following accomplishments:

- optimization of annealed proton-exchange to produce a device with a normalized conversion efficiency of $\eta_{nor}L^2$ =1400 %/W
- development of buried waveguides in PPLN using annealed and reverse proton-exchange
- demonstration of the highest normalized conversion efficiency reported to date in an optical frequency mixer (η_{nor} = 150 %/W-cm^2)

Given these highly efficient devices, a second objective was a study of their behavior in the regime of strong pump depletion, which led to the two experiments described in Chapter 4:

- observation of 99 % pump depletion for the first time in single-pass SHG in a quasi-CW configuration
- observation of Jacobi elliptic tuning curves in the strongly depleted limit

Telecommunications applications of frequency mixing are also greatly facilitated by the high efficiency of the devices developed in this work, as was demonstrated by the experiments presented in Chapter 5:

- implementation of nearly-complete all-optical gating using sum frequency generation
- observation of 0 dB wavelength conversion using cascaded SHG/DFG with only 160 mW pump power
- observation of 1.8 dB (external) and 5 dB (internal) parametric gain with less than 200 mW pump power

6.2 Future Directions

6.2.1 System Applications

Like their electrical counterparts, optical frequency mixers are very versatile. Several functions implemented with this device technology have been presented in this dissertation. When used in conjunction with other optical devices, more complex signal processing is possible. Tunable fiber Bragg gratings (FBGs), for example, allow for introducing wavelength-dependent delays in a system. These gratings have been used in conjunction with wavelength conversion in OF mixers to demonstrate functions such as time-slot interchange in a TDM system [90], and all-optical header recognition in a packet switched network [91]. These experiments used wavelength converters identical to those described in this work. The tuning behavior of OF mixers can be engineered to allow for multiple pump and signal channels through application of Fourier transform grating structures [92]. These structures can facilitate more complex optical signal processing functions.

Highly efficient SHG and OPA have many potential applications in quantum optics. Experiments involving amplitude squeezing of light using SHG have already been performed [69] with APE waveguides. The buried waveguides described in Chapter 3 can allow for much greater levels of squeezing at lower pump powers. These experiments can be done with simple straight waveguides. Implementation of squeezing using degenerate OPA requires development of integrated optical structures such as directional couplers and wavelength selective attenuators in RPE waveguides. Modeling of such structures will demand a better understanding of the proton diffusion process in the low concentration regime formed in buried waveguides, as well as extension of the material dispersion model to longer wavelengths. Both of these efforts are currently being pursued [68].

The large modulation bandwidth made available by parametric processes makes OF mixers attractive for processing of high-speed time division multiplexed signals [17]. More complex functions like TDM to WDM conversion can be implemented efficiently with buried waveguides, however these will require the same bends, couplers, and other integrated optics structures needed for quantum optics (Figure 6.1).

6.2.2 Novel Materials

As discussed in Section 3.1, several properties must be considered when choosing a material for mixer applications. Cost, availability and the ability to implement quasi-phasematching are perhaps the most important traits, particularly for devices being considered for widespread commercial use. Annealed and reverse proton-exchanged waveguides in periodically-poled lithium niobate have proven to be a good choice given these considerations.

Other waveguide fabrication techniques have recently shown promising results. Vapor phase proton-exchange, for example, has been used to form waveguides with large index steps, undegraded nonlinear coefficients and relatively low (0.35 dB/cm @ 1550 nm) losses [93]. The low proton concentration of the vapor as compared to the liquid melt results in a much less aggressive exchange, which may be the explanation for the higher material quality. Channel waveguides fabricated in this manner could

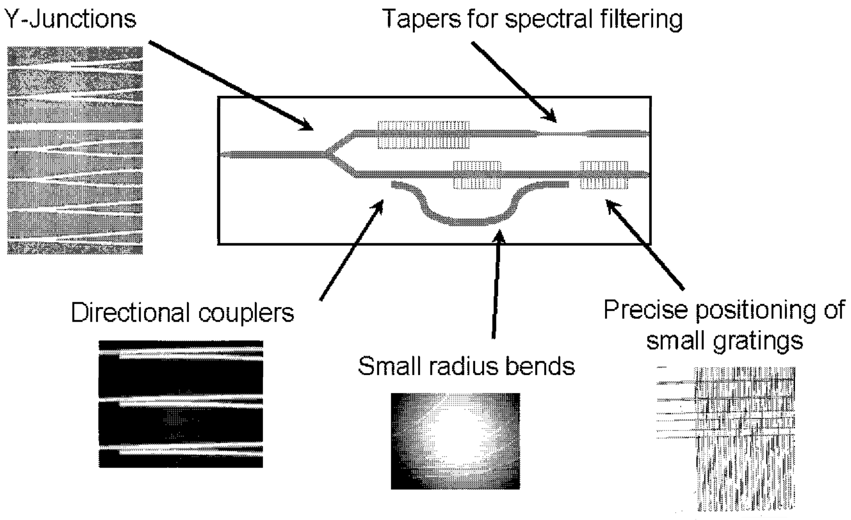

Figure 6.1: Various novel integrated optics structures implemented lithographically in silicon dioxide mask sputtered on PPLN substrate. These structures provide useful functions in nonlinear waveguides. Accurate modeling of APE and RPE processes will allow for better design of these structures. Figure courtesy of Jonathan Kurz.

provide higher confinement than the best RPE guides, allowing for significant gains in conversion efficiency.

Lithium niobate has some unattractive properties. The congruent composition of this crystal (which is the most straightforward to grow) is susceptible to photorefractive perturbations. Although this problem can be largely mitigated by high temperature operation, it is a major concern for those exploring commercial applications of optical frequency mixers. Annealed and reverse proton-exchanged waveguides in PPLN are less photorefractive than those formed by titanium indiffusion, however the devices still need to be held at high temperature ($\approx$ 120°C) in order to operate stably when pumped with high power. Doping lithium niobate with MgO has been found to greatly reduce photorefractive sensitivity [94]. Periodic poling and waveguide fabrication have been implemented in this doped substrate by other groups for blue light generation [6], hence there is great potential for its use in the communications band. A good understanding of the proton diffusion process and material dispersion in this material are needed in order to design waveguide devices optimized in the manner described in Chapter 3. This work is currently being undertaken by groups at Stanford and elsewhere. Zinc indiffusion is another approach to reducing photorefraction [95]. Waveguides formed using vapor phase zinc diffusion have been shown to have fairly high refractive index steps for both polarizations [96], while the lower photorefraction of the zinc allows for lower temperature operation of frequency mixers [97]. Optimization of these structures could lead to polarization-insensitive mixers that operate at room temperature. The stoichiometric composition of $LiNbO_3$ (where the [Li]/([Li]+[Nb]) ratio is 50 %, as opposed to 48 % in the congruent case) has also been found to have attractive properties, including low coercive field [98] that facilitates poling of thicker substrates for bulk devices.

Many semiconductors appear to be well suited for application in optical frequency mixers. Many of these materials exhibit strong nonlinearities, wide optical transparency, and are available at reasonable cost with good substrate quality. Gallium arsenide (GaAs), for example, has a nonlinear coefficient that is roughly three times that of lithium niobate. Accounting for its higher index of refraction, the nonlinear figure of merit (d^2/n^3) for GaAs is roughly 2.5 times that of lithium niobate. GaAs is also transparent much further into the infrared region of the electromagnetic spectrum (12 μm vs 4.5 μm), allowing it to be used for generation of frequencies useful in spectroscopy. The primary difficulty here is the implementation of quasi-phasematching structures. Zincblende semiconductors are not ferroelectric, so post-growth electric-field poling is not possible. The sign of the nonlinearity can however be inverted by a 90° rotation of the crystal axis. Eyres et al have recently demonstrated a novel all-epitaxial approach to implementing orientation-patterned GaAs (OPGaAs) [99]. This technique involves using GaAs/Ge/GaAs heteroepitaxy to create an inverted or antiphase layer on a GaAs substrate. Subsequent lithographic patterning and regrowth results in a bulk quasi-phasematched nonlinear optical structure. Work on implementation of low-loss waveguides for mixing in the telecommunications band is ongoing.

6.3 Conclusion

The highly efficient optical frequency mixers described in this dissertation clearly have many useful applications. Further development of the technology described here and extension of these techniques to new materials and systems appears to be a promising area of research.

Appendix A

List of Journal Publications and Conference Presentations

A.1 Journal Publications

1. K. R. Parameswaran, R. K. Route, J. R. Kurz, R. V. Roussev, M. M. Fejer, and M. Fujimura, “Highly efficient SHG in buried waveguides formed using annealed and reverse proton exchange in PPLN,” *Optics Letters*, 27(3):179 – 181, February 2002.

2. K. R. Parameswaran, J. R. Kurz, R. V. Roussev, and M. M. Fejer, “Observation of 99 % pump depletion in single pass SHG in a PPLN waveguide,” *Optics Letters*, 27(1):43 – 45, January 2002.

3. K. R. Parameswaran, M. Fujimura, M. H. Chou, and M. M. Fejer, “Low-power all-optical gate based on sum frequency mixing in APE waveguides in PPLN,” *IEEE Photonics Technology Letters*, 12(6):654 – 656, June 2000.

4. R. Harel, W. H. Burkett, G. Lenz, E. E. Chaban, K. R. Parameswaran, M. M. Fejer, and I. Brener, “Interchannel cross talk caused by pump depletion in periodically poled $LiNbO_3$ waveguide wavelength converters,” *Journal of the Optical Society of America B*, 19(4):849 – 851, April 2002.

5. Z. Zheng, A. M. Weiner, K. R. Parameswaran, M. H. Chou, and M. M. Fejer, "Femtosecond second-harmonic generation in periodically poled lithium niobate waveguides with simultaneous strong pump depletion and group-velocity walk-off," *Journal of the Optical Society of America B*, 19(4):839 – 848, April 2002.
6. M. C. Cardakli, D. Gurkan, S. A. Havstad, A. E. Willner, K. R. Parameswaran, M. M. Fejer, and I. Brener, "Tunable all-optical time-slot-interchange and wavelength conversion using difference-frequency-generation and optical buffers," *IEEE Photonics Technology Letters*, 14(2):200 – 202, February 2002.
7. J. R. Kurz, K. R. Parameswaran, R. V. Roussev, and M. M. Fejer, "Optical-frequency balanced mixer," *Optics Letters*, 26(16):1283 – 1285, August 2001.
8. K. Gallo, G. Assanto, K. R. Parameswaran, and M. M. Fejer, "All-optical diode in a periodically poled lithium niobate waveguide," *Applied Physics Letters*, 79(3):314 – 316, July 2001.
9. Z. Zheng, A. M. Weiner, K. R. Parameswaran, M. H. Chou, and M. M. Fejer, "Low-power spectral phase correlator using periodically poled $LiNbO_3$ waveguides," *IEEE Photonics Technology Letters*, 13(4):376 – 378, April 2001.
10. G. S. Kanter, P. Kumar, K. R. Parameswaran, M. H. Chou, and M. M. Fejer, "Wavelength-selective pulsed all-optical switching based on cascaded second-order nonlinearity in a periodically poled lithium-niobate waveguide," *IEEE Photonics Technology Letters*, 13(4):341 – 343, April 2001.
11. I. Brener, B. Mikkelsen, G. Raybon, R. Harel, K. Parameswaran, J. R. Kurz, and M. M. Fejer, "160 Gbit/s wavelength shifting and phase conjugation using periodically poled $LiNbO_3$ waveguide parametric converter," *Electronics Letters*, 36(21):1788 – 1790, October 2000.
12. M. H. Chou, K. R. Parameswaran, M. M. Fejer, and I. Brener, "Optical signal processing and switching with second-order nonlinearities in waveguides," *IEICE Transactions on Electronics*, E83C(6):869 – 874, June 2000.

13. M. H. Chou, I. Brener, G. Lenz, R. Scotti, E. E. Chaban, J. Shmulovich, D. Philen, S. Kosinski, K. R. Parameswaran, and M. M. Fejer, "Efficient wide-band and tunable mid-span spectral inverter using cascaded nonlinearities in $LiNbO_3$ waveguides," *IEEE Photonics Technology Letters*, 12(1):82 – 84, January 2000.
14. I. Brener, M. H. Chou, E. Chaban, K. R. Parameswaran, M. M. Fejer, S. Kosinski, and D. L. Pruitt, "Polarisation-insensitive wavelength converter based on cascaded nonlinearities in $LiNbO_3$ waveguides," *Electronics Letters*, 36(1):66 – 67, January 2000.
15. R. Schiek, L. Friedrich, H. Fang, G. I. Stegeman, K. R. Parameswaran, M. H. Chou, and M. M. Fejer, "Nonlinear directional coupler in periodically poled lithium niobate," *Optics Letters*, 24(22):1617 – 1619, November 1999.
16. M. H. Chou, K. R. Parameswaran, M. M. Fejer, and I. Brener, "Multiple channel wavelength conversion using engineered quasi-phasematching structures in $LiNbO_3$ waveguides," *Optics Letters*, 24(16):1157 – 1159, August 1999.
17. M. H. Chou, I. Brener, K. R. Parameswaran and M. M. Fejer, "Stability and bandwidth enhancement of difference frequency generation based wavelength conversion by pump detuning," *Electronics Letters*, 35(12):978 – 80, June 1999.

A.2 Conference Presentations

1. K. R. Parameswaran, J. R. Kurz, R. V. Roussev, and M. M. Fejer, "Observation of wavelength tuning curves during pump-depleted second harmonic generation," accepted for presentation at *OSA Topical Meeting on Nonlinear Optics (NLO) 2002*, session TuB.
2. K. R. Parameswaran, R. K. Route, J. R. Kurz, R. V. Roussev, and M. M. Fejer, "Highly efficient SHG in buried waveguides using annealed and reverse proton exchange in PPLN," *IEEE Lasers and Electro-Optics Society (LEOS) Annual Meeting 2001*, paper ThL3.

3. K. R. Parameswaran, J. R. Kurz, R. V. Roussev, and M. M. Fejer, “Observation of 99 % pump depletion in single pass SHG in a PPLN waveguide,” *Conference on Laser and Electro-Optics (CLEO) 2001*, paper CFB3.
4. K. R. Parameswaran, J. R. Kurz, R. V. Roussev, M. M. Fejer, M. H. Chou, and I. Brener, “Optical frequency mixers for WDM and TDM applications,” *SPIE Photonics West 2001*, paper 4268A-26 (invited).
5. K. R. Parameswaran, M. M. Fejer, K. Gallo, and G. Assanto, “All-optical diode in quasi-phase-matched $LiNbO_3$ waveguide,” *CLEO Europe 2000*, postdeadline paper CPD1.6.
6. K. R. Parameswaran, M. H. Chou, M. M. Fejer, I. Brener, and S. Kawanishi, “Waveguide frequency mixers for all-optical signal processing,” *NLO 2000*, Technical Digest TOPS vol. 46, pp. 156-158.
7. K. R. Parameswaran, M. Fujimura, M. H. Chou, and M. M. Fejer, “Low power all-optical gating based on sum frequency mixing in annealed proton exchanged waveguides in periodically poled lithium niobate,” *LEOS Annual Meeting 1999*, postdeadline paper PD2.5.
8. T. Ohara, H. Takara, I. Shake, K. Mori, S. Kawanishi, S. Mino, T. Yamada, M. Ishii, T. Kitoh, T. Kitagawa, K. R. Parameswaran, and M. M. Fejer, “160 Gbit/s optical-time-division multiplexer based on PPLN hybrid integrated planar lightwave circuit,” accepted for presentation at *CLEO 2002*, postdeadline session CPDB.
9. D. Gurkan, M. C. Hauer, A. B. Sahin, Z. Pan, S. Lee, A. E. Willner, K. R. Parameswaran, and M. M. Fejer, “Demonstration of multi-wavelength all-optical header recognition using a PPLN and optical correlators,” *European Conference on Optical Communications (ECOC) 2001*, paper We.B.2.5 (invited).
10. Z. Zheng, A. M. Weiner, K. R. Parameswaran, M. H. Chou, and M. M. Fejer, “Femtosecond pulse second harmonic generation under large depletion conditions in long PPLN waveguides,” *CLEO 2001*, paper CFB2.

11. M. C. Cardakli, A. B. Sahin, O. A. Adamczyk, A. E. Willner, K. R. Parameswaran, and M. M. Fejer, "All-optical wavelength shifting of subcarrier channels using difference-frequency-generation in a PPLN," *CLEO 2001*, paper CThB2.

12. G. S. Kanter, P. Kumar, M. Fiorentino, D. K. Serkland, M. M. Fejer, and K. R. Parameswaran, "Quantum-noise squeezing in periodically-poled lithium-niobate waveguides: Detection by use of a spatio-temporally matched local oscillator," *OSA Annual Meeting 2000*, paper WM3.

13. R. Schiek, W. Elflein, T. Pertsch, A. Tuennermann, K. R. Parameswaran, and M. M. Fejer, "Femtosecond all-optical switching in a lithium niobate directional coupler with cascaded nonlinearity, *NLO 2000*, paper TuD6 (invited).

14. R. Schiek, C. G. Trevino-Palacios, J. Meier, H. Fang, L. Friedrich, G. I. Stegeman, K. R. Parameswaran, M. H. Chou, and M. M. Fejer, "High-power second harmonic generation experiments in periodically poled lithium niobate waveguides," *CLEO 2000*, paper CWH2.

15. Z. Zheng, A. M. Weiner, K. R. Parameswaran, M. H. Chou, and M. M. Fejer, "All-optical recognition of spectrally coded optical pulses using periodically poled lithium niobate second harmonic waveguides for ultrashort pulse optical code division multiple access," *CLEO 2000*, paper CTuD4.

16. I. Brener, B. Mikkelsen, K. Rottwitt, W. Burkett, G. Raybon, J. B. Stark, K. R. Parameswaran, M. H. Chou, M. M. Fejer, E. E. Chaban, R. Harel, D. L. Philen, and S. Kosinski, "Cancellation of all Kerr nonlinearities in long fiber spans using a $LiNbO_3$ phase conjugator and Raman amplification," *OFC 2000*, postdeadline paper PD33-1.

17. M. C. Cardakli, D. Gurkan, S. A. Havstad, A. E. Willner, K. R. Parameswaran, M. M. Fejer, and I. Brener, "All-optical time-slot-interchange and wavelength conversion using difference-frequency-generation and FBGs," *OFC 2000*, postdeadline paper PD10-1.

18. M. M. Fejer, M. H. Chou, K. R. Parameswaran, I. Brener, "Optical frequency mixers for WDM and TDM applications," *OFC 2000*, paper FB1 (invited).

19. I. Brener, M. H. Chou, E. Chaban, K. R. Parameswaran, M. M. Fejer, and S. Kosinski, "Polarization-insensitive parametric wavelength converter based on cascaded nonlinearities in $LiNbO_3$ waveguides," *OFC 2000*, paper TuF1.

20. M. H. Chou, K. R. Parameswaran, and M. M. Fejer, "Wide bandwidth 1.5 μm and 1.3 μm wavelength conversion in periodically-poled waveguides," *Nonlinear Guide Waves Conference (NLGW) 1999*, paper FA5 (invited).

21. M. H. Chou, I. Brener, K. R. Parameswaran and M. M. Fejer, "Stability and bandwidth enhancement of difference frequency generation based wavelength conversion by pump detuning," *CLEO 1999*, paper CWB8.

22. M. H. Chou, K. R. Parameswaran, M. M. Fejer, I. Brener, "Multiple channel wavelength conversion using engineered quasi-phase-matching structures in $LiNbO_3$ waveguides," *CLEO 1999*, paper CTuW7 (invited).

23. I. Brener, M. H. Chou, G. Lenz, R. Scotti, E. E. Chaban, J. Shmulovich, D. Philen, S. Kosinski, K. R. Parameswaran, and M. M. Fejer, "High efficiency (-7 dB), wideband (70 nm) and tunable $LiNbO_3$ -waveguide mid-span spectral inverter and its use for dispersion compensation in 4x10 Gb/s," *ECOC 1999.*

24. M. H. Chou, I. Brener, K. R. Parameswaran and M. M. Fejer, "Quasi-phasematched waveguides: From ultrashort pulses to signal processing for optical communications", *European Conference on Integrated Optics (ECIO) 1999* (invited).

25. M. H. Chou, K. R. Parameswaran, I. Brener and M. M. Fejer, "Three wave mixing for WDM applications," *IEEE LEOS Topical Meeting on WDM components 1999*, (invited).

26. M. H. Chou, K. R. Parameswaran, M. A. Arbore, J. Hauden, and M. M. Fejer, "Bidirectional wavelength conversion between 1.3 μm and 1.5 μm telecommunications

bands using difference frequency mixing in $LiNbO_3$ waveguides with integrated coupling structures," *CLEO 1998*, paper CThZ2.

Bibliography

[1] S.-K. Choi, R.-D. Li, C. Kim, and P. Kumar, "Traveling-wave optical parametric amplifier: investigation of its phase-sensitive and phase-insensitive gain response," *Journal of the Optical Society of America B (Optical Physics)*, 14(7):1564 – 75, July 1997.

[2] E. Desurvire, *Erbium-doped fiber amplifiers : principles and applications*, Wiley, New York, 1994.

[3] M. Saruwatari, "All-optical signal processing for terabit/s optical transmission," *IEEE Journal of Selected Topics in Quantum Electronics*, 6(6):1363 – 74, November 2000.

[4] P.A. Franken, A.E. Hill, C.W. Peters, and G. Weinreich, "Generation of optical harmonics," *Phys. Rev. Lett.*, 7:118 – 120, 1961.

[5] C. Frederickson, "Diode-pumped solid-state lasers continue industrial expansion," *Photonics Spectra*, 33(1):108, January 1999.

[6] Y. Kitaoka, K. Mizuuchi, T. Yokoyama, K. Yamamoto, K. Narumi, and M. Kato, "Quasi-phase-matched second harmonic generation device in Mg-doped $\mathrm{LiNbO_3}$ and its application to high-density optical disk system," *Bulletin of Materials Science*, 22(3):405 – 11, May 1999.

[7] J.E. Midwinter and J. Warner, "Effects of phase matching method and of uniaxial crystal symmetry on polar distribution of second-order non-linear optical polarization," *Brit. Jour. App. Phys.*, 16(8):1135, 1965.

[8] M.V. Hobden, "Phase-matched 2nd-harmonic generation in biaxial crystals," *Jour. App. Phys.*, 38(11):4365, 1967.

[9] M.M. Fejer, G.A. Magel, D.H. Jundt, and R.L. Byer, "Quasi-phase-matched second harmonic generation: tuning and tolerances," *IEEE Journal of Quantum Electronics*, 28(11):2631 – 2654, November 1992.

[10] R.L. Byer, "Parametric oscillators and nonlinear materials," in *Nonlinear Optics*, edited by P.G. Harper and B.S. Wherrett (Academic Press, New York, 1977), pp. 47-160.

[11] G.D. Boyd and D.A. Kleinman, "Parametric interaction of focused gaussian light beams," *Jour. App. Phys.*, 39(8):3597 – 3639, July 1968.

[12] C.Q. Xu, H. Okayama, K. Shinozaki, K. Watanabe, and M. Kawahara, "Wavelength conversions ≈ 1.5 μm by difference frequency generation in periodically domain-inverted $LiNbO_3$ channel waveguides," *Applied Physics Letters*, 63(9):1170 – 2, August 1993.

[13] M.H. Chou, I. Brener, M.M. Fejer, E.E. Chaban, and S.B. Christman, "1.5-μm-band wavelength conversion based on cascaded second-order nonlinearity in $LiNbO_3$ waveguides," *IEEE Photonics Technology Letters*, 11(6):653 – 5, June 1999.

[14] C.Q. Xu, H. Okayama, and M. Kawahara, "Wavelength conversions between the two silica fibre loss windows at 1.31 and 1.55 μm using difference frequency generation," *Electronics Letters*, 30(25):2168 – 9, December 1994.

[15] M.H. Chou, K.R. Parameswaran, M.A. Arbore, J. Hauden, and M.M. Fejer, "Bidirectional wavelength conversion between 1.3- and 1.5- μm telecommunication bands using difference frequency mixing in $LiNbO_3$ waveguides with integrated coupling structures," in *Technical Digest Summaries of papers presented at the Conference on Lasers and Electro-Optics*, paper CThZ2, May 1998.

[16] M.H. Chou, I. Brener, G. Lenz, R. Scotti, E.E. Chaban, J. Shmulovich, D. Philen, S. Kosinski, K.R. Parameswaran, and M.M. Fejer, “Efficient wide-band and tunable midspan spectral inverter using cascaded nonlinearities in $LiNbO_3$ waveguides,” *IEEE Photonics Technology Letters*, 12(1):82 – 4, January 2000.

[17] S. Kawanishi, M.H. Chou, K. Fujiura, M.M. Fejer, and T. Morioka, “All-optical modulation and time-division-multiplexing of 100 Gbit/s signal using quasi-phase matched mixing in $LiNbO_3$ waveguides,” *Electronics Letters*, 36(18):1568 – 9, August 2000.

[18] A.W. Snyder and J.D. Love, *Optical waveguide theory*, London, UK : Chapman & Hall, 1983.

[19] M.L. Bortz, L.A. Eyres, and M.M. Fejer, “Depth profiling of the d_{33} nonlinear coefficient in annealed proton exchanged $LiNbO_3$ waveguides,” *Applied Physics Letters*, 62(17):2012 – 14, April 1993.

[20] D. Marcuse, *Theory of Dielectric Optical Waveguides*, Harcourt Brace Jovanovich, Boston, 1991.

[21] J.A. Armstrong, N. Bloembergen, J. Ducuing, and P.S. Pershan, “Interactions between light waves in a nonlinear dielectric,” *Physical Review*, 127:1918 – 39, 1962.

[22] P.A. Franken and J.F. Ward, “Optical harmonics and nonlinear phenomena,” *Rev. Mod. Phys.*, 35:23 – 39, 1963.

[23] S. Helmfrid, G. Arvidsson, and J. Webjorn, “Influence of various imperfections on the conversion efficiency of second-harmonic generation in quasi-phase-matching lithium niobate waveguides,” *Journal of the Optical Society of America B (Optical Physics)*, 10(2):222 – 9, February 1993.

[24] C.K. Campbell, *Surface Acoustic Wave Devices for Mobile and Wireless Communications*, Academic Press, San Diego, 1998.

[25] E.L. Wooten, K.M. Kissa, A. Yi-Yan, E.J. Murphy, D.A. Lafaw, P.F. Hallemeier, D. Maack, D.V. Attanasio, D.J. Fritz, G.J. McBrien, and D.E. Bossi, "A review of lithium niobate modulators for fiber-optic communications systems," *IEEE Journal of Selected Topics in Quantum Electronics*, 6(1):69 – 82, January 2000.

[26] E.J. Lim, M.M. Fejer, R.L. Byer, and W.J. Kozlovsky, "Blue light generation by frequency doubling in periodically poled lithium niobate channel waveguide," *Electronics Letters*, 25(11):731 – 2, May 1989.

[27] M.L. Bortz, M.A. Arbore, and M.M. Fejer, "Quasi-phase-matched optical parametric amplification and oscillation in periodically poled $LiNbO_3$ waveguides," *Optics Letters*, 20(1):49 – 51, January 1995.

[28] M.A. Arbore and M.M. Fejer, "Singly resonant optical parametric oscillation in periodically poled lithium niobate waveguides," *Optics Letters*, 22(3):151 – 3, February 1997.

[29] T. Suhara and H. Ishizuki, "Integrated QPM sum-frequency generation interferometer device for ultrafast optical switching," *IEEE Photonics Technology Letters*, 13(11):1203 – 5, November 2001.

[30] C.Q. Xu, K. Fujita, A.R. Pratt, Y. Ogawa, and T. Kamijoh, "Optimization of 1.5 μm-band $LiNbO_3$ quasiphase matched wavelength converters for optical communication systems," *IEICE Transactions on Electronics*, E83-C(6):884 – 91, June 2000.

[31] D. Hofmann, G. Schreiber, C. Haase, H. Herrmann, W. Grundkotter, R. Ricken, and W. Sohler, "Quasi-phase-matched difference-frequency generation in periodically poled $Ti : LiNbO_3$ channel waveguides," *Optics Letters*, 24(13):896 – 8, July 1999.

[32] M.E. Lines and A.M. Glass, *Principles and Applications of Ferroelectrics and Related Materials*, Oxford University Press, New York, 2001.

[33] G.A. Magel, M.M. Fejer, and R.L. Byer, "Quasi-phase-matched second harmonic generation of blue light in periodically poled $LiNbO_3$," *Applied Physics Letters*, 56(2):108 – 10, January 1990.

[34] H. Ito, C. Takyu, and H. Inaba, "Fabrication of periodic domain grating in $LiNbO_3$ by electron beam writing for application of nonlinear optical processes," *Electronics Letters*, 27(14):1221 – 2, July 1991.

[35] S. Miyazawa, "Ferroelectric domain inversion in Ti-diffused $LiNbO_3$ optical waveguide," *Journal of Applied Physics*, 50(7):4599 – 603, July 1979.

[36] E.J. Lim, M.M. Fejer, and R.L. Byer, "Second-harmonic generation of green light in periodically poled planar lithium niobate waveguide," *Electronics Letters*, 25(3):174 – 5, February 1989.

[37] M. Yamada, N. Nada, M. Saitoh, and K. Watanabe, "First-order quasi-phased matched $LiNbO_3$ waveguide periodically poled by applying an external field for efficient blue second-harmonic generation," *Applied Physics Letters*, 62(5):435 – 6, February 1993.

[38] S. Matsumoto, E.J. Lim, H.M. Hertz, and M.M. Fejer, "Quasiphase-matched second harmonic generation of blue light in electrically periodically-poled lithium tantalate waveguides," *Electronics Letters*, 27(22):2040 – 2, October 1991.

[39] A.A. Ballman, "Growth of piezoelectric and ferroelectric materials by czochralski technique," *J. Am. Ceram. Soc.*, 48:112, 1965.

[40] K. Nassau, H. Levinstein, and G. Loiacono, "Ferroelectric lithium niobate .2. preparation of single domain crystals," *J. Phys. Chem. Solids*, 27:989, 1966.

[41] L.E. Myers, R.C. Eckardt, M.M. Fejer, R.L. Byer, W.R. Bosenberg, and J.W. Pierce, "Quasi-phase-matched optical parametric oscillators in bulk periodically poled $LiNbO_3$," *Journal of the Optical Society of America B (Optical Physics)*, 12(11):2102 – 16, November 1995.

[42] G.D. Miller, R.G. Batchko, W.M. Tulloch, D.R. Weise, M.M. Fejer, and R.L. Byer, "42 % efficient single-pass CW second-harmonic generation in periodically poled lithium niobate," *Optics Letters*, 22(24):1834 – 6, December 1997.

[43] G.D. Miller, R.G. Batchko, M.M. Fejer, and R.L. Byer, "Visible quasi-phase-matched harmonic generation by electric-field-poled lithium niobate," *Proceedings of the SPIE*, 2700:34 – 45, 1996.

[44] G.D. Miller, "Periodically-poled lithium niobate: modeling, fabrication, and nonlinear-optical performance," *Ph.D. Dissertation*, Department of Electrical Engineering, Stanford University, Stanford, CA, June 1998.

[45] J.R. Kurz, Personal communication 2001.

[46] J.R. Kurz, K.R. Parameswaran, R.V. Roussev, and M.M. Fejer, "Optical-frequency balanced mixer," *Optics Letters*, 26(16):1283 – 5, August 2001.

[47] J.R. Kurz, A.M. Schober, D.S. Hum, A.J. Saltzman, and M.M. Fejer, "Nonlinear physical optics with transversely patterned quasi-phase-matching gratings," *submitted to IEEE Journal of Selected Topics in Quantum Electronics*, 2002.

[48] M. Minakata, S. Saito, M. Shibata, and S. Miyazawa, "Precise determination of refractive-index changes in Ti-diffused $LiNbO_3$ optical waveguides," *Journal of Applied Physics*, 49(9):4677 – 82, September 1978.

[49] J.L. Jackel, C.E. Rice, and J.J. Veselka, "Proton exchange for high-index waveguides in $LiNbO_3$," *Applied Physics Letters*, 41(7):607 – 8, October 1982.

[50] E. Schiller, E. Herreros, and G. Lifante, "Optical characterization of vapor Zn-diffused waveguides in lithium niobate," *Journal of the Optical Society of America A (Optics, Image Science and Vision)*, 14(2):425 – 9, February 1997.

[51] T. Fujiwara, X. Cao, R. Srivastava, and R.V. Ramaswamy, "Photorefractive effect in annealed proton-exchanged $LiNbO_3$ waveguides," *Applied Physics Letters*, 61(7):743 – 5, August 1992.

[52] J.T. Cargo, A.J. Filo, M.C. Hughes, V.C. Kannan, F.A. Stevie, and J.A. Taylor, "Characterization of sulfuric acid proton-exchanged lithium niobate," *Journal of Applied Physics*, 67(2):627 – 33, January 1990.

[53] N. Goto and G.L. Yip, "Characterization of proton-exchange and annealed $LiNbO_3$ waveguides with pyrophosphoric acid," *Applied Optics*, 28(1):60 – 5, January 1989.

[54] Yu.N. Korkishko, V.A. Fedorov, M.P. De Micheli, P. Baldi, K.E. Hadi, and A. Leycuras, "Relationships between structural and optical properties of proton-exchanged waveguides on Z-cut lithium niobate," *Applied Optics*, 35(36):7056 – 60, December 1996.

[55] Yu.N. Korkishko, V.A. Fedorov, and F. Laurell, "The SHG-response of different phases in proton exchanged lithium niobate waveguides," *IEEE Journal of Selected Topics in Quantum Electronics*, 6(1):132 – 42, January 2000.

[56] M.L. Bortz and M.M. Fejer, "Annealed proton-exchanged $LiNbO_3$ waveguides," *Optics Letters*, 16(23):1844 – 6, December 1991.

[57] M.H. Chou, J. Hauden, M.A. Arbore, and M.M. Fejer, "1.5- μm-band wavelength conversion based on difference-frequency generation in $LiNbO_3$ waveguides with integrated coupling structures," *Optics Letters*, 23(13):1004 – 6, July 1998.

[58] E.J. Lim, S. Matsumoto, and M.M. Fejer, "Noncritical phase matching for guided-wave frequency conversion," *Applied Physics Letters*, 57(22):2294 – 6, November 1990.

[59] M.L. Bortz, S.J. Field, M.M. Fejer, D.W. Nam, R.G. Waarts, and D.F. Welch, "Noncritical quasi-phase-matched second harmonic generation in an annealed proton-exchanged $LiNbO_3$ waveguide," *IEEE Journal of Quantum Electronics*, 30(12):2953 – 60, December 1994.

[60] K.R. Parameswaran, J.R. Kurz, R.V. Roussev, M.M. Fejer, M.H. Chou, I. Brener, S. Kawanishi, K. Fujiura, and T. Morioka, "Optical frequency mixers for WDM and TDM applications," *Proceedings of the SPIE*, 4268:123 – 33, 2001.

[61] J. Rams, J. Olivares, and J.M. Cabrera, "SHG-capabilities of reverse PE-$LiNbO_3$ waveguides," *Electronics Letters*, 33(4):322 – 3, February 1997.

[62] J.L. Jackel and J.J. Johnson, "Reverse exchange method for burying proton exchanged waveguides," *Electronics Letters*, 27(15):1360 – 1, July 1991.

[63] M. Digonnet, M. Fejer, and R. Byer, "Characterization of proton-exchanged waveguides in $MgO : LiNbO_3$," *Optics Letters*, 10(5):235 – 7, May 1985.

[64] Yu.N. Korkishko, V.A. Fedorov, T.M. Morozova, F. Caccavale, F. Gonella, and F. Segato, "Reverse proton exchange for buried waveguides in $LiNbO_3$," *Journal of the Optical Society of America A (Optics, Image Science and Vision)*, 15(7):1838 – 42, July 1998.

[65] P.K. Tien and R. Ulrich, "Theory of prism-film coupler and thin-film light guides," *Journal of the Optical Society of America*, 60(10):1325 – 37, October 1970.

[66] J.M. White and P.F. Heidrich, "Optical waveguide refractive index profiles determined from measurement of mode indices: a simple analysis," *Applied Optics*, 15(1):151 – 5, January 1976.

[67] A. Loni, G. Hay, R.M. De La Rue, and J.M. Winfield, "Proton-exchanged $LiNbO_3$ waveguides: the effects of post-exchange annealing and buffered melts as determined by infrared spectroscopy optical waveguide measurements and hydrogen isotopic exchange reactions," *Journal of Lightwave Technology*, 7(6):911 – 19, June 1989.

[68] R.V. Roussev, Personal communication 2002.

[69] D.K. Serkland, P. Kumar, M.A. Arbore, and M.M. Fejer, "Amplitude squeezing by means of quasi-phase-matched second-harmonic generation in a lithium niobate waveguide," *Optics Letters*, 22(19):1497 – 9, October 1997.

[70] R.C. Eckardt and J. Reintjes, "Phase matching limitations of high efficiency second harmonic generation," *IEEE Journal of Quantum Electronics*, QE-20(10):1178 – 87, October 1984.

[71] D. Eimerl, "High average power harmonic generation," *IEEE Journal of Quantum Electronics*, QE-23(5):575 – 92, May 1987.

[72] D. Taverner, P. Britton, P.G.R. Smith, D.J. Richardson, G.W. Ross, and D.C. Hanna, "Highly efficient second-harmonic and sum-frequency generation of nanosecond pulses in a cascaded erbium-doped fiber: periodically poled lithium niobate source," *Optics Letters*, 23(3):162 – 4, February 1998.

[73] D. Eimerl, "Quadrature frequency conversion," *IEEE Journal of Quantum Electronics*, QE-23(8):1361 – 71, August 1987.

[74] G. Imeshev, M.A. Arbore, M.M. Fejer, A. Galvanauskas, M. Fermann, and D. Harter, "Ultrashort-pulse second-harmonic generation with longitudinally nonuniform quasi-phase-matching gratings: pulse compression and shaping," *Journal of the Optical Society of America B (Optical Physics)*, 17(2):304 – 18, February 2000.

[75] G. P. Agrawal, *Nonlinear Fiber Optics*, Academic Press, San Diego, 1989.

[76] K. Inoue and H. Toba, "Wavelength conversion experiment using fiber four-wave mixing," *IEEE Photonics Technology Letters*, 4(1):69 – 72, January 1992.

[77] S. Bigo, O. Leclerc, and E. Desurvire, "All-optical fiber signal processing and regeneration for soliton communications," *IEEE Journal of Selected Topics in Quantum Electronics*, 3(5):1208 – 23, October 1997.

[78] D.F. Geraghty, R.B. Lee, M. Verdiell, M. Ziari, A. Mathur, and K.J. Vahala, "Wavelength conversion for WDM communication systems using four-wave mixing in semiconductor optical amplifiers," *IEEE Journal of Selected Topics in Quantum Electronics*, 3(5):1146 – 55, October 1997.

[79] Y. Baek, R. Schiek, G.I. Stegeman, G. Krijnen, I. Baumann, and W. Sohler, “All-optical integrated Mach-Zehnder switching due to cascaded nonlinearities,” *Applied Physics Letters*, 68(15):2055 – 7, April 1996.

[80] R. Schiek, L. Friedrich, H. Fang, G.I. Stegeman, K.R. Parameswaran, M.-H. Chou, and M.M. Fejer, “Nonlinear directional coupler in periodically poled lithium niobate,” *Optics Letters*, 24(22):1617 – 19, November 1999.

[81] N.J. Doran and D. Wood, “Nonlinear-optical loop mirror,” *Optics Letters*, 13(1):56 – 8, January 1988.

[82] K.J. Blow, N.J. Doran, and B.K. Nayar, “Experimental demonstration of optical soliton switching in an all-fiber nonlinear Sagnac interferometer,” *Optics Letters*, 14(14):754 – 6, July 1989.

[83] K.J. Blow, N.J. Doran, and B.P. Nelson, “Demonstration of the nonlinear fibre loop mirror as an ultrafast all-optical demultiplexer,” *Electronics Letters*, 26(14):962 – 4, July 1990.

[84] A.J. Poustie, R.J. Manning, and K.J. Blow, “All-optical circulating shift register using a semiconductor optical amplifier in a fibre loop mirror,” *Electronics Letters*, 32(13):1215 – 16, June 1996.

[85] I.D. Phillips, A. Gloag, P.N. Kean, N.J. Doran, I. Bennion, and A.D. Ellis, “Simultaneous demultiplexing data regeneration and clock recovery with a single semiconductor optical amplifier-based nonlinear-optical loop mirror,” *Optics Letters*, 22(17):1326 – 8, September 1997.

[86] Jiun-Haw Lee, Ding-An Wang, Yean-Woei Kiang, Hsin-Jiun Chiang, Ding-Wei Huang, and C.C. Yang, “Nonlinear switching behaviours in a compact all-semiconductor optical-amplifier Sagnac interferometer device,” *IEEE Journal of Quantum Electronics*, 35(10):1469 – 77, October 1999.

[87] K. Gallo, G. Assanto, and G.I. Stegeman, “Efficient wavelength shifting over the erbium amplifier bandwidth via cascaded second order processes in lithium niobate waveguides,” *Applied Physics Letters*, 71(8):1020 – 2, August 1997.

[88] R. Schiek, W. Elflein, T. Pertsch, A. Tunnermann, K.R. Parameswaran, and M.M. Fejer, "Femtosecond all-optical switching in a lithium niobate directional coupler with cascaded nonlinearity," in *Nonlinear Optics: Materials, Fundamentals, and Applications*, Technical Digest, TOPS, Vol. 46, August 2000.

[89] G.S. Kanter, P. Kumar, K.R. Parameswaran, and M.M. Fejer, "Wavelength-selective pulsed all-optical switching based on cascaded second-order nonlinearity in a periodically poled lithium-niobate waveguide," *IEEE Photonics Technology Letters*, 13(4):341 – 3, April 2001.

[90] M.C. Cardakli, D. Gurkan, S.A. Havstad, A.E. Willner, K.R. Parameswaran, M.M. Fejer, and I. Brener, "Tunable all-optical time-slot-interchange and wavelength conversion using difference-frequency-generation and optical buffers," *IEEE Photonics Technology Letters*, 14(2):200 – 2, February 2002.

[91] D. Gurkan, M.C. Hauer, A.B. Sahin, Z. Pan, S. Lee, A.E. Willner, K.R. Parameswaran, and M.M. Fejer, "Demonstration of multi-wavelength all-optical header recognition using a PPLN and optical correlators," *European Conference on Optical Communications*, paper We.B.2.5 (invited), October 2001.

[92] M.H. Chou, K.R. Parameswaran, M.M. Fejer, and I. Brener, "Multiple-channel wavelength conversion by use of engineered quasi-phase-matching structures in $LiNbO_3$ waveguides," *Optics Letters*, 24(16):1157 – 9, August 1999.

[93] J. Rams and J.M. Cabrera, "Preparation of proton-exchange $LiNbO_3$ waveguides in benzoic acid vapor," *Journal of the Optical Society of America B (Optical Physics)*, 16(3):401 – 6, March 1999.

[94] Y. Furukawa, K. Kitamura, S. Takekawa, A. Alesandrovski, G. Foulon, R.K. Route, and M.M. Fejer, "Elimination of photorefraction and green-induced-infrared-absorption in MgO-doped near-stoichiometric $LiNbO_3$," *Topical Meeting on Advanced Solid-State Lasers (ASSL)*, February 2000.

[95] T.R. Volk, V.I. Pryalkin, and N.M. Rubinina, "Optical-damage-resistant $LiNbO_3$:Zn crystal," *Optics Letters*, 15(18):996 – 8, September 1990.

[96] E. Schiller, E. Herreros, and G. Lifante, “Optical characterization of vapor Zn-diffused waveguides in lithium niobate,” *Journal of the Optical Society of America A (Optics, Image Science and Vision)*, 14(2):425 – 9, February 1997.

[97] M. Asobe, O. Tadanaga, H. Miyazawa, and H. Suzuki, “Parametric wavelength conversion and amplification using damage-resistant Zn:$LiNbO_3$ waveguide,” *Electronics Letters*, 37(15):962 – 4, July 2001.

[98] A. Grisard, E. Lallier, K. Polgar, and A. Peter, “Low electric field periodic poling of thick stoichiometric lithium niobate,” *Electronics Letters*, 36(12):1043 – 4, June 2000.

[99] L.A. Eyres, P.J. Tourreau, T.J. Pinguet, C.B. Ebert, J.S. Harris, M.M. Fejer, L. Becouarn, B. Gerard, and E. Lallier, “All-epitaxial fabrication of thick orientation-patterned GaAs films for nonlinear optical frequency conversion,” *Applied Physics Letters*, 79(7):904 – 6, August 2001.